

# Brownian Dynamics Simulations of Fine-Scale Molecular Models

by

Irina Burmenko

B.S. Chemical Engineering  
Purdue University (2000)

Submitted to the Department of Chemical Engineering  
in partial fulfillment of the requirements for the degree of

Master of Science in Chemical Engineering

at the

MASSACHUSETTS INSTITUTE OF TECHNOLOGY

June 2005

© Massachusetts Institute of Technology 2005

Signature of Author.....

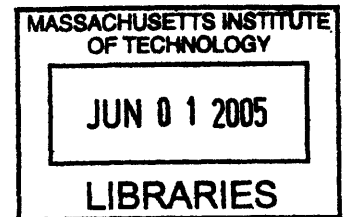
Department of Chemical Engineering  
24 May 2005

Certified by.....

Robert C. Armstrong  
Chevron Professor of Chemical Engineering  
Thesis Supervisor

Accepted by.....

Daniel Blankschtein  
Chairman, Committee for Graduate Students



ARCHIVES

# Brownian Dynamics Simulations of Fine-Scale Molecular Models

by

Irina Burmenko

Submitted to the Department of Chemical Engineering  
on 24 May 2005, in partial fulfillment of the  
requirements for the degree of  
Master of Science in Chemical Engineering

## Abstract

One of the biggest challenges in non-Newtonian fluid mechanics is calculating the polymer contribution to the stress tensor, which is needed to calculate velocity and pressure fields as well as other quantities of interest. In the case of a Newtonian fluid, the stress tensor is linearly proportional to the velocity gradient and is given by the Newton's law of viscosity, but no such unique constitutive equation exists for non-Newtonian fluids. In order to predict accurately a polymer's rheological properties, it is important to have a good understanding of the molecular configurations in various flow situations. To obtain this information about molecular configurations and orientations, a micromechanical representation of a polymer molecule must be proposed. A micromechanical model may be fine scale, such as the Kramers chain model, which accurately predicts a real polymer's rheological properties, but at the same time possesses too many degrees of freedom to be used in complex flow simulations, or it may be a coarse-grained model, such as the Hookean or the FENE dumbbell models, which can be used in complex flow analysis, but have too few degrees of freedom to adequately describe the rheology. The Adaptive Length Scale (ALS) model proposed by Ghosh et al. is only marginally more complicated than the FENE dumbbell model, yet it is able to capture the rapid stress growth in the start-up of uniaxial elongational flow, which is not predicted correctly by the simple dumbbell models.

The ALS model is optimized in order to have its simulation time as close as possible to that of the FENE dumbbell. Subsequently, the ALS model is simulated in the start-up of the uniaxial elongational and shear flows as well as in steady extensional and shear flows, and the results are compared to those obtained with other competing rheological models such as the Kramers chain, FENE chain, and FENE dumbbell. While a 5-spring FENE chain predicts results that are in very good agreement with the Kramers chain, the required simulation time clearly makes it impossible to use this model in complex flow simulations. The ALS model agrees better with the Kramers chain than does the FENE dumbbell in the start-up of shear and elongational flows. However, the ALS model takes too long to achieve steady state, which is something that needs to be explored further before the model is used in complex flow calculations. Understanding of this phenomena may explain why the stress-birefringence hysteresis loop predicted by the ALS model is unexpectedly small. In general, if polymer stress is to be calculated using Brownian dynamics simulations, a large number of stochastic trajectories must be simulated in order to predict accurately the macroscopic quantities of interest, which makes the problem computationally expensive. However, recent technological advances as well as a new simulation algorithm called

Brownian configuration fields make such problems much more tractable. The operation count in order to assess the feasibility of using the ALS model in complex flow situations yields very promising results if parallel computing is used to calculate polymer contribution to stress.

In an attempt to capture polydispersity of real polymer solutions, the use of multi-mode models is explored. The model is fit to the linear viscoelastic spectrum to obtain relaxation times and individual modes' contributions to polymer viscosity. Then, data-fitting to the dimensionless extensional viscosity in the startup of the uniaxial elongational flow is performed for the ALS and the FENE dumbbell models to obtain the molecule's contour length,  $b_{\max}$ . It is found that the results from the single-mode and the four-mode ALS models agree much better with the experimental data than do the corresponding single-mode and four-mode FENE dumbbell models. However, all four models resulted in a poor fit to the steady shear data, which may be explained by the fact that the zero-shear-rate viscosity obtained via a fit to the dynamic data by Rothstein and McKinley and used in present simulations, tends to be somewhat lower than the steady-state shear viscosity at very low shear rates, which may have caused a mismatch between the value of  $\eta_0$  used in the simulation and the true  $\eta_0$  of the polymer solution.

As a motivation for using the ALS model in complex flow calculations, the results by Phillips, who simulated the closed-form version of the model in the benchmark 4:1:4 contraction-expansion problem are presented and compared to the experimental results by Rothstein and McKinley [49]. While the experimental observations show that there exists a large extra pressure drop, which increases monotonically with increasing  $De$  above the value observed for a Newtonian fluid subjected to the same flow conditions, the simulation results with a closed-form version of the FENE dumbbell model, called FENE-CR, exhibit the opposite trend. The ALS-C model, on the other hand, is able to predict the trend correctly. The use of the ALS-C model in another benchmark problem, namely the flow around an array of cylinders confined between two parallel plates, also shows very promising results, which are in much better agreement with experimental data by Liu as compared to the Oldroyd-B model. The simulation results for the ALS-C and the Oldroyd-B models are due to Joo, *et al.* [28] and Smith *et al.* [50], respectively.

Overall, it is concluded that the ALS model is superior to the commonly used FENE dumbbell model, although more work is needed to understand why it takes significantly longer than the FENE dumbbell to achieve steady state in uniaxial elongational flows, and why the stress-birefringence hysteresis loop predicted by the ALS model is much smaller than that of the other rheological models.

Thesis Supervisor: Robert C. Armstrong  
Title: Chevron Professor of Chemical Engineering

# Acknowledgements<sup>1</sup>

There are many people whom I would like to thank for making my stay at MIT enjoyable. First of all, I would like to thank my advisor, Bob Armstrong, for guiding me through my research and for helping me overcome the usual hurdles of graduate research. It meant a great deal to me that he understood and accepted my decision not to continue pursuing my Ph.D. I was also lucky to have Pat Doyle and Gareth McKinley as my committee members. Pat always found time to meet with me if I needed his help or advice, and I really appreciate his providing me with the Kramers chain code, which made writing this thesis that much easier and less stressful. A special thank you goes to Bob Armstrong's assistant, Melanie Miller, who has been helpful beyond words.

I would also like to thank past and present fluid mechanics group members. I will always be grateful to Jason Suen for spending countless hours with me explaining the principles of kinetic theory and guiding me in my research for the next two years. Even though I only met Indranil Ghosh once, his new rheological model served as basis for my research. My thanks also go to Yong Joo, Scott Phillips, Pankaj Doshi, Arvind Gopinath, Micah Green, and Theis Clarke for the many useful conversations that we had. I wish you guys all the best in your current and future endeavors.

My stay at MIT would not be nearly as memorable had it not been for some wonderful friends that I made among my classmates: Saeeda, Greg, Nina, and Noreen. I am really glad that I got to know them, and I truly hope that our friendships will continue after we all leave MIT. It is the friendships outside of MIT that kept me happy and sane even when I had hit dead-ends in my research and nothing seemed to work. My friends Grisha, Inna, Olya, Marina,

---

<sup>1</sup>This work was supported by the ERC program of the National Science Foundation under Award Number EEC-9731680.

Bella, and Jay were always there for me a short drive or a phone call away with a kind word of support, and I can only hope that I can be as a good a friend to them as they have been to me.

None of what I have achieved, including sports and academics, would have been possible without the support of my family. Even since I can remember myself, my parents have been there for me, carefully guiding me and supporting my decisions without exerting pressure to behave a certain way or to choose a certain path. I am very lucky to have them and my brother Eugene, whom I can count on anytime I need help. And finally, my husband Dan... He has been a constant source of love, laughter, and encouragement every step of the way, and I so look forward to spending the rest of my life with him.

# Contents

<b>Contents</b>	<b>6</b>
<b>List of Figures</b>	<b>7</b>
<b>List of Tables</b>	<b>8</b>
<b>1 Introduction</b>	<b>9</b>
1.1 Motivation . . . . .	9
1.2 Viscoelastic flow analysis . . . . .	12
1.3 Commonly used constitutive equations . . . . .	14
1.4 Thesis goals and outline . . . . .	14
<b>2 Introduction to Polymer Kinetic Theory</b>	<b>17</b>
2.1 Micromechanical models . . . . .	18
2.1.1 Bead-rod chains . . . . .	18
2.1.2 Elastic chains . . . . .	20
2.1.3 Dumbbells . . . . .	25
2.2 Incorporating molecular models into stress calculation . . . . .	29
2.2.1 Direct simulation of the Fokker-Planck equation . . . . .	30
2.2.2 Moment equation with closure approximation . . . . .	32
2.2.3 Stochastic approach . . . . .	33
2.2.4 Importance sampling technique . . . . .	38
2.2.5 Control variable technique . . . . .	38

<b>3</b>	<b>The Adaptive Length Scale Model (ALS)</b>	<b>40</b>
3.1	Model description . . . . .	41
3.2	Governing equations . . . . .	42
3.3	Closed form of the ALS model . . . . .	47
<b>4</b>	<b>Optimization of the ALS model</b>	<b>49</b>
4.1	Solving for $b_{\text{seg}}^*$ . . . . .	49
4.1.1	Bisection Method . . . . .	50
4.1.2	Newton's method . . . . .	51
4.1.3	Lookup table . . . . .	53
4.1.4	Polynomial expression . . . . .	54
4.1.5	Approximated Newton's method . . . . .	55
4.2	Time integration methods . . . . .	56
4.3	Summary . . . . .	58
<b>5</b>	<b>Behavior of the ALS model in simple flows</b>	<b>60</b>
5.1	Rheological predictions of the ALS model . . . . .	63
5.2	Parameter dependence . . . . .	70
<b>6</b>	<b>Multi-mode models</b>	<b>76</b>
<b>7</b>	<b>Complex Flow Calculations Using Stochastic Methods</b>	<b>82</b>
7.1	Lagrangian CONNFFESSIT method . . . . .	83
7.2	Eulerian CONNFFESSIT method (Brownian Configuration Fields) . . . . .	85
7.3	Feasibility of using ALS in complex flow simulations . . . . .	87
7.4	ALS-C in complex flows . . . . .	90
<b>8</b>	<b>Conclusion</b>	<b>96</b>
8.1	Summary . . . . .	96
8.2	Suggested future work . . . . .	99
	<b>Bibliography</b>	<b>100</b>

# List of Figures

1-1	Non-Newtonian fluid flow phenomena. (a) Tubeless siphon; (b) Die-swell; (c) Rod climbing. [4] . . . . .	10
2-1	Sample chain trajectories in steady shear flow for $N = 50$ and $We = 0.355, 35.5,$ and $3.55 \times 10^8$ . Reproduced from Doyle et al. [16] . . . . .	21
2-2	Comparison of force-extension relationships for three springs force laws: Hookean (solid), FENE (dashed), inverse Langevin (dash-dotted line). The vertical dashed line at $Q/Q_0 = 1$ corresponds to the maximum possible extension at which nonlinear FENE and inverse Langevin forces diverge. . . . .	23
2-3	Ways to incorporate molecular models into kinetic theory. . . . .	30
2-4	Forward Euler time integration algorithm for an elastic dumbbell. . . . .	36
3-1	Evolution of the adaptive length scale $L$ . . . . .	42
4-1	6th order nonlinear algebraic function given by Equation 3.10 as a function of $b_{seg}^*$ . A value of $b_{max} = 150$ was used to generate this figure. . . . .	51
4-2	Plot of the first derivative of the function given by Equation 3.10. $b_{max} = 150$ . . . . .	53
4-3	Timing comparison of various rheological models. . . . .	56
5-1	Transient polymer shear viscosity $(\eta^+ - \eta_s)/nkT\lambda_d$ for the FENE dumbbell and the ALS models for $b_{max} = 150$ , $Z = 1$ and $We = 0.5, 1, 5, 10.65,$ and $50$ . FENE dumbbell results for $We = 0.5$ and $1$ coincide with the ALS results for corresponding values of $We$ . . . . .	61

5-2	Transient polymer elongational viscosity $(\bar{\eta}^+ - 3\eta_s)/nkT\lambda_d$ for the FENE dumbbell and the ALS models for $b_{\max} = 150$ , $Z = 1$ and $We = 0.5, 1, 5, 10.65$ , and 50. . . . .	62
5-3	The dependence of $M_{\text{seg}}^*$ on $Q^2$ (made dimensionless by one-third of the equilibrium length of a FENE dumbbell) for various $We$ . $b_{\max} = 150$ , $Z = 1$ . . . . .	62
5-4	Dependence of transient polymer elongational viscosity on strain for a 50-rod Kramers chain and the corresponding forms of the ALS, ALS-C, FENE dumbbell, and FENE-P dumbbell models in start-up of uniaxial extensional flow for $We = 10.65$ . The maximum extensibility for the elastic spring models, $b_{\max}$ is 150. Kramers chain data are obtained from Doyle <i>et al.</i> [15]. . . . .	64
5-5	Dependence of polymer contribution to shear viscosity on strain for a 50-rod Kramers chain and the corresponding forms of the ALS, ALS-C, FENE dumbbell, and FENE-P dumbbell models in start-up of steady shear flow for $We = 10.65$ . The maximum extensibility for the elastic spring models, $b_{\max}$ is 150. $b_0 = 150$ . Kramers chain data are obtained from Doyle <i>et al.</i> [15]. . . . .	65
5-6	Dependence of the first normal stress coefficient $\Psi_1^+$ on strain for a 50-rod Kramers chain and the corresponding forms of the ALS, ALS-C, FENE dumbbell, and FENE-P dumbbell models in start-up of steady shear flow for $We = 10.65$ . The maximum extensibility for the elastic spring models, $b_{\max}$ is 150. $b_0 = 150$ . Kramers chain data are obtained from Doyle <i>et al.</i> [15]. . . . .	66
5-7	Dependence of elongational viscosity on $We$ for a 50-rod Kramers chain and the corresponding forms of the ALS, ALS-C, FENE dumbbell, and FENE-P dumbbell models in steady elongational flow. The maximum extensibility for the elastic spring models, $b_{\max}$ is 150. Kramers chain data are obtained from Doyle <i>et al.</i> [16]. . . . .	67
5-8	Dependence of viscosity on $We$ for a 50-rod Kramers chain and the corresponding forms of the ALS, ALS-C, FENE dumbbell, and FENE-P dumbbell models in steady shear flow. The maximum extensibility for the elastic spring models, $b_{\max}$ is 150. $b_0 = 150$ . Kramers chain data are obtained from Doyle <i>et al.</i> [16]. $b_0 = 150$ .	68

5-9	Dependence of first normal stress coefficient on $We$ for a 50-rod Kramers chain and the corresponding forms of the ALS, ALS-C, FENE dumbbell, and FENE-P dumbbell models in steady shear flow. The maximum extensibility for the elastic spring models, $b_{\max}$ is 150. Kramers chain data are obtained from Doyle <i>et al.</i> [16]. $b_0 = 150$ . . . . .	69
5-10	Polymer stress vs. birefringence for start-up of elongational flow up to $\varepsilon = 6$ and subsequent relaxation. The results are shown for the Kramers chain with $N = 50$ , the ALS, ALS-C, FENE dumbbell, and FENE-P dumbbell models with $b_{\max} = 150$ . Kramers chain data are obtained from Doyle <i>et al.</i> [17]. . . . .	71
5-11	Sample chain configurations during start-up of extensional flow at $We = 10.65$ and subsequent relaxation. During start-up the chain follows the right hand side path, and the left hand side path is followed during relaxation. Reproduced from [17]. . . . .	71
5-12	Dependence of polymer contribution to the elongational viscosity on strain in the ALS model for values of $Z = 0.1, 0.2, 0.5, 1, 2, 5, 10$ . $We = 10.65$ and $b_{\max} = 150$ are held constant. . . . .	72
5-13	Dependence of polymer contribution to shear viscosity on strain in the ALS model for values of $Z = 0.1, 0.2, 0.5, 1, 2, 5, 10$ . $We = 10.65$ and $b_{\max} = 150$ are held constant. $b_0 = 150$ . . . . .	73
5-14	Dependence of the maximum number of segments $M_{\text{seg,max}}$ on $Z$ for uniaxial elongational flow at $We = 10.65$ and $b_{\max} = 150$ . . . . .	74
5-15	Dependence of the maximum number of segments $M_{\text{seg,max}}$ on $Z$ for simple shear flow at $We = 10.65$ and $b_{\max} = 150$ . . . . .	74
5-16	Dependence of transient polymer viscous stress growth coefficient $\eta^+$ on strain for a 50-rod Kramers chain and the corresponding forms of the ALS, ALS-C, FENE dumbbell, and FENE-P dumbbell models in start-up of steady shear flow for $We = 10.65$ . The maximum extensibility for the elastic spring models, $b_{\max}$ , is 150. . . . .	75
6-1	Linear viscoelastic fit to the experimental data by Rothstein [49]: (a) single-mode fit, (b) 4-mode fit. . . . .	77

6-2	Single-mode data-fitting to experimental data in order to find the best value of $b_{\max}$ . The included results are: i) experimental data with 0.025 wt% PS solution ([49]), simulation results with a single-mode ALS model with $Z = 0.25, 0.5, 1$ and 2, and simulation results with a single-mode FENE dumbbell model. (a) $b_{\max} = 7744$ , (b) $b_{\max} = 1000$ , (c) $b_{\max} = 500$ , (d) $b_{\max} = 1000$ . Trouton ratio is defined as $\bar{\eta}^+/\eta_0$ , where $\bar{\eta}^+$ is the transient extensional viscosity and $\eta_0$ is the zero-shear-rate viscosity; $\dot{\epsilon} = 9.1$ sec. . . . .	79
6-3	Data fitting to extensional rheology with (a) 4-mode ALS model and (b) 4-mode FENE dumbbell model to determine the best values of $b_{\max}$ for each mode. Trouton ratio is defined as $\bar{\eta}^+/\eta_0$ , where $\bar{\eta}^+$ is the transient extensional viscosity and $\eta_0$ is the zero-shear rate viscosity. The vertical dashed line at Strain of 2.75 indicates the maximum value of strain achieved in the experimental setup; $\dot{\epsilon} = 9.1$ sec. . . . .	80
6-4	Dependence of polymer elongational viscosity on strain for a 50-rod Kramers chain and the corresponding forms of the ALS, FENE dumbbell, 5-mode FENE dumbbell and the 5-spring FENE chain models in start-up of uniaxial extensional flow at $We = 10.65$ . The maximum extensibility for the single-mode ALS and the single-mode FENE dumbbell models, $b_{\max}$ , is 150. The maximum extensibility for each mode of the 5-mode FENE dumbbell model, starting from the slowest one, are: 150, 75, 50, 37.5, and 30. Maximum extensibility of each spring in the chain is 30. Kramers chain data are obtained from Doyle <i>et al.</i> [15]. Insert: Dependence of the ensemble-averaged number of segments in the ALS model on strain. . . . .	81
7-1	Comparison between Lagrangian (CONNFESSIT) and Eulerian (Brownian configuration fields) implementations. (a) Lagrangian implementation, in which ensembles at adjacent nodes are uncorrelated; (b) Eulerian implementation, where the same ensemble of random numbers is generated at each node in the physical domain. . . . .	85

7-2	In the operator splitting method, the macroscopic process environment solver and the microstructure solvers are completely decoupled, which means that changes to one of the solvers have no effect on the other one. . . . .	88
7-3	Schematic of the parallelization process for the contraction-expansion problem. .	90
7-4	Schematic of the contraction-expansion geometry. $R_1$ is the radius of the upstream . . . . .	91
7-5	Extra pressure drop made dimensionless by the pressure drop for the Newtonian fluid as a function of $De$ for the 4:1:4 axisymmetric contraction-expansion problem with a sharp re-entrant corner. Data presented are from experiments ([48]) and from computations with the FENE-CR model with the maximum extensibility $L = 3.2, 4, 5$ ([56]). The horizontal dashed line corresponds to the Newtonian limit. . . . .	92
7-6	Extra pressure drop made dimensionless by the pressure drop for the Newtonian fluid as a function of $De$ for the 4:1:4 axisymmetric contraction-expansion problem with a rounded re-entrant corner. The plot includes: experimental data for the Boger fluid by Rothstein and McKinley ([49]), FENE-P dumbbell results and single-mode ALS-C results with $Z = 0.25, 0.5, 1,$ and $2$ and $b_{\max} = 7, 744$ from simulations by Phillips ([47]). . . . .	93
7-7	Flow past a linear, periodic array of cylinders confined between two parallel plates. The cylinders each have radius $R_c$ , and the geometry is specified by the cylinder-to-cylinder spacing $L$ and the channel half height $H_c$ . The unit cell on which computations are performed is shaded. . . . .	94
7-8	Dependence of the critical Weissenberg number, $We_{cr}$ on the inter-cylinder spacing $L$ for the flow around an array of cylinders confined between two parallel plates. Data presented are: PIB/PB Boger fluid experimental data by Liu ([38]), simulation results with an Oldroyd-B model by Smith <i>et al.</i> ([50]), and simulations results with the ALS-C model by Joo <i>et al.</i> for $b_{\max} = 120$ and $12, 500$ ([28]). . . . .	95

# List of Tables

2.1	Comparison of the Fokker-Planck and the stochastic approaches in solving viscoelastic flow problems. . . . .	37
4.1	Breakdown on timing for the ALS and the FENE dumbbell models . . . . .	56
6.1	Set of parameters for a 4-mode ALS model resulting in the best fit to the transient uniaxial elongation experimental data of Rothstein et al. . . . .	78
7.1	Operation count for the ALS model in complex flow calculations . . . . .	88

# Chapter 1

## Introduction

### 1.1 Motivation

Polymers are a large class of materials consisting of many small molecules called monomers that are linked together to form long chains. A typical polymer may include tens of thousands of monomer units. Because of their large size, polymers are classified as macromolecules. Polymers can be found occurring in nature, and they can also be made synthetically. Arguably, the most important natural polymer is DNA, which is a genetic blueprint that defines all living things. People have taken advantage of the versatility of polymers in the form of oils, resins and tars for hundreds of years, but the modern polymer industry began developing during the Industrial Revolution. However, the progress in polymer science was relatively slow until the 1930's when polymers such as vinyl, neoprene, polystyrene, and nylon were invented. Today, natural and synthetic polymers are used in nearly every industry due to the unmatched diversity of their properties such as strength, heat resistance, stiffness and density.

Because of their long-chain architecture, polymers, which fall into the category of non-Newtonian fluids, tend to exhibit behavior that is different from their Newtonian counterparts. In particular, non-Newtonian fluids exhibit shear rate-dependent viscosity and non-zero normal stresses in simple shear flow and elongation rate-dependent extensional viscosity in simple elongational flow. These fluids may also display time-dependent effects, with the fading memory of the polymer given by a characteristic relaxation time  $\lambda$ . Some striking flow phenomena are

summarized in Figure 1-1: (a) In a tubeless siphon experiment, a fluid gets siphoned out of a container when a tube is lifted. While a Newtonian fluid will stop flowing, a non-Newtonian fluid will continue to flow, (b) In a die-swell experiment, a polymeric fluid exits a capillary with the diameter of the exiting jet increasing to about 300% of the capillary diameter. In contrast, a Newtonian fluid would have a die-swell of no more than 13%, (c) When a non-Newtonian fluid is stirred with a rod, normal stresses create tension along the circular lines of flow, thus causing the fluid to climb up the rod. This is called the "rod climbing" or the Weissenberg effect. Other phenomena such as secondary flow, jet break-up and elastic recoil are depicted and explained in [4] and [9].

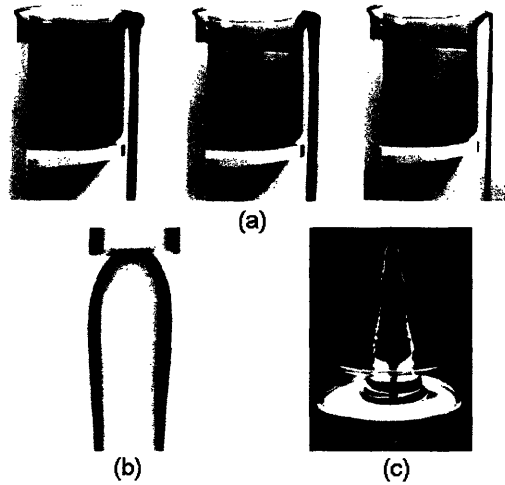


Figure 1-1: Non-Newtonian fluid flow phenomena. (a) Tubeless siphon; (b) Die-swell; (c) Rod climbing. [4]

The non-linear behavior of non-Newtonian fluids lies in the origin of the fundamental problem in polymer fluid mechanics of how to calculate the stress tensor, which in itself is a function of various kinematic tensors. In the case of a Newtonian fluid, the stress tensor is linearly proportional to the velocity gradient and is given by the Newton's law of viscosity, but no such unique constitutive equation exists for non-Newtonian fluids. Over the years, a number of empirical relations have been proposed to calculate polymer contribution to the stress tensor, and they are reviewed by Bird and Wiest [8].

In order to predict accurately a polymer's rheological properties, it is important to have a good understanding of the various conformations that a polymer molecule may assume, and ideally, the forces along its backbone in a variety of flow situations. A homogeneous, or simple, flow falls into a class of flows in which the velocity gradient tensor, which describes the kinematics of the fluid, does not vary spatially. Common types of simple flows are shear, uniaxial elongational, and planar elongational flows. One of the major challenges of the polymer kinetic theory on the experimental front has been to understand the relationship between the configuration of an individual molecule and the force along its backbone. Such understanding could be used to design a micro-mechanical model whose backbone forces were related to conformation at a submolecular level, the same way it is for actual polymer molecules. A variety of experimental techniques have been used to gain this understanding. These techniques include optical methods such as birefringence and light scattering, which provide information about the mean orientation and conformations of the molecules, nuclear magnetic resonance (NMR) and neutron scattering methods, which provide detailed information about the conformational distribution function, and fluorescence video microscopy, which provides direct observations of molecular conformational changes in the flow [54]. An important milestone was the development of a filament stretching rheometer, which allowed for quantitatively reliable measurements of transient stress growth as a function of strain and strain rate in uniaxial elongational flows [57].

Experimental advances in birefringence measurements have also allowed for a better understanding of the average molecular conformations in complex flows. Techniques which can visualize the birefringence at every point in a complex flow were developed by Liu [38], Geneiser [22], and Burghardt *et al.* [11]. Birefringence is related to the second moment of the configurational distribution function and can therefore yield information about the conformation of molecules in the flow domain. By using the stress-optical rule, which predicts a linear relationship between stress and birefringence, the researchers claimed that their birefringence measurements can be used to calculate polymer contribution to the stress in the entire flow domain. However, Doyle *et al.* later showed that the stress-optical rule breaks down for large strains in elongational flows [17]. In addition, the stress-optical relationship was found to vary with the flow history experienced by the polymers. Hence, birefringence measurements can

provide only limited information about the stress field in a complex flow geometry.

Molecular models are used in kinetic theory because they can provide information about the conformations of polymer chains in solution, which is of great importance for accurate prediction of the final product properties. Aside from that, the use of molecular approach is important for a number of other reasons. Polymeric liquids are usually composed of chains with different molecular weights, and this polydispersity can have significant effects on the fluid's rheology. Information provided by molecular models such as molecular architecture and chain stiffness can be used to improve existing models. The use of molecular models can also help account for solvent-solute interactions as well as elucidate the behavior of viscoelastic fluids near boundaries such as sharp corners, contact lines and stagnation points. The ultimate goal is to connect the information provided by molecular modeling with the macroscopic calculations to solve industrially important problems such as fiber spinning, film blowing and injection molding.

## 1.2 Viscoelastic flow analysis

The first step in understanding non-Newtonian fluids lies in being able to characterize them properly. For example, Newtonian fluids at constant temperature can be characterized by just two material constants: the density  $\rho$  and the viscosity  $\mu$ . Once these properties have been measured, the governing equations for the velocity and stress distributions in the fluid are fixed for any flow system [4]. On the other hand, experiments performed on non-Newtonian polymeric fluids yield a number of material properties, which may depend on shear rate, frequency, time, etc. The two standard kinds of flows used to characterize polymeric liquids are shear and shearfree flows, which are discussed in detail in [4] and are briefly summarized here.

The velocity field for a simple shear flow is given by

$$v_x = \dot{\gamma}_{yx}y; \quad v_y = 0; \quad v_z = 0 \quad (1.1)$$

where the velocity gradient  $\dot{\gamma}_{yx}$  can be a function of time. The magnitude or the second invariant of the rate of strain tensor  $\dot{\boldsymbol{\gamma}} = \nabla \mathbf{v} + \nabla \mathbf{v}^T$  is called the shear rate  $\dot{\gamma}$ , and it is independent of time for steady shear flows. Simple shear flow is completely characterized by three material functions, which for steady state are the viscosity  $\eta$ , and the first and second normal stress

coefficients  $\Psi_1$  and  $\Psi_2$ . These material functions have the following definitions

$$\tau_{yx} = -\eta(\dot{\gamma})\dot{\gamma}_{yx} \quad (1.2)$$

$$\tau_{xx} - \tau_{yy} = -\Psi_1(\dot{\gamma})\dot{\gamma}_{yx}^2 \quad (1.3)$$

$$\tau_{yy} - \tau_{zz} = -\Psi_2(\dot{\gamma})\dot{\gamma}_{yx}^2 \quad (1.4)$$

Simple shearfree flows are given by the velocity field

$$v_x = -\frac{1}{2}\dot{\epsilon}(1+b)x \quad (1.5)$$

$$v_y = -\frac{1}{2}\dot{\epsilon}(1-b)y \quad (1.6)$$

$$v_z = +\dot{\epsilon}z \quad (1.7)$$

where  $0 \leq b \leq 1$  and  $\dot{\epsilon}$  is the elongation rate, which can be time-dependent. The choice of the parameter  $b$  determines the type of a shearfree flow

Uniaxial elongational flow: ( $b = 0, \dot{\epsilon} > 0$ )

Biaxial stretching flow: ( $b = 0, \dot{\epsilon} < 0$ )

Planar elongational flow: ( $b = 1$ )

For steady simple shearfree flows, there exist two material functions,  $\bar{\eta}_1$  and  $\bar{\eta}_2$ , which define two normal stress differences

$$\tau_{zz} - \tau_{xx} = -\bar{\eta}_1(\dot{\epsilon}, b)\dot{\epsilon} \quad (1.8)$$

$$\tau_{yy} - \tau_{xx} = -\bar{\eta}_2(\dot{\epsilon}, b)\dot{\epsilon} \quad (1.9)$$

If the flow is uniaxial elongational,  $\bar{\eta}_2 = 0$  and  $\bar{\eta}_1$  is defined to be the elongational viscosity  $\bar{\eta}(\dot{\epsilon})$ .

The three most important dimensionless parameters that govern the flow of non-Newtonian fluids are the Reynolds number (Re), the Deborah number (De), and the Weissenberg number (We). The Reynolds number is defined as the ratio of inertial forces to viscous forces, and due to high viscosities of polymeric liquids, this parameter is typically negligible and hence  $\text{Re} \approx 0$  is assumed in most calculations.

The Deborah number is defined to be the ratio of the polymer characteristic relaxation time  $\lambda$  to the observation time,  $T$ , i.e.  $De = \lambda/T$ . The observation time is typically the residence time of a polymer molecule in the flow process. If  $De \ll 1$ , polymer molecules relax very quickly and the fluid is essentially Newtonian. In the case of  $De \gg 1$ , molecules are not able to change their configuration at all on the time scale of the flow, and the fluid behaves like a Hookean elastic solid. The most interesting phenomena, such as those depicted in Figure 1-1 can be observed when  $De \approx 1$ , in which case the fluid is called viscoelastic.

The Weissenberg number is defined as the product of the characteristic polymer relaxation time and the characteristic strain rate  $\kappa$ , i.e.  $We = \lambda\kappa$ . In many flow geometries, the characteristic time of the flow is the inverse of the characteristic strain rate, in which case  $De$  and  $We$  can be used interchangeably.

### 1.3 Commonly used constitutive equations

Until very recently, the traditional approaches used by chemists, engineers and polymer physicists for deriving constitutive equations for stress calculation have been based on either simple mechanical models (e.g. convected Maxwell model), or on using engineering correlations (e.g. Carreau viscosity model for shear-thinning fluids) or mathematical expansions around Newtonian solutions (e.g. retarded motion expansion). Because each one of these approaches applies to a narrow class of flows, improper use of continuum-based models can lead to erroneous results. Chapter 2 will explain the merits of molecular-based models and information they provide.

### 1.4 Thesis goals and outline

The main goal of this thesis is to develop robust, accurate methods to capture fine-scale polymer dynamics in simple flow calculations. The particular research directions for achieving this goal were:

1. Optimization of the Adaptive Length Scale model (ALS), which was originally introduced by Ghosh *et al.* [25], in order to have the simulation time as close as possible to that of a FENE dumbbell. Such optimization is necessary because complex flow simulations employing the use

of Brownian dynamics are expensive with the majority of CPU time spent on generating random numbers and calculating stress (see Chapter 7).

2. Assessment and comparison of the ALS model with other competing rheological models in simple flows to find a balance between the wish to have as detailed a model as possible and the ability to simulate it in a reasonable amount of time.

3. Evaluation of the use of multi-mode models to capture the range of time scales caused by polydispersity in a real polymer solution.

4. Assessment of closure approximations on the physics predicted by a given model.

And the final goal was to evaluate the feasibility of using the Adaptive Length Scale model in complex flow calculations by doing an operation count. As discussed in Chapter 7, the closed-form of the ALS model, called ALS-C, yields certain predictions in the contraction-expansion geometry as well as in the flow around an array of cylinders confined between two parallel plates, which are missed by the FENE dumbbell model. Therefore, it is of great interest to determine how the unapproximated version of the model will behave in the same flow situation.

The thesis is organized in the following way. Chapter 2 introduces and reviews the kinetic theory of polymers. The chapter begins with the introduction of various micromechanical models used to represent polymer molecules. Then, three different approaches for incorporating molecular models into stress calculations are discussed, followed by a brief summary of the techniques to reduce noise in a Brownian dynamics simulation. Chapter 3 introduces the Adaptive Length Scale (ALS) model, which was designed to capture the fine-scale dynamics of a Kramers chain while retaining only one more degree of freedom in addition to what a simple FENE dumbbell possesses. This chapter discusses the qualitative and quantitative aspects of the model, and it also summarizes the governing equations for a closed-form version of the model, ALS-C proposed in [25]. The focus of Chapter 4 is to describe the approaches that were taken to optimize the ALS model so that its simulation time would be as close as possible to that of a FENE dumbbell. One of the governing equations in the ALS model is a 6th degree nonlinear algebraic equation for the instantaneous maximum extensibility of a segment,  $b_{\text{seg}}^*$ . The solution of this equation is extremely time-consuming, and therefore different approaches such as the bisection method, the Newton's method, lookup table, etc. were evaluated and compared to determine which method gives the fastest solution without a sacrifice in accuracy.

The chapter concludes with a discussion of the relative merits of explicit and semi-implicit time-integration techniques. Chapter 5 is devoted to presenting the rheological predictions of the ALS model in transient as well as steady simple shear and uniaxial elongational flows. This chapter is concluded by examining the model's parameter dependence. Since most real polymeric solutions contain chains of different molecular weights and hence different contour lengths and relaxation times, the use of multi-mode models is explored in Chapter 6. Chapter 7 focuses on the use of stochastic methods in complex flow calculations. First, the CONNFESSIT (**C**alculation of **N**on-**N**ewtonian **F**low: **F**inite **E**lement and **S**tochastic **S**imulation **T**echnique) approaches based on the Lagrangian and the Eulerian point of reference are presented. In the former, the location of each stochastic trajectory representing a polymer molecule is tracked by an ordinary differential equation. In this approach, which was introduced by Laso & Öttinger [31], the stochastic trajectories at adjacent nodes are not correlated, which means that  $N_{node} * N_{traj}$  random numbers have to be generated, where  $N_{node}$  is the number of nodes in the spacial discretization and  $N_{traj}$  is the number of stochastic trajectories being simulated. The Eulerian approach, which is also called the Brownian Configuration fields technique, was introduced by Hulsen *et al.* [26] and van den Brule *et al.* [58]. By replacing individual stochastic particles by continuous configuration fields, they achieved a two-fold benefit. First, because fields at adjacent nodes are correlated, only  $N_{traj}$  random numbers need to be generated, where  $N_{traj}$  is now the number of convected configuration fields, which results in an enormous computational time saving. And two, this correlation results in a natural variance reduction, thus decreasing the noise of the simulation. The rest of the chapter is devoted to performing an operation count on the ALS model to show that the model is feasible for use in complex flow calculations on parallel processors. The chapter is concluded by showing complex flow results of the ALS-C model, which explain its advantage over the commonly used FENE-P dumbbell model. The main findings of this thesis and suggestions for future work are summarized in Chapter 8.

## Chapter 2

# Introduction to Polymer Kinetic Theory

It is often of interest in materials processing to know not only the velocity and stress fields, but also the molecular configurations and orientations. To obtain the latter, one usually begins by proposing a model of the molecular structure. Given the fact that computing the electronic structure of each atom within a polymer molecule using *ab initio* molecular dynamics is impractical for calculating transport and thermodynamic properties, most micromechanical models are constructed using classical mechanics. These micromechanical models can in general be divided into two types: (1) particle-based discrete models, which are used for modeling dilute solutions and will be discussed in this thesis, and (2) field-theoretical continuous models, which are generally used to model concentrated polymer solutions and melts. Then one solves self-consistently the governing microscopic and macroscopic equations. Ideally, the proposed molecular model would be as detailed as possible in order to capture maximum number of important aspects of a real polymer molecule. The problem, however, lies in the fact that a typical polymer chain has a broad spectrum of time scales. The shortest ones are related to molecular vibrations and are roughly of the order of  $10^{-12}$  seconds, whereas the slow modes can be of the order of 10 seconds or longer. This kind of spectrum would clearly be impossible to model, and for that reason, a common practice in the polymer kinetic theory has been to focus only on the slow processes that govern the global configurations of the macromolecules by studying

the response of coarse-grained models. Bead-spring and bead-rod chains are commonly used as such models. A detailed account of various coarse-grained models can be found in [5] and [7]. The coarse-grained models are generally nonlinear and possess a large number of degrees of freedom, which complicates their simulation even in simple flows.

## 2.1 Micromechanical models

The most commonly used molecular models, beginning with a relatively fine-grained one known as the Kramers chain, will be discussed in this section, followed by a discussion in the next chapter of the recently proposed single-mode Adaptive Length Scale model (ALS), which takes into account kinematic history of the flow and is able to capture the fine-scale physics of the Kramers chain without having the high computational cost associated with simulating the latter.

### 2.1.1 Bead-rod chains

A Kramers chain, or a freely-jointed bead-rod chain, consists of  $N$  beads joined together by  $N-1$  massless rods. The beads do not represent individual atoms of a polymer chain, but rather a collection of atoms along the molecule's backbone. Each rod has a constant length  $a$ , which corresponds to a Kuhn step ([21]). The name 'freely-jointed' comes from the fact that the rods are allowed to move freely about beads and do not experience bending potentials. Beads and rods can also move 'through' one another, because excluded volume is not accounted for in this model. Solvent molecules are modeled as a continuum, which is described by an incompressible Newtonian liquid with viscosity  $\eta_s$ . In the absence of body forces, each bead  $\nu$  is subjected to three forces, namely (1) the hydrodynamic drag force  $F_\nu^{(h)}$  imparted by the solvent, (2) the Brownian motion force  $F_\nu^{(B)}$ , which results from the bombardment of the beads by the solvent molecules constantly undergoing random thermal motion, and finally (3) the constraint force  $F_\nu^{(c)}$ , which arises from tensions in the rods. Definitions of each of the three forces as well as the force balance can be found elsewhere ([45],[24]). From simulations of Kramers chains in relaxation following the cessation of uniaxial elongational flow, Doyle *et al.* ([16]) found that the longest time scale,  $\lambda_d$ , of the polymer is related to the diffusive time for a single link

( $\lambda_{rod} = \zeta a^2/kT$ ) by

$$\lambda_d = 0.0142N^2 \frac{\zeta a^2}{kT} \quad (2.1)$$

where  $\zeta$  is the bead drag coefficient of the Kramers chain,  $k$  is the Boltzmann constant, and  $T$  is the temperature. In dimensionless form Equation 2.1 has the following form

$$\text{We} = 0.0142N^2\text{Pe} \quad (2.2)$$

The dimensionless group Pe, which naturally arises in Equation 2.2 is the Peclet number, which is the dimensionless diffusion time defined as

$$\text{Pe} = \frac{\zeta a^2}{kT} \dot{\epsilon} \quad (2.3)$$

Here,  $\dot{\epsilon}$  is the extension rate, and the Weissenberg number in Equation 2.2 has the following definition,  $\text{We} = \lambda_d \dot{\epsilon}$ . The expression for the birefringence ([16]) is

$$\Delta n = 5CnkT \sum_{\nu=1}^{N-1} \langle u_{\nu z} u_{\nu z} - u_{\nu x} u_{\nu x} \rangle \quad (2.4)$$

where

$$C = \frac{2\pi}{45kT} \frac{(n^2 + 2)^2}{n} (\alpha_1 - \alpha_2) \quad (2.5)$$

and  $n$  is the isotropic part of the refractive index tensor,  $(\alpha_1, \alpha_2)$  are the (parallel, perpendicular) components of the polarizability tensor, and  $(u_{\nu x}, u_{\nu z})$  are the  $(x, z)$  components of the unit vector pointing from the  $\nu$ th to the  $(\nu + 1)$ th bead.

Liu [39] established the first numerical method for performing Brownian dynamics simulations of dilute solutions of Kramers chains. The condition of constant length of each link in the chain was imposed in his algorithm through the use of Lagrange multipliers. By studying polymer molecules at sudden inception of elongational flows, he was able to obtain visualizations of the chain-unfolding mechanism during the coil-stretch transition. In general, a Kramers chain would have to have on the order of 1000 or more beads in order to mimic a real polymer molecule. But since this kind of simulation is not feasible with current computational resources, researches have modeled chains of 50-200 beads in order to compare their results to the exper-

imental observations. Simulations of a Kramers chain in the start-up of shear and extensional flows as well as comparison of the results to experimental data can be found in [15]. Doyle et al. ([16], [15]) showed that a Kramers chain is capable of exhibiting internal configurations such as kinks and dumbbells similar to those of a real polymer molecule undergoing shear and elongational flow (see Figure 2-1). The study of the rheological and optical behavior of Kramers chains by using stochastic methods in steady shear and uniaxial extension is described in [16]. The authors also developed an algorithm to split the stress into its Brownian and viscous contributions. Based on the algorithm proposed by Liu [39], Ghosh et al. [24] analyzed Kramers chains in uniaxial elongational flows in order to understand the fine-scale physics that the chains are capable of capturing and to assess the validity of coarse-grained models. Both, Doyle *et al.* [17] and Ghosh *et al.* [24], showed that besides exhibiting the distributional stress-birefringence hysteresis, a Kramers chain also exhibits residual hysteresis, which Doyle *et al.* termed the configuration hysteresis. It arises because molecules tend to assume different configurations during extension and relaxation. Most synthetic polymers such as polystyrene, polyethylene, and polypropylene are flexible molecules, which can be represented well by the Kramers chain. A Kramers chain is a relatively detailed model which can accurately represent the important dynamics of a real molecule, but its many degrees of freedom do not allow it to be used in complex flow calculations. Hence, further coarse-graining is required.

### 2.1.2 Elastic chains

To make problems computationally tractable, dilute solutions of polymer molecules are often modeled as beads connected by springs. These bead-spring chains are coarsened versions of the Kramers chains, many segments of which are represented by a single spring, whose “effective” force is entropic in origin. While this is the representation used by most researches, Laso *et al.* [32] showed that such coarse-graining will result in non-uniform bond and torsional angle distribution, thus preventing the bead-spring model from being truly freely-jointed. Thus, even though both the bead-rod and the bead-spring chain models provide detailed information about polymer microstructure, there does not exist a unique mapping relationship between the two.

The bead-spring chains are suspended in a Newtonian solvent and are convected and distorted by the viscous forces exerted on the beads. The beads also experience a randomly

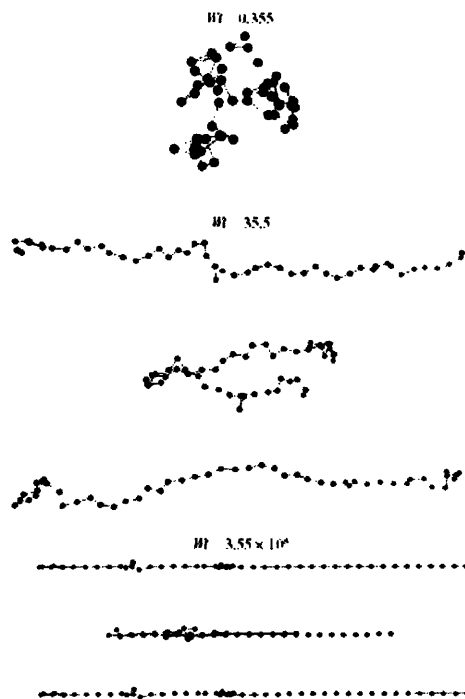


Figure 2-1: Sample chain trajectories in steady shear flow for  $N = 50$  and  $We = 0.355, 35.5,$  and  $3.55 \times 10^8$ . Reproduced from Doyle et al. [16]

fluctuating force due to the thermal agitation by the surrounding solvent molecules, the so-called Brownian force. The hydrodynamic and Brownian forces have the same form as for the Kramers chain. However, unlike the Kramers chain, no constraints exist in an elastic chain, which reduces the simulation time tremendously.

A widely used model for dilute polymer solutions is the Rouse chain, which is made up of beads joined together by Hookean springs. The Hookean force law is given by

$$\mathbf{F}^{(c)}(Q) = H\mathbf{Q} \quad (2.6)$$

In this equation,  $\mathbf{F}^{(c)}$  is the connector force,  $H$  is the spring modulus, and  $\mathbf{Q}$  is the end-to-end vector representing a particular spring in a chain. The constitutive equation associated with this Hookean chain is, in fact, identical to the macroscopic multi-mode Oldroyd-B model. The Rouse chain model is well understood and, because of its linearity, is often amenable to analytical solutions. Major shortcomings of the Rouse chain are that none of the steady shear flow material functions obtained using this model depend on the shear rate and that the springs in the chain can be stretched indefinitely. This can lead to an unbounded value of the elongational viscosity at high strain rates. All of these results are in disagreement with experimental data.

It is suggested in [5] through the use of kinetic theory that the force law for polymer chain models should be nonlinear in the extension of the spring,  $Q$ . The most commonly used nonlinear force law, Finitely Extensible Nonlinear Elastic (FENE) spring force law has the following form:

$$\mathbf{F}^{(c)}(Q) = \frac{H\mathbf{Q}}{1 - \frac{Q^2}{Q_0^2}} \quad (2.7)$$

The FENE force law is an approximation to a more complicated inverse Langevin force law proposed by Warner [62] and is derived based on the equilibrium force-extension relationship for a Kramers chain. The Langevin force law is in given by

$$\mathbf{F}^{(c)}(Q) = \frac{HQ_0}{3} \mathcal{L}^{-1} \left( \frac{\mathbf{Q}}{Q_0} \right) \quad (2.8)$$

In Equations 2.7 and 2.8,  $Q_0$  is the defined as the maximum extensibility of a spring. In

addition,  $\mathcal{L}^{-1}$  in Equation 2.8 is the inverse Langevin function given by  $\mathcal{L}(x) = \coth(x) - x^{-1}$ . A comparison between the inverse Langevin, FENE and Hookean force laws is given in Figure 2-2.

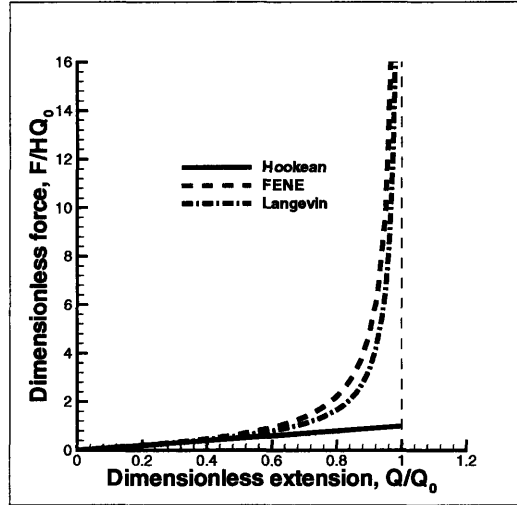


Figure 2-2: Comparison of force-extension relationships for three springs force laws: Hookean (solid), FENE (dashed), inverse Langevin (dash-dotted line). The vertical dashed line at  $Q/Q_0 = 1$  corresponds to the maximum possible extension at which nonlinear FENE and inverse Langevin forces diverge.

As can be seen in Figure 2-2, the three force laws yield identical results for small extensions ( $Q/Q_0 < 0.5$ ). For larger extensions, the Hookean force law, which is a linear approximation to the inverse Langevin force law, underpredicts the spring force. The FENE force law, on the other hand, is a good approximation to the inverse Langevin force law for the whole range of  $Q/Q_0$ . An important feature of these two force laws is that the forces they predict diverge for dimensionless extensions close to unity, which is designed to mimic a real polymer molecule with a finite extensibility. One of the major problems with Hookean springs is that they can be stretched indefinitely, which is clearly unphysical. A major drawback of a FENE chain is that it does not allow for a closed-form constitutive equation for the polymer stress, and therefore it is not suited for traditional continuum approaches to numerical solution of complex flows. As discussed later on in the thesis, this problem can be avoided by coupling direct simulation of a molecular model with solution of the conservation equations from fluid mechanics.

To circumvent the closure problem in the macroscopic finite element calculations, a modification of the FENE model with a Peterlin approximation, which constraints the average extension of the  $j$  segments to a maximum value of  $Q_0$ , was introduced. The force law for a link in a chain of FENE-P springs has the following form

$$\mathbf{F}_j^{(c)}(Q) = \frac{H \mathbf{Q}_j}{1 - \langle Q_j^2 \rangle / Q_0^2}, \quad j = 1..N - 1 \quad (2.9)$$

Because with this model the system of equations governing the evolution of the second moments cannot be transformed to normal coordinates, the calculation involves solving an  $N-1$  by  $N-1$  matrix of 3-dimensional tensorial differential equations, where  $N$  is the number of beads in the chain. Rigorous solutions for a FENE-P chain in shear flow are provided in [44], [64], and [66]. The number of equations to be solved in this model increases roughly as  $N^2$ , and the problem can become computationally expensive even for a relatively small number of beads. Bird *et al.* [6] attempted to decouple their constitutive equation, but made an error in transformation to normal coordinates. Therefore, the constitutive equation they obtained is not that for a true FENE-P chain, but rather for an empirical multimode model that contains time constants which depend on a transformation matrix.

A modification of the FENE-P model called FENE-PM is proposed in [63]. The authors replaced the denominator of the FENE-P spring force with an expression that is invariant under the transformation to normal coordinates. The FENE-PM expression has the form

$$\mathbf{F}_j^{(c)}(Q) = \frac{H \mathbf{Q}_j}{1 - \frac{1}{N-1} \sum_{j=1}^{N-1} \langle (Q_j/Q_0)^2 \rangle} \quad (2.10)$$

This form of the force law constrains the arithmetic average of the square of the average end-to-end distances of the links to the square of the maximum extension  $Q_0$ . One downside of the FENE-PM model is that it is possible for one link in the chain to have  $\langle Q_j^2 \rangle \approx (N - 1) Q_0^2$ , with all other  $\langle Q_j^2 \rangle \approx 0$ . However, as shown in [63], this situation does not occur in shear and elongational flows. After introduction of normal coordinates, the number of FENE-PM second moment equations that need to be solved is proportional to  $N - 1$ , which is a significant reduction from the number of equations in the FENE-P model. FENE and FENE-P models

in start-up of shear and uniaxial elongational flow are compared in [60]. Because closing a model can sometimes significantly alter results of the calculations, the authors offered ways to select parameters of the FENE-P model such that the important FENE flow characteristics are not lost. The effects of excluded volume, polymer chain length, maximum bond extension, and hydrodynamic interactions of the FENE model in steady and transient elongational flows, obtained by using Brownian dynamics simulations, and comparison of the results to the analytic FENE-PM theory of Wedgwood *et al.* [63] are presented in [20]. The problem with closure approximations as applied to FENE dumbbells was also addressed in [29] and [58].

The birefringence of bead-spring models can be calculated using the expression from [65] as

$$\Delta n = 5CnkT \frac{n_s}{Q_{s0}^2} \sum_{i=1}^M \langle \hat{Q}_{iz} \hat{Q}_{iz} - \hat{Q}_{ix} \hat{Q}_{ix} \rangle \quad (2.11)$$

where  $C$  is given by Equation 2.5,  $M$  is the number of springs,  $Q_{s0}$  is the maximum extension of a spring and each spring corresponds to  $n_s$  rods in the Kramers chain representation of a polymer molecule.

### 2.1.3 Dumbbells

As in the case of the Kramers chain, FENE chains have too many degrees of freedom to be used in complex flow calculations. The most commonly used molecular models in fluid mechanics calculations are the elastic dumbbell models, in which polymer molecules are represented by two beads joined together by a linear or a nonlinear spring. The elastic dumbbell model is usually used to represent the end-to-end vector of a Kramers chain. The inverse Langevin force law (and the FENE approximation to it) is obtained from equilibrium statistical mechanics and is based on the assumption that for a given end-to-end distance a Kramers chain has had sufficient time to sample its entire configuration space and that the internal conformational distribution has reached equilibrium. This force law should be used with caution in non-equilibrium situations when molecules are undergoing rapid stretching. The chain will unravel *reversibly* only when the time scale of the deformation is much longer than the relaxation time scale of the entire chain, i.e. the internal conformation of the chain will be able to equilibrate at each stage of the stretching ([23]). Similar to the Kramers chains, FENE dumbbells exhibit

distributional hysteresis, but they lack a sufficient number of internal degrees of freedom to have configurational hysteresis. The time constant,  $\lambda_d$ , for a FENE dumbbell is

$$\lambda_d = \zeta_d/4H_d \quad (2.12)$$

where the dumbbell spring modulus  $H_d$  is related to the Kramers chain parameters through the following equation

$$H_d = \frac{3kT}{(N-1)a^2} \quad (2.13)$$

Combining Equations 2.1, 2.12, and 2.13, we can obtain a relationship between the bead drag coefficient of the Kramers chain and that of the FENE dumbbell,  $\zeta_d$ ,

$$\zeta_d = 0.1704 \frac{N^2}{N-1} \zeta \quad (2.14)$$

There is no unique way to match the time constant for a dumbbell to the time constant of an individual spring in a bead-spring chain. The scaling relationship chosen by Ghosh [23] is such that the transient extensional viscosity of the FENE chains approaches the profile predicted by the Kramers chain as the number of springs in the chain  $M$  becomes large. This condition can be satisfied by a scaling relationship that makes the zero-shear-rate first normal stress coefficient independent of  $M$ . Using the result for the zero-shear-rate first normal stress coefficient presented by Van den Brule *et al.* [58] gives the relationship between the time constants as

$$\lambda_s = \frac{\zeta_s}{4H_s} = \frac{\lambda_d}{K} \quad (2.15)$$

where  $K$  is given by

$$K = \left( \frac{b_s}{b_s + 5} \right) \left( \frac{\sqrt{(b_{\max} + 5)(b_{\max} + 7)}}{b_{\max}} \left\{ \frac{[2(M+1)^2 + 7][ (M+1)^2 - 1]}{45} - \frac{12[(M+1)^4 - 1]}{45(M+1)(b_s + 7)} \right\}^{1/2} \right) \quad (2.16)$$

In Equation 2.16,  $b_{\max}$  is the maximum dimensionless extensibility of a spring in the case a

polymer molecule is represented by a single dumbbell, which is defined as

$$b_{\max} = \frac{H_d Q_0^2}{kT} \quad (2.17)$$

$b_s$  is the maximum extensibility of spring in a bead-spring chain defined by

$$b_s = \frac{H_d Q_0^2}{MkT} \quad (2.18)$$

The quantity  $b_{\max}$  is related to the number of rods in the Kramers chain through the following expression

$$b_{\max} = 3(N - 1) \quad (2.19)$$

While there is no unique way of matching the parameters in the Kramers chain, the FENE chain, and the FENE dumbbell models for proper comparison of their results, if one is interested in studying systems far away from equilibrium, the following matching technique can be used:

- (1) Set the time scale  $\lambda_d$  of the dumbbell to the slowest relaxation time of the Kramers chain and
- (2) Use the scaling relationship given by Equation 2.15 to match the time scale of the dumbbell to that of an individual spring in the chain.

Doyle *et al.* [16] showed that the Kramers chain and the FENE dumbbell cannot predict the same values for the following pairs of properties if the FENE dumbbell has a constant drag coefficient: (1) the zero-shear-rate viscosity and zero-shear-rate first normal stress coefficient and (2) the steady-state elongational viscosity at zero and infinite elongation rate. In order to match the zero-shear-rate viscosities of the two models, they chose the bead drag coefficient for the FENE dumbbell to be  $(2/3)N\zeta$ . With this choice, the FENE dumbbell predicts the zero-shear-rate first normal stress coefficient to be twice that of the Kramers chain.

Whereas the FENE model and its closed versions have been the most popular nonlinear elastic dumbbell models, a new kind of model, termed a HYBRID model was proposed in [12]. The HYBRID model consists of springs that are Hookean at low elongations until the spring length  $Q$  reaches some critical value  $Q_c$ , after which they follow a Morse potential with a given dissociation energy. This new model was shown to be suitable for studying polymer fracture in

strong flows. In trying to develop a closed model that would be capable of reproducing the stress vs. mean square extension hysteresis displayed by the FENE model, Lielens *et al.* [36] proposed a more sophisticated second order closure model for one-dimensional flows, which they referred to as FENE-L. This model approximates the distribution function as a composite of a delta function and a rectangular element. The addition of the rectangular segment adds dispersity to the distribution function. In a follow up paper, Lielens *et al.* [37] extended the model to general, three-dimensional flow kinematics. The authors reported simulations for steady and transient rheometrical flows, which demonstrated the superiority of the FENE-L constitutive equation with respect to the classical FENE-P closure in describing the response of the FENE dumbbell model, both in shear and elongational flows. In particular, the FENE-L model was able to predict the stress-birefringence hysteresis, which is out of reach for a single-mode FENE-P dumbbell.

Dumbbells are by and far the least expensive models to use in finite element calculations, but because they only have three degrees of freedom, the three components of the end-to-end vector  $\mathbf{Q}$ , they perform poorly in predicting experimentally observed behavior of polymer solutions in the start-up of extensional flow [15], [24]. In particular, it is demonstrated in [24] through simulations of the Kramers chain, that for a given value of the end-to-end distance, the effective force in a polymer molecule varies with strain and strain rate. In contrast to this observation, the FENE force law, which describes the entropic elasticity in a slowly stretching polymer chain, is not dependent on either quantity. It is also shown in [25] that whereas a short FENE chain is needed to describe stress growth at low strains, a FENE dumbbell would suffice at higher strains when the molecules are almost fully unraveled. Therefore, the use of a FENE chain with its many degrees of freedom would not be the most efficient way to model a polymer molecule under varied flow conditions. To avoid the problem of having to map between FENE chains with different numbers of springs, Ghosh *et al.* proposed a new single-mode constitutive equation, which they termed the Adaptive Length Scale (ALS) model. The ALS model is described in the next chapter.

## 2.2 Incorporating molecular models into stress calculation

One of the goals of a microscale simulation is to get an expression for the tensor  $\langle \mathbf{Q}\mathbf{Q} \rangle$ , which is the ensemble average of the dyadic product of the end-to-end vector of an elastic dumbbell with itself. Once this expression is known for a linear dumbbell, the polymer contribution to the stress tensor  $\tau_p$  can be calculated with an appropriate constitutive equation. However, as it will be demonstrated in the ensuing discussion, knowing  $\langle \mathbf{Q}\mathbf{Q} \rangle$  is not sufficient for a nonlinear molecular model if a traditional finite element approach is used, and some kind of closure approximation will be required.

Before a molecular model can be used in the viscoelastic flow calculation, constitutive expressions for various flux expressions in the equations of change must be derived. These expressions, such as the one for the stress tensor in the momentum equation, can be obtained from physical arguments or it can be based on a detailed kinetic theory derivation. The goal of this thesis is to concentrate on the latter approach.

The three main approaches for incorporating molecular models into kinetic theory are reviewed in [8] and [54]. They are: (1) the direct simulation of the Fokker-Planck equation, (2) solution of a closed model from a general equation of change, and (3) stochastic simulation of the associated stochastic differential equation. These three approaches are summarized pictorially in Figure 2-3 and discussed in the next three subsections.

In Figure 2-3,  $\mathbf{B}$  is a dynamical variable, which is a function of the end-to-end vector  $\mathbf{Q}$  connecting two beads and  $\psi(\mathbf{Q}, t)$  is the configuration space distribution function. The angular brackets indicate an average quantity. In a direct simulation approach,  $\langle \mathbf{B} \rangle$  is calculated by multiplying  $\mathbf{B}$  by the distribution function  $\psi$ , which is obtained by solving the Fokker-Planck equation, and integrating over all  $\mathbf{Q}^N$ , where  $\mathbf{Q}^N$  is the set of all end-to-end vectors  $\mathbf{Q}$  that describe relative locations of all beads in a bead-spring-rod model. In a stochastic approach,  $\langle \mathbf{B} \rangle$  is defined as the average over all stochastic ensembles. For a converged solution, the two averages are mathematically equivalent.

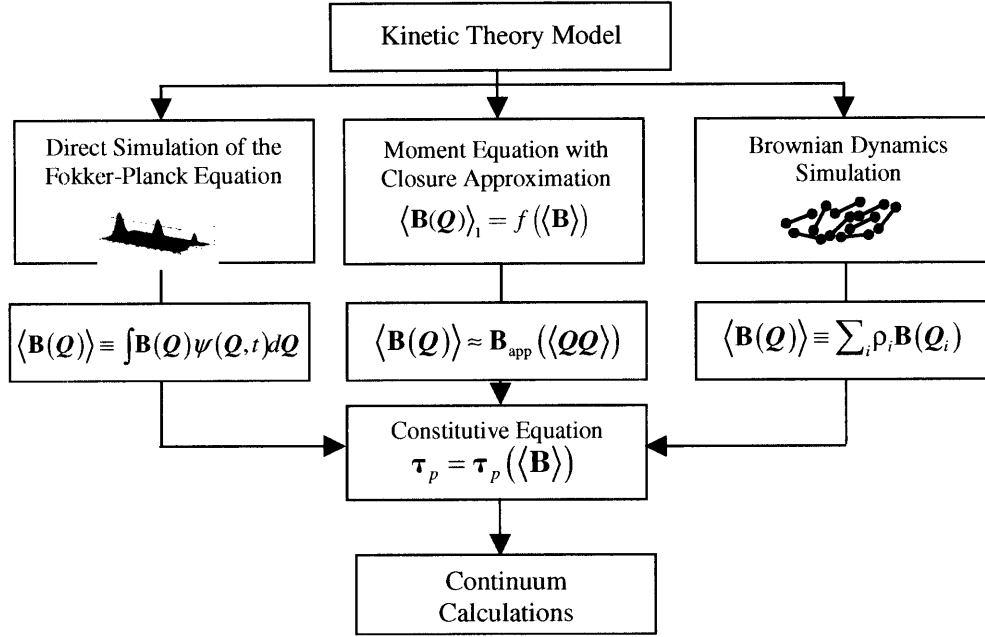


Figure 2-3: Ways to incorporate molecular models into kinetic theory.

### 2.2.1 Direct simulation of the Fokker-Planck equation

The Fokker-Planck equation for an isothermal, homogeneous suspension of elastic dumbbells has the following form:

$$\frac{\partial \psi}{\partial t} + \mathbf{v}_c \cdot \frac{\partial \psi}{\partial \mathbf{r}_c} = - \frac{\partial}{\partial \mathbf{Q}} \cdot \left\{ \nabla \mathbf{v}^T \cdot \mathbf{Q} \psi - \frac{1}{2\zeta} \left( kT \frac{\partial \psi}{\partial \mathbf{Q}} + \mathbf{F}^{(c)} \psi \right) \right\} \quad (2.20)$$

where the normalized configuration space distribution function  $\psi(\mathbf{Q})$  is defined in such a way that  $\psi(\mathbf{Q}, t) d\mathbf{Q}$  is the probability that at time  $t$  a molecule has configuration within  $d\mathbf{Q}$  of  $\mathbf{Q}$  with normalization  $\int \psi(\mathbf{Q}, t) d\mathbf{Q} = 1$ . In Equation 2.20,  $\mathbf{r}_c$  is the location of the molecule's center of mass,  $\mathbf{v}_c$  is the velocity of the center of mass, and  $\zeta$  is the bead drag coefficient ( $\zeta = \zeta \delta$ ). Equation 2.20 can be made dimensionless by scaling time with characteristic relaxation time  $\lambda$  and length with  $\sqrt{kT/H}$ , which is one third of the equilibrium dumbbell length. The resulting dimensionless equation then becomes

$$\text{De} \left( \frac{\partial \psi}{\partial t^*} + \mathbf{v}_c^* \cdot \frac{\partial \psi}{\partial \mathbf{r}_c^*} \right) = - \frac{\partial}{\partial \mathbf{Q}^*} \cdot \left\{ \text{De} \nabla^* \mathbf{v}^{*T} \cdot \mathbf{Q}^* \psi - \frac{\partial \psi}{\partial \mathbf{Q}^*} + \mathbf{F}^{*(c)} \psi \right\} \quad (2.21)$$

Once the diffusion equation is solved for the configurational distribution function  $\psi(\mathbf{Q}, t)$ , any average quantity of interest  $\langle \mathbf{B} \rangle$  can be computed as  $\int \mathbf{B}\psi(\mathbf{Q}, t)d\mathbf{Q}$ . The key is how to compute  $\psi(\mathbf{Q}, t)$ . Most of the direct simulations of the Fokker-Planck equations are based on weighted residual methods. How successful this approach is depends on how well one can approximate the distribution function in the Fokker-Planck equation by a set of basis functions. Spherical harmonics were used as basis functions in [52] and [53]. Spherical harmonics were used because they are the eigenfunctions of the operator in the Fokker-Planck equation at  $De = 0$ . Due to this fact, the use of the spherical harmonics basis functions yields an efficient solution at low Deborah numbers. However, as the Deborah number increases, the required number of basis functions also increases, which can significantly decrease efficiency of the algorithm. Spherical harmonics are not eigenfunctions of the operator in the Fokker-Planck equation for any value of  $De$  if the diffusion coefficient depends on the configurations of the molecules. Having observed the fact that the distribution function is highly localized for high values of  $De$ , Nayak [43] and Armstrong *et al.* [2] proposed using wavelets as a substitute for spherical harmonics. They used the Daubechies orthonormal scaling functions as basis functions and demonstrated both accuracy and convergence of material properties in simple shear flows for a wide range of  $De$ . A new robust technique based on the mixed wavelet-Galerkin/finite element approach was introduced in [55]. Starting with the mixed Galerkin-collocation method developed by Nayak, the authors first extended the method to incorporate a range of basis functions and to solve highly complex and nonlinear diffusion equations. Then, a numerical algorithm was developed based on a synthesis of a node-by-node decomposition strategy and an operator splitting time-integration algorithm. The resulting algorithm was shown to be robust for finite element calculations with non-constant Jacobian of the global-to-local coordinate transformation. Such calculations were impossible to perform with the previous implementation of Nayak ([43]). The authors also simulated liquid crystalline polymer in complex flows using the wavelet-Galerkin method. The so-called thermodynamically admissible reptation model (TAR) was used to perform multi-scale calculations, which are difficult to perform using Brownian dynamics (see Section 2.2.3) due to the presence of a reaction-like term in the diffusion equation.

### 2.2.2 Moment equation with closure approximation

It was discussed in Section 2.2.1 that the Fokker-Planck equation can be used to calculate directly the dynamics of the distribution function, and hence the evolution of molecular configurations. Alternatively, one can obtain a general evolution equation for any function of the internal coordinates,  $\langle \mathbf{B}(\mathbf{Q}) \rangle$ , by multiplying Equation 2.21 by  $\mathbf{B}(\mathbf{Q})$  and integrating over  $\mathbf{Q}$ . This so-called contraction operation has been the most popular approach in traditional finite element solvers. By choosing  $\mathbf{B} = \mathbf{Q}\mathbf{Q}$ , one obtains the following evolution equation for  $\langle \mathbf{Q}\mathbf{Q} \rangle$

$$\text{De} \langle \mathbf{Q}\mathbf{Q} \rangle_{(1)} = - \left\langle \mathbf{F}^{(c)} \mathbf{Q} \right\rangle + \delta \quad (2.22)$$

where  $\Xi_{(1)} \equiv \frac{\partial \Xi}{\partial t} + \mathbf{v} \cdot \nabla \Xi - \nabla v \cdot \Xi - \{\nabla v \cdot \Xi\}^T$  is the upper convected derivative of the second order tensor  $\Xi$ . The dimensionless form of the FENE force law ( $\mathbf{F}^{(c)} = \mathbf{Q}/(1 - Q^2/b)$ ) can be substituted into Equation 2.22 to obtain

$$\text{De} \langle \mathbf{Q}\mathbf{Q} \rangle_{(1)} = - \left\langle \frac{\mathbf{Q}\mathbf{Q}}{1 - Q^2/b} \right\rangle + \delta \quad (2.23)$$

Here, for simplicity of notation, asterisks over dimensionless quantities have been dropped, and  $b$  is defined as  $Q_0^2/(kT/H)$ . Equation 2.23 contains two unknowns, namely  $\langle \mathbf{Q}\mathbf{Q} \rangle$  and  $\left\langle \frac{\mathbf{Q}\mathbf{Q}}{1 - Q^2/b} \right\rangle$ . In order to solve for  $\langle \mathbf{Q}\mathbf{Q} \rangle$ , some kind of closure approximation is required to express  $\left\langle \frac{\mathbf{Q}\mathbf{Q}}{1 - Q^2/b} \right\rangle$  in terms of  $\langle \mathbf{Q}\mathbf{Q} \rangle$ . One of the simplest closure approximations was proposed by Peterlin, in which he replaced the average of a ratio of two quantities by ratio of two averages, i.e.  $\langle \mathbf{Q}\mathbf{Q}/(1 - Q^2/b) \rangle \approx \langle \mathbf{Q}\mathbf{Q} \rangle / (1 - \langle Q \rangle^2/b)$ . The approximated model is called FENE-P. The polymer contribution to the stress tensor can be calculated from the Kramers expression  $\boldsymbol{\tau}_p = \delta - \left\langle \mathbf{F}^{(c)} \mathbf{Q} \right\rangle$ , which has the following form for the FENE-P model:

$$\boldsymbol{\tau}_p = \delta - \frac{\langle \mathbf{Q}\mathbf{Q} \rangle}{1 - \langle Q \rangle^2/b} \quad (2.24)$$

Another popular closure approximation called FENE-PM, the expression for which is given in Section 2.1. Although closed models may look qualitatively similar to the ones without closure, they can sometimes lead to incorrect and even aphysical results for a given molecular structure. It was demonstrated in [17] and [24] that whereas a FENE dumbbell exhibits

stress-birefringence hysteresis, the so-called distributional hysteresis, which arises because the distribution function assumes different shapes during extension and relaxation thus leading to multiple values of stress for a given birefringence, no such hysteresis is observed when Peterlin kind of approximation is applied. The authors attributed it to the fact that hysteresis cannot possibly be observed for a model in which polymeric stress is written as a function of just the second moment of instantaneous end-to-end vector  $\mathbf{Q}$ . It must be kept in mind applying the FENE-P type of approximation is equivalent to assuming that the configurational distribution function has the form of a Dirac delta function. Despite the drawbacks of closure approximations, constitutive equations obtained in this way remain popular for simulating polymer flows in complex geometries because of the ease of their implementation into finite element solvers.

### 2.2.3 Stochastic approach

The third approach for incorporating molecular models into kinetic theory is through stochastic simulations. This is the approach taken in this research and will be described in more detail throughout the thesis. A Brownian dynamics simulation is essentially a time integration scheme for a stochastic differential equation. Statistical quantities such as averages of polymer configurations and polymer contribution to the stress tensor are computed as averages over a large ensemble of stochastic trajectories. Detailed theories and numerical algorithms of Brownian dynamics simulations are provided in [30].

A typical stochastic differential equation for a multi-dimensional Brownian particle is given in Equation 2.25.

$$d\mathbf{X} = \mathbf{A}(\mathbf{X}, t)dt + \mathbf{B}(\mathbf{X}, t) \cdot d\mathbf{W}(t) \quad (2.25)$$

where  $\mathbf{X}$  is a multi-dimensional random variable and  $\mathbf{W}(t)$  is Wiener process that accounts for the random displacement of the beads due to their collisions with solvent molecules. The Wiener process is a Gaussian process with zero mean and covariance  $\langle \mathbf{W}_{t_1} \mathbf{W}_{t_2} \rangle = \min(t_1, t_2)$ . A stochastic differential equation is a balance between a drift or deterministic term and a stochastic term (first and second terms on the right side of Equation 2.25, respectively). Using Itô calculus, it is possible to derive a diffusion equation that is mathematically equivalent to the stochastic differential equation. The diffusion equation would have the following general

form

$$\frac{\partial}{\partial t} p(\mathbf{x}, t) = -\frac{\partial}{\partial \mathbf{x}} \cdot [A(\mathbf{x}, t)p(\mathbf{x}, t)] + \frac{1}{2} \frac{\partial}{\partial \mathbf{x}} \frac{\partial}{\partial \mathbf{x}} : [\mathbf{D}(\mathbf{x}, t)p(\mathbf{x}, t)] \quad (2.26)$$

where  $p$  is the probability density function,  $x$  is the set of all coordinates, and  $\mathbf{D}$  is a positive semi-definite symmetric matrix given by  $\mathbf{D}(\mathbf{x}, t) = \mathbf{B}(\mathbf{x}, t) \cdot \mathbf{B}^T(\mathbf{x}, t)$ . A necessary condition that must be met if the Fokker-Planck equation approach is to be applicable is that the configuration space description stays constant throughout. This is not an issue in the stochastic approach. A model in which configuration space changes due to segments of a molecule breaking up into a number of smaller segments and subsequently recombining is the Adaptive Length Scale model discussed in Chapter 3. On the other hand, a stochastic approach is not applicable if there is a reaction term in the diffusion equation. While in the Fokker-Planck approach a reaction term is treated as an additional term in the diffusion equation, there is no trivial methodology that would allow one to derive the associated stochastic differential equation.

A stochastic differential equation relevant to the Brownian dynamics simulation of a polymer solution is the equation of motion for a bead. If the solution is modeled as a suspension of elastic dumbbells, then the equation for the relative positions of the beads  $\mathbf{Q}$  will take the following form:

$$d\mathbf{Q}(t) = \left( [\boldsymbol{\kappa}(t) \cdot \mathbf{Q}(t)] - \frac{2}{\zeta} \mathbf{F}^{(c)} \right) dt + \sqrt{\frac{4kT}{\zeta}} d\mathbf{W}(t) \quad (2.27)$$

If Equation 2.27 is made dimensionless and integrated using a forward Euler time-integration scheme the following expression for the equation of motion of a dumbbell is obtained

$$\mathbf{Q}(t + \Delta t) = \mathbf{Q}(t) + \left( \text{De} [\boldsymbol{\kappa}(t) \cdot \mathbf{Q}(t)] - \frac{1}{2} \frac{\mathbf{Q}\mathbf{Q}}{1 - \text{tr} \mathbf{Q}\mathbf{Q}/b} \right) \Delta t + \Delta \mathbf{W}(t) \quad (2.28)$$

where  $\Delta \mathbf{W}$  is now an independent Wiener process with zero mean and variance equal to  $\Delta t$ . Once the configurations are known, polymer stress can be calculated from the Kramers expression for the stress tensor, which has the following form for a FENE dumbbell model

$$\boldsymbol{\tau}_p = \delta - \frac{1}{N_{\text{traj}}} \sum_{i=1}^{N_{\text{traj}}} \frac{\mathbf{Q}_i \mathbf{Q}_i}{1 - \text{tr} \mathbf{Q}_i \mathbf{Q}_i / b} \quad (2.29)$$

While forward Euler is relatively easy to implement, it has a major drawback. When

applied to a nonlinear model such as a FENE dumbbell, for a finite time step, there is always a probability that the spring will stretch beyond its maximum allowable extension  $Q_0$ . One way to tackle this problem is to reject all moves that result in such outcome. Another way is to use an implicit time-integration scheme. One such scheme, called a predictor-corrector method, is described in [45]. Another advantage of using some kind of an implicit method is that it allows for much larger time steps to be taken, thus increasing the rate of convergence. Time-integration techniques of a stochastic differential equation as applied to the Adaptive Length Scale model will be discussed in Chapter 3.

As seen from Equation 2.28, Brownian dynamics simulations are most accurate at large Deborah numbers, which makes them a good complement to the direct solution of the Fokker-Planck equation, which, unless a set of basis functions that are capable of capturing efficiently the sharply peaked distribution functions is used, is most accurate at the low values of Deborah numbers. Stochastic simulations are a very powerful and often the only tool available for simulating molecules with large numbers of internal degrees of freedom. A commonly used time-integration algorithm for an elastic dumbbell called forward Euler is depicted in Figure 2-4. In this figure,  $i$  is the trajectory being simulated,  $t_n$  is the time,  $\Delta t$  is the time-step size,  $Q_i^{n+1}$  and  $Q_i^n$  are the extensions of the  $i^{th}$  spring at two consecutive times, and  $N_{traj}$  is the number of generated stochastic trajectories.

Brownian dynamics simulations are also useful for studying the effect of boundary conditions and of interactions between bounding surfaces and polymer molecules. For instance, in an application relevant to the fiber industry it may lead to a better understanding of instabilities such as melt fracture, shark skin, etc. Also, explicit molecular architecture such as found in branched or star polymers can be incorporated into the multi-bead-rod chain model and simulated with Brownian dynamics.

McLeish & Larson [40] were the first to introduce a single mode model called the pom-pom for branched polymers. The pom-pom model with the simplest branching architecture was developed in order to predict rheological properties of long-chain branched commercial melts, such as low-density polyethylene (LDPE). The constitutive equation in this model, which was derived by modifying the relaxation time and modulus of the Doi-Edwards model, can correctly predict extensional and shear rheologies. The pom-pom model was later modified by various

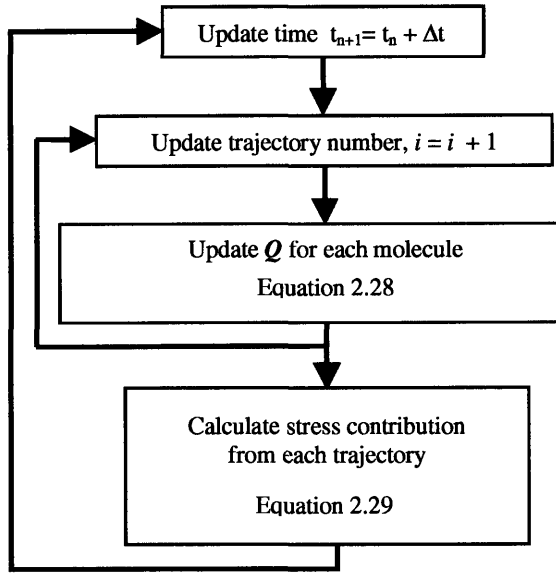


Figure 2-4: Forward Euler time integration algorithm for an elastic dumbbell.

researchers to improve its predictions. The negative aspect of this model is its inability to provide topological information. Lee and McHugh [34] performed Brownian dynamics simulations on a variety of hyperbranched polymers by modeling them as bead-spring-tridumbbells. The compact architecture of dendrimers potentially makes them useful as rheological modifiers, host molecules in drug delivery, dendritic catalysis, self-assembling liquid crystals, and synthetic analogs for biological molecules [35]. Most computational studies of dendrimers have focused on the role of branching and chain geometry for the static properties. In the above-mentioned study, Lee and McHugh proposed a coarse-grained bead-spring model for dendrimers, which incorporates stretching and bending potential. By performing Brownian dynamics simulations, they showed that the proposed model is capable of qualitatively describing many of the experimentally observed properties such as the Newtonian viscosity profile and a maximum in the intrinsic viscosity as function of the molecular weight. In addition, complicated effects such as hydrodynamic interactions, excluded volume, and anisotropic friction can in principle be studied rigorously through stochastic simulations.

As can be gathered from the above discussion, either direct simulation of the Fokker-Planck equation or a stochastic simulation must be performed if a closure approximation is to be

avoided. The relative merits of the two approaches were outlined by Ghosh [23] and are summarized in Table 2.1.

Issue	Fokker-Planck Approach	Stochastic Approach
Ease of solution at high De	Difficult	Simple
Ease of solution at low De	Simple	Difficult
Level of parallelization	Moderate-high	High
Ease of parallelization	Simple	Simple
Simulation of high DOF models	Difficult	Moderate
Applicability condition	Const. config. space description	Absence of reaction in FPE

Table 2.1: Comparison of the Fokker-Planck and the stochastic approaches in solving viscoelastic flow problems.

Entries in the first two rows of Table 2.1 have been explained in the preceding discussion. As can be gathered from the third and the fourth rows, both approaches lend themselves to relatively efficient parallelization. To understand the entries in the fifth row, one needs to look at how the operation counts scale with the number of internal degrees of freedom of a polymer chain. If each dimension of the Fokker-Planck equation is represented by the same number of basis functions, then without accounting for the LU decomposition, the number of operations per iteration/time step will scale as  $N_b^{2m}$ ,  $m$  being the number of degrees of freedom and  $N_b$  being the number of basis functions for each degree of freedom. In a stochastic approach, the problem is already decoupled, and the number of operations will scale as  $mN_{traj}$ ,  $N_{traj}$  being the total number of stochastic trajectories simulated. Therefore, in theory, for large enough  $m$ , the stochastic approach is more efficient than the Fokker-Planck approach even if  $N_{traj} > N_b$  and the multi-bead-rod/spring models in homogeneous flows can be simulated more easily by using Brownian dynamics.

In order to take advantage of the robustness of the Brownian dynamics simulations, one must first understand the limitations of this approach to simulating polymer molecules. A major issue with coupling any trajectory-based simulation, such as Brownian dynamics, with macroscopic flow calculations is the error in estimating the stress tensor at any given position. This is due to the fact that there does not exist a microscopic steady state as molecular configurations evolve continuously due to thermal motion. This results in fluctuations of stochastic trajectories with time even after macroscopic steady state is reached, which often makes convergence especially

difficult to achieve. To explore the possibility of improving the accuracy of simulations, it is helpful to look at formal results for statistical errors. From the central limit theorem, it is known that the error of a stochastic simulation scales with  $\sigma/\sqrt{N}$ , where  $\sigma$  is the variance of the underlying distribution and  $N$  is the size of the ensemble being simulated. One obvious way to decrease the error is to increase the ensemble size. This, however, is not very efficient, as increasing  $N$  by two orders of magnitude would only reduce the error by one order of magnitude. An alternative way to keep the error low is to reduce the variance by means of some variance reduction technique. The two main approaches, which are based on the use of a control variable and on importance sampling have been investigated by Öttinger *et al.* [46], Bonvin & Picasso [10], Melchior & Öttinger [41] and [42], and Doyle *et al.* [16] and are discussed briefly in the next two subsections.

#### 2.2.4 Importance sampling technique

The first attempts at variance reduction were based on the importance sampling techniques borrowed from the Monte-Carlo literature. In general, distribution functions for systems at or close to equilibrium are Gaussian. Thus, system points clustered near the peak of the distribution contribute most to the mean and least to the variance. On the other hand, points located in the tails of the distribution contribute mostly to the variance. If some prior knowledge of the distribution function is available, such as the case if a system is at equilibrium, system points can be sampled selectively from the vicinity of the peak. Importance sampling contributed tremendously to improved efficiency of many equilibrium simulations [45], but it is less useful for non-equilibrium systems, the distribution function for which is usually not known a priori.

#### 2.2.5 Control variable technique

The idea behind control variables is that they should have essentially the same fluctuations as the random variable of interest, but a vanishingly small average. Subtracting the control variable from the variable of interest will then reduce the fluctuations while leaving the average of the quantity unchanged. Two ways to construct the control variables, namely direct control and parallel process simulations, have been discussed by Melchior & Öttinger [41], [42]. If one is interested in studying systems that are only slightly perturbed from equilibrium, then the

equilibrium simulation, which is considered a parallel process simulation, may provide an ideal control variable.

## Chapter 3

# The Adaptive Length Scale Model (ALS)

The Kramers chain is arguably the best mesoscale molecular model for describing the physics of a dilute polymer solution. However, its many degrees of freedom make it impossible to use this model in complex flow simulations. The FENE dumbbell model, on the other hand, only has three degrees of freedom, namely the three components of its end-to-end vector  $\mathbf{Q}$ , and hence lends itself to use in complex flows; but as Ghosh *et al.* showed ([24]), it predicts the short time scale behavior in the startup of elongational flow poorly. The authors showed that FENE chains with only six springs mimic the dynamics of a Kramers chain (and hence the real polymer molecule) well. Therefore, one would think that using FENE chains is the solution because they are computationally much less expensive than the Kramers chain, but it is not necessarily the case. First, multiple springs are required for the first few units of strain when molecules are no longer in their equilibrium coil configurations. When the strain gets larger, most molecules subjected to elongational flow will unravel, and a single spring will be sufficient to model this behavior. Unfortunately, there does not exist a systematic way to switch to a different number of springs at a certain number of strain. Therefore, if one starts out with a five-spring chain, five springs will have to be used throughout the simulation, which of course, is not efficient. This problem becomes more severe in complex flows where the rate of deformation varies spatially. For example, in the contraction-expansion flow, molecules may

be deforming slowly near the centerline far upstream from the contraction region and only a few springs would be enough to resolve the polymer dynamics. However, the molecules will be subjected to very high deformation rates near the contraction region, and hence a much longer chain would be required. Ghosh *et al.* [25] argued that the ideal molecular model would have a single spring whose length scale would be able to adapt according to the kinematic history of the flow.

### 3.1 Model description

The Adaptive Length Scale (ALS) model was motivated by a mechanistic understanding of the behavior of a Kramers chain in the start-up of elongational flow. The FENE force law does not describe the end-to-end force law in a Kramers chain for strong flows because the Kramers chain with its many internal degrees of freedom is not capable of sampling its entire configuration space on the time scale of the flow. The polymer molecule in the ALS model is viewed as a set of identical segments that are each small enough to be stretched reversibly under the local flow conditions. As the molecule unravels, the segments combine so that the length of the segment increases, but the number of segments decreases in order to keep the contour length of the polymer constant. The adaptive length scale is thus defined as the contour length of a fragment of the polymer chain, the end-to-end force of which is described by the FENE force law. It was postulated that a fragment of the polymer that satisfies the condition  $\lambda_f \dot{\epsilon} = 1$ , where  $\lambda_f$  is the time constant of the fragment and  $\dot{\epsilon}$  is the extension rate, is locally equilibrated and is thus adequately described by the FENE force law. To minimize the complexity of the model, it was assumed that the orientations and lengths of all segments are identical, and the force in each segment is given by the FENE force law with the adaptive length scale being the maximum extension of the spring. The evolution of the adaptive length scale  $L$  with strain is summarized schematically in Figure 3-1. The length scale in the figure is made dimensionless by  $Q_0$ , which is the maximum extension of a spring if the whole molecule were represented by a dumbbell, that is, it is the overall contour length of the molecule. At low strains, when most molecules have coiled configurations, a single dumbbell serves as a good representation, and hence the adaptive length scale is equal to  $Q_0$ . At high strains and strain rates, the molecules

are nearly fully-stretched and a dumbbell is able to sample the entire configuration space on the time scale of the flow, and the adaptive length scale is again equal to  $Q_0$ . At intermediate strains, when molecules have kinked configurations, the adaptive length scale decreases, which means the molecular representation breaks down into a number of segments.

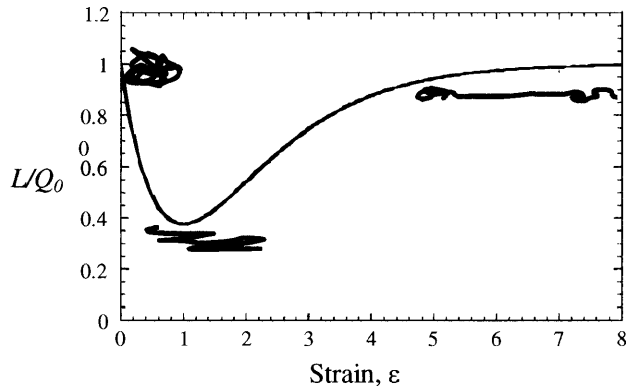


Figure 3-1: Evolution of the adaptive length scale  $L$ .

In the next section, the key governing equation of the ALS model will be presented first in dimensional form with brief explanations of the terms and then in dimensionless forms. First, the equations are developed that describe the adaptive length scale in the limit that instantaneous changes in the flow field lead to instantaneous changes in the molecular parameters. The quantities so derived are denoted with an asterisk to signify this idealization. For example, the adaptive length scale in this limit is denoted as  $L^*$ . Of course, real molecules require some finite time to react to the flow, and this fact is subsequently incorporated into the model. Asterisks will be dropped from quantities calculated using this correction. For more detailed information about the model, one can consult [23] and [25].

### 3.2 Governing equations

The contour length of the molecule always has to stay the same, and for that reason, the number of segments  $M_{\text{seg}}^*$  that the molecule will break down into is set equal to the contour length of

the entire molecule divided by  $L^*$  or

$$M_{\text{seg}}^* = \frac{(N-1)a}{L^*} \quad (3.1)$$

where the maximum extension of each spring is given by

$$Q_0 = \frac{(N-1)a}{M} \quad (3.2)$$

The number of beads, which is given by

$$N_{\text{bead}}^* = M_{\text{seg}}^* + 1 \quad (3.3)$$

as well as the number of segments given by equation 3.1 can be fractional. The drag coefficient  $\zeta_{\text{seg}}^*$  and the spring constant  $H_{\text{seg}}^*$  are functions of the number of segments. As the number of segments increases, each segment will represent a smaller section of the Kramers chain, which means that each spring must become stiffer. The spring modulus  $H_{\text{seg}}^*$  is proportional to the number of segments and thus inversely proportional to the number of links in the segment

$$H_{\text{seg}}^* = \frac{3M_{\text{seg}}kT}{(N-1)a^2} \quad (3.4)$$

With each segment representing fewer links in the Kramers chain, the time constant of each segment should also decrease according to

$$\lambda_{\text{seg}}^* = \frac{\zeta_{\text{seg}}^*}{4H_{\text{seg}}^*} = \frac{\lambda_d}{K^*} \quad (3.5)$$

where

$$K^* = \left( \frac{b_{\text{seg}}^*}{b_{\text{seg}}^* + 5} \right) \left( \frac{\sqrt{(b_{\text{max}} + 5)(b_{\text{max}} + 7)}}{b_{\text{max}}} \left\{ \frac{[2(M_{\text{seg}}^* + 1)^2 + 7][(M_{\text{seg}}^* + 1)^2 - 1]}{45} - \frac{12[(M_{\text{seg}}^* + 1)^4 - 1]}{45(M_{\text{seg}}^* + 1)(b_{\text{seg}} + 7)} \right\}^{1/2} \right) \quad (3.6)$$

The parameter  $b_{\text{seg}}^*$  is the dimensionless finite extensibility for a segment with maximum extension equal to the adaptive length scale  $L^*$  and is defined as

$$b_{\text{seg}}^* = \frac{H_{\text{seg}}^* L^{*2}}{kT} \quad (3.7a)$$

and

$$M_{\text{seg}}^* = \frac{b_{\text{max}}}{b_{\text{seg}}^*} \quad (3.8)$$

Equation 3.5 is identical to Equation 2.15 because Ghosh *et al.* assumed that the time constant of a segment  $\lambda_{\text{seg}}^* = \zeta_{\text{seg}}^*/4H_{\text{seg}}^*$  scales with the longest relaxation time of the polymer  $\lambda_d = \zeta_d/4H_d$  in the same way that the time constant  $\lambda_s$  of a spring in a FENE chain scales with the dumbbell time constant  $\lambda_d$ .

To propose an equation for the instantaneous adaptive length scale  $L^*$ , it was assumed that a fragment of a molecule can sample its entire configuration space if the time constant of that fragment is similar in magnitude to the time scale of the underlying flow. The equation then has the following form

$$\frac{Z}{\dot{\epsilon}} = \frac{\zeta_{\text{seg}}^*}{4H_{\text{seg}}^*/(1 - Q^2/L^{*2})} \quad (3.9)$$

The time constants of the segment and the underlying flow need to be similar, but not identical. Therefore,  $Z$  should be an order one constant, but its precise value is not set in the model. If  $Z \rightarrow \infty$  is chosen, then it means that the molecule is able to sample its entire configuration space for any flow strength, and hence FENE dumbbell model is recovered. If, in addition,  $b_{\text{max}} \rightarrow \infty$ , then the Hookean dumbbell will be recovered. The presense of the term  $(1 - Q^2/L^{*2})$  is included because even though at and near equilibrium this term is equal to unity, when the segment stretches close to its maximum extension, the relaxation time scale of the spring decreases because the spring modulus stiffens as  $(1 - Q^2/L^{*2})^{-1}$ .

Equation 3.9 can be made dimensionless with the longest time constant of a molecule  $\lambda_d$  and characteristic length  $\sqrt{kT/H_d}$ . The spring constant  $H_d$  is that for a dumbbell representing the entire molecule and is defined by Equation 3.4 with  $M = 1$  and all asterisks removed. The

dimensionless form of Equation 3.9 can then be written as

$$\frac{\text{We}}{K^*} \left( 1 - \frac{\hat{Q}^2 b_{\max}}{b_{\text{seg}}^* b_{\text{seg}}^*} \right) = Z \quad (3.10)$$

where  $\text{We} = \lambda_d \dot{\epsilon}$ .  $b_{\text{seg}}^*$  is defined to be piecewise continuous, which means that it equals the value given by Equation 3.10 if that value is less than  $b_{\max}$ . Otherwise,  $b_{\text{seg}}^*$  is set to  $b_{\max}$ .

As explained in the beginning of this section, the development of  $L^*$  and other asterisked quantities was based on the assumption that sudden changes in the flow field will result in instantaneous changes in these quantities. This, however, would yield to instantaneous changes in the number of segments and, therefore, to polymer stress "jumps", the existence of which has not been proved conclusively through experimental observations. The adaptive length scale  $L^*$  should therefore be thought of as a pseudosteady state value that the system tends toward, but which is not reached instantaneously. The evolution equation for the true value of the adaptive length scale  $L$  is the following ordinary differential equation

$$\frac{dL}{dt} = - \left| \mathbf{n} \times \frac{\mathbf{Q}}{|\mathbf{Q}|} \right| \frac{\text{We}^{\text{eff}} [1 - (Q^2/L^{*2})] (L - L^*)}{\lambda_d/K} + \frac{(Q_0 - L)}{\lambda_d/K} \quad (3.11)$$

The first term on the right hand side of Equation 3.11 is a stiffening term and the second term is a relaxation term. The stiffening term causes  $L$  to decrease towards  $L^*$  when the flow is initiated and the relaxation term makes the adaptive length scale value to return to  $Q_0$  when the flow is stopped. The effective Weissenberg number  $\text{We}^{\text{eff}}$  was used instead of  $\text{We}$  to enable the applicability of the ALS model to arbitrary flows, and not just uniaxial elongational flow, for which it was originally derived. The proposed definition of  $\text{We}^{\text{eff}}$  is

$$\text{We}^{\text{eff}} = \lambda_d \dot{\epsilon}^{\text{eff}} = \frac{1}{2} \lambda_d \max \left[ \text{Ei g}(\dot{\gamma}^{\text{eff}}) \right] \dot{\epsilon}^{\text{eff}} \quad (3.12)$$

where the two-dimensional version of the effective rate of strain tensor is given by

$$\dot{\gamma}^{\text{eff}} = \begin{pmatrix} 2\kappa_{11} & s(\kappa_{21} + \kappa_{12}) \\ s(\kappa_{21} + \kappa_{12}) & 2\kappa_{22} \end{pmatrix}; \quad s = (b_0/b_{\max})^{1/2} \quad (3.13)$$

and  $b_0$  is a fitting parameter that governs the onset of shear thinning behavior. The components

of the transpose of the velocity gradient tensor  $\boldsymbol{\kappa}$  are expressed in Protean coordinates ([1]) in which basis vectors are the unit tangent and unit normal vectors to the streamlines for a two-dimensional flow. It should be noted that Equation 3.11 is not derived rigorously in the kinetic theory framework, but is rather fundamentally motivated by simulations of Kramers chain behavior. The dimensionless form of Equation 3.11 is

$$\frac{db_{\text{seg}}}{d\hat{t}} = - \left| \mathbf{n} \times \frac{\hat{\mathbf{Q}}}{|\hat{\mathbf{Q}}|} \right| \text{We}^{\text{eff}} \left( 1 - \frac{\hat{\mathbf{Q}} \cdot b_{\text{max}}}{b_{\text{seg}}^* b_{\text{seg}}^*} \right) (b_{\text{seg}} - b_{\text{seg}}^*) K^* + (b_{\text{max}} - b_{\text{seg}}) K \quad (3.14)$$

Given the assumption that all segments are identical, it follows that the motion of each of these segments is governed by the same stochastic differential equation. Since each segment behaves like a FENE dumbbell, one would expect the dynamic motion of the ALS model to be similar to that of the FENE dumbbell with the exception that the drag coefficient, the spring constant, and the maximum extensibility in the former are functions of the number of segments. With this assumption in place, the equation of motion for a bead in the ALS model in dimensionless form is given by

$$d\hat{\mathbf{Q}} = \left[ \text{We} [\hat{\boldsymbol{\kappa}} \cdot \hat{\mathbf{Q}}] - \frac{1}{2} K \frac{\hat{\mathbf{Q}}}{\left( 1 - \frac{\hat{\mathbf{Q}} \cdot b_{\text{max}}}{b_{\text{seg}}^* b_{\text{seg}}^*} \right)} \right] d\hat{t} + \left( K \frac{b_{\text{seg}}}{b_{\text{max}}} \right)^{1/2} d\hat{\mathbf{W}} \quad (3.15)$$

The dimensionless birefringence is given by

$$\Delta n = \frac{5}{3} C n k T \left\langle \left( \frac{b_{\text{max}}}{\langle b_{\text{seg}} \rangle} \right)^2 (\hat{Q}_3 \hat{Q}_3 - \hat{Q}_1 \hat{Q}_1) \right\rangle \quad (3.16)$$

where  $C$  is given by Equation 2.5 and the polymer contribution to the stress tensor is calculated using the Kramers expression of the form given by Equation 2.29. The only difference is that all segments of the ALS model must be accounted for, and since all segments are identical, the stress is calculated by multiplying the contribution of an individual segment by the number of segments. If the polymer contribution to the stress tensor is made dimensionless by  $nkT$ , then

the total polymeric contribution to the stress is expressed in dimensionless form as

$$\hat{\tau}_p = \left\langle \frac{b_{\max}}{b_{\text{seg}}} \right\rangle \delta - \left\langle \frac{(b_{\max}/b_{\text{seg}})^2 \hat{\mathbf{Q}}\hat{\mathbf{Q}}}{1 - \frac{\hat{\mathbf{Q}}}{b_{\text{seg}}} \frac{b_{\max}}{b_{\text{seg}}}} \right\rangle \quad (3.17)$$

### 3.3 Closed form of the ALS model

Ghosh *et al.* proposed an approximated version of the ALS model in order for it to be usable in traditional finite element solvers. In order for the closed-form model to be consistent with kinetic theory, the derivation would have to be as follows. First, the Fokker-Planck equation that is equivalent to the governing equations of the ALS model (Eqs. 3.10, 3.14, and 3.15) would have to be derived using the Fokker-Planck/stochastic differential equation equivalence theorem (Eqn. 2.25 and 2.26). For the ALS model, the set of dependent variables denoted by  $\mathbf{X}$  consists of the three components of the end-to-end vector  $\mathbf{Q}$  as well as the maximum extensibility of a segment  $b_{\text{seg}}$ . Then, the evolution equation for  $\langle \mathbf{Q}\mathbf{Q} \rangle$  would have to be obtained by multiplying the Fokker-Planck equation by the configuration tensor  $\mathbf{Q}\mathbf{Q}$  and integrating over the configuration space. Finding the Fokker-Planck equation is complicated by the fact that the stochastic term  $\mathbf{B}(\mathbf{X}, t)$  for the ALS model is a complicated function of  $b_{\text{seg}}$  ( $\mathbf{B}(\mathbf{X}, t) = \sqrt{K b_{\text{seg}}/b_{\max}}$ ). Second derivatives of this function would have to be evaluated, which would yield a series of yet more complicated terms.

To avoid this difficulty, Ghosh *et al.* proposed to close the model by providing closed forms for each of the governing equations of the ALS model such that the properties of the approximate and original forms of the ALS model are similar. The closed forms of Equations 3.10, 3.14, 3.15, 3.16, and 3.17 are the following

$$\frac{\text{We}}{K^*} \left( 1 - \frac{\text{tr} \langle \hat{\mathbf{Q}}\hat{\mathbf{Q}} \rangle}{\langle b_{\text{seg}}^* \rangle} \frac{b_{\max}}{\langle b_{\text{seg}}^* \rangle} \right) = Z \quad (3.18)$$

$$\frac{d\langle b_{\text{seg}} \rangle}{d\hat{t}} = - \left| \mathbf{n} \times \begin{pmatrix} \langle \hat{Q}_1 \hat{Q}_1 \rangle^{1/2} \\ \langle \hat{Q}_2 \hat{Q}_2 \rangle^{1/2} \\ \langle \hat{Q}_3 \hat{Q}_3 \rangle^{1/2} \end{pmatrix} \frac{1}{(\text{tr} \langle \hat{Q} \hat{Q} \rangle)^{1/2}} \right| \text{We}^{\text{eff}} \left( 1 - \frac{\text{tr} \langle \hat{Q} \hat{Q} \rangle}{\langle b_{\text{seg}}^* \rangle} \frac{b_{\text{max}}}{\langle b_{\text{seg}}^* \rangle} \right) \quad (3.19)$$

$$\times (\langle b_{\text{seg}} \rangle - \langle b_{\text{seg}}^* \rangle) K^* + (b_{\text{max}} - \langle b_{\text{seg}} \rangle) K \quad (3.20)$$

$$\frac{d\langle \hat{Q} \hat{Q} \rangle}{d\hat{t}} = \text{We} \left\{ \hat{\boldsymbol{\kappa}} \cdot \langle \hat{Q} \hat{Q} \rangle + \langle \hat{Q} \hat{Q} \rangle \cdot \hat{\boldsymbol{\kappa}}^T \right\} - \frac{K \langle \hat{Q} \hat{Q} \rangle}{\left( 1 - \frac{\text{tr} \langle \hat{Q} \hat{Q} \rangle}{\langle b_{\text{seg}} \rangle} \frac{b_{\text{max}}}{\langle b_{\text{seg}} \rangle} \right)} + \left( K \frac{\langle b_{\text{seg}} \rangle}{b_{\text{max}}} \right) \boldsymbol{\delta} \quad (3.21)$$

$$\Delta n = \frac{5}{3} C n k T \left( \frac{b_{\text{max}}}{\langle b_{\text{seg}} \rangle} \right)^2 \langle \hat{Q}_3 \hat{Q}_3 - \hat{Q}_1 \hat{Q}_1 \rangle \quad (3.22)$$

$$\hat{\boldsymbol{\tau}}_p = \frac{b_{\text{max}}}{\langle b_{\text{seg}} \rangle} \boldsymbol{\delta} - \left( \frac{b_{\text{max}}}{\langle b_{\text{seg}} \rangle} \right)^2 \left\langle \frac{\langle \hat{Q} \hat{Q} \rangle}{1 - \frac{\text{tr} \langle \hat{Q} \hat{Q} \rangle}{\langle b_{\text{seg}} \rangle} \frac{b_{\text{max}}}{\langle b_{\text{seg}} \rangle}} \right\rangle \quad (3.23)$$

## Chapter 4

# Optimization of the ALS model

This chapter discusses ways to make the ALS model as efficient as possible in simple flow simulations, because when coupled with finite element calculations, Brownian dynamics simulations will occupy a significant fraction of the total computational time. Keeping in mind that the ALS model is significantly more complex than the FENE dumbbell model, the goal has been to make the simulation time as short as possible, ideally approaching the FENE limit. In addition to the stochastic differential equation and the polymer stress tensor equation, which are similar to those of the FENE dumbbell model, the ALS model involves two more governing equations. The first equation is a sixth-order nonlinear algebraic equation for  $b_{\text{seg}}^*$ , which is the limiting instantaneous finite extensibility of a segment, and the second one is an ordinary differential equation for the evolution of the actual finite extensibility,  $b_{\text{seg}}$ . The two approaches for optimizing the model have been (1) finding most efficient ways to solve the nonlinear equation for  $b_{\text{seg}}^*$  and (2) evaluating the use of semi-implicit time integration instead of the explicit one in the hope that the former one will allow for a much larger time-step size.

### 4.1 Solving for $b_{\text{seg}}^*$

The expression for the instantaneous maximum extensibility  $b_{\text{seg}}^*$  (Eq. 3.10) is a 6th order nonlinear algebraic equation, which can be rewritten as

$$f(b_{\text{seg}}^*) = \text{We} \left( 1 - \frac{Q^2 b_{\text{max}}}{b_{\text{seg}}^* b_{\text{seg}}^*} \right) - K^* Z \quad (4.1)$$

where from here onwards carets will be dropped, and it will be assumed that all quantities are dimensionless. Since this equation has to be solved for each stochastic trajectory ( $N_{traj} \sim O(10,000)$ ) for each time step, we expected that a large percentage of the total simulation time would be spend on solving this equation. Originally, the bisection method, which is described in the next subsection, was used.

#### 4.1.1 Bisection Method

In order for the bisection method to work, function  $f$  must be continuous, which is nearly always the case because  $f$  is usually derived from some physical model. Suppose now that we have an interval  $[a, b]$ , with  $f(a)$  and  $f(b)$  having different signs, or in other words:

$$f(a)f(b) < 0 \tag{4.2}$$

It follows then from elementary analysis that the interval  $[a, b]$  will contain at least one root of the function  $f$ . Suppose now that some approximation to this root  $c$  has been found, with  $a < c < b$ . There are now 3 possibilities for  $f(c)$ :

1.  $f(c) = 0$ ; The root has been found, but this is "infinitely unlikely" to occur on the first iteration,
2.  $f(a)f(c) < 0$ ;  $c$  is not the root, but it is now known that root lies in the interval  $[a, c]$ , and
3.  $f(b)f(c) < 0$ ; the root lies in the interval  $[c, b]$ .

The question that remains is how to find this approximation to the root  $c$ . Usually,  $c$  is taken to lie mid-way between  $a$  and  $b$ , and therefore the interval is halved on each iteration until solution is reached. The bisection method is guaranteed to find a solution if one exists, but the problem lies in the fact that the method has linear convergence rate and therefore may take a long time to find the solution within specified tolerance. When applied to the solution of the  $b_{seg}^*$  equation, it was noticed that up to 80% of the total simulation time was spent in the subroutine that solved this equation.

### 4.1.2 Newton's method

Although the nonlinear function given by Equation 4.1 is not well-behaved for negative values of  $b_{seg}^*$ , except for a singularity at  $b_{seg}^* = 0$ , it is monotonically increasing for the positive values of  $b_{seg}^*$  (see Figure 4-1). For that reason, we decided to use Newton's method in place of the previously used bisection method, hoping that its quadratic convergence would speed up the total simulation time.

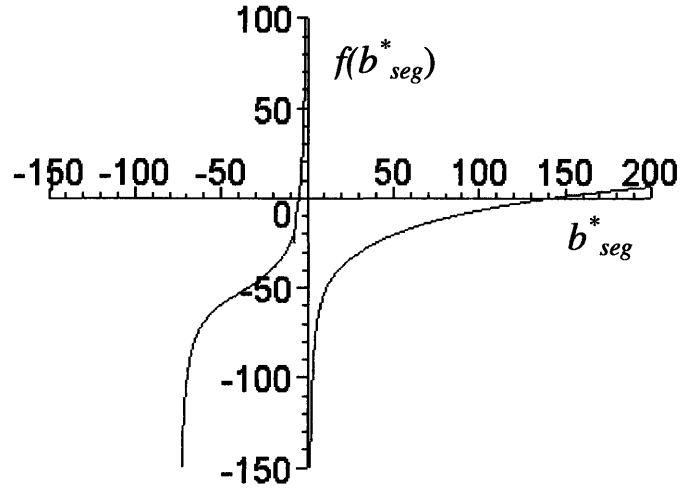


Figure 4-1: 6th order nonlinear algebraic function given by Equation 3.10 as a function of  $b_{seg}^*$ . A value of  $b_{max} = 150$  was used to generate this figure.

Newton's method, also called the Newton-Raphson method, is a root-finding algorithm that uses the first few terms of the Taylor series of a function  $f(x)$  in the vicinity of a suspected root. The Taylor series of  $f(x)$  about the point  $x = x_0 + \varepsilon$  is given by

$$f(x_0 + \varepsilon) = f(x_0) + f'(x_0)\varepsilon + \frac{1}{2}f''(x_0)\varepsilon^2 + \dots \quad (4.3)$$

Keeping terms to first order in  $\varepsilon$  only,

$$f(x_0 + \varepsilon) \approx f(x_0) + f'(x_0)\varepsilon \quad (4.4)$$

This expression can be used to estimate the amount of offset needed to land closer to the root

starting from an initial guess  $x_0$ . Setting  $f(x_0 + \varepsilon) = 0$  and solving Equation 4.4 for  $\varepsilon \equiv \varepsilon_0$  gives

$$\varepsilon_0 = -\frac{f(x_0)}{f'(x_0)} \quad (4.5)$$

which is the first-order adjustment to the root's position. By letting  $x_1 = x_0 + \varepsilon$ , calculating a new  $\varepsilon_1$ , and so on the process can be repeated until it converges to a root using

$$\varepsilon_n = -\frac{f(x_n)}{f'(x_n)} \quad (4.6)$$

Unfortunately, this procedure can be unstable near a horizontal asymptote or a local extremum. However, with a good initial choice of the root's position, the algorithm can be applied iteratively to obtain

$$x_{n+1} = x_n - \frac{f(x_n)}{f'(x_n)} \quad (4.7)$$

for  $n = 1, 2, 3, \dots$ . The error  $\varepsilon_{n+1}$  after  $(n + 1)$ th iteration is given by

$$\varepsilon_{n+1} = \varepsilon_n - \frac{f(x_n)}{f'(x_n)} \quad (4.8)$$

which can be rewritten as

$$\varepsilon_{n+1} = -\frac{f''(x_{n-1})}{2f'(x_{n-1})}\varepsilon_n^2 \quad (4.9)$$

Therefore, when the method converges, it converges quadratically. Unlike the bisection method, however, convergence is not guaranteed for the Newton's method, but rather is highly dependent on how good the initial guess  $x_0$  is.

Although for a given time step, each trajectory in the ALS model will have a different value of  $b_{\text{seg}}^*$ , because each one of these trajectories has been subjected to the same kinematic conditions, we do not expect these values to differ significantly, thus providing us with a good initial guess from one trajectory to the next. Newton's method is generally a good choice for solving nonlinear equations if one can provide an initial guess that lies within the radius of convergence. Since  $b_{\text{seg}}^*$  must lie in the region bounded by  $[0, b_{\text{max}}]$ , one choice is to use  $b_{\text{max}}$  as an initial guess for the first time Newton's method routine is executed, and after that to use  $b_{\text{seg}}^*$  from one trajectory as an initial guess for another one. This approach, however, did not

prove feasible given the nature of the nonlinear function in question. Due to the small slope of the curve at values of  $b_{seg}^*$  close to  $b_{max}$  (Figure 4-2), Newton’s method often ‘jumped’ to the negative values of  $b_{seg}^*$ , where there is always at least one real root. This situation occurred only when the value of the initial guess lay to the right of the true root. The way we chose to deal with this issue was by using a constant value of the initial guess, which was small enough that it was guaranteed to always lie to the left of the actual root.

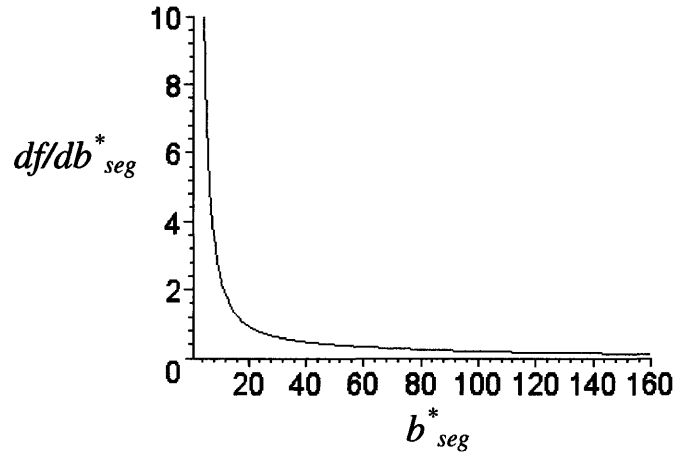


Figure 4-2: Plot of the first derivative of the function given by Equation 3.10.  $b_{max} = 150$ .

As expected, using Newton’s method offered tremendous computational savings as compared to the bisection method. For example, in a sample simulation of 10,000 trajectories in uniaxial elongational flow at  $We = 11.4$ , 45% of total simulation time is spent solving for  $b_{seg}^*$ . To put this number into perspective, if the bisection method is used, 75% of the total simulation time is spent on solving for  $b_{seg}^*$  (see Table 4.1), which makes it clear that the bisection method is inferior to the Newton’s method if the main objective is to minimize computation time.

### 4.1.3 Lookup table

The use of a lookup table for  $b_{seg}^*$  has also been considered. There were four parameters, namely  $tr\mathbf{Q}\mathbf{Q}$ ,  $We$ ,  $Z$ , and  $b_{max}$ , that needed to be tabulated. It was decided that instead of having a three-dimensional array of solutions, it was more efficient to keep  $Z$  and  $b_{max}$  constant for a

given table, thus varying only the first two parameters. This approach is justified because the values of  $Z$  and  $b_{\max}$  are kept the same throughout the simulation and are generally not changed very often between simulations. One problem with a lookup table is choosing the appropriate coarseness, especially since the value of  $\text{tr} \mathbf{Q} \mathbf{Q}$  for some individual trajectories can be extremely small at the beginning of the simulation. Given all this as well as the fact that the use of a lookup table did not offer considerable savings in computational efficiency as compared to the Newton's method, it was decided that lookup table was not the most efficient way to solve the  $b_{\text{seg}}^*$  equation.

#### 4.1.4 Polynomial expression

Since there exist a number of efficient techniques for finding real roots of polynomials, an attempt was made to put the nonlinear equation (Eq. 3.10) in such a form. Squaring the expression we get

$$\frac{Z^2 K^{*2} - 2\text{We}Z \left(1 - M_{\text{seg}}^{*2} Q^2 / b_{\max}\right) K^* + \text{We}^2 \left(1 - 2M_{\text{seg}}^{*2} Q^2 / b_{\max} + M_{\text{seg}}^{*4} Q^4 / b_{\max}^2\right)}{K^{*2}} = 0 \quad (4.10)$$

where  $K$ , which is defined by Equation 3.6, contains a term consisting of a square root of a ratio of polynomials. Hence, if Equation 4.10 is to be expressed in a form of a polynomial, only terms containing even powers of  $K$  are allowed. There is no obvious way to get rid of the middle term in this equation without generating another term that is some odd power of  $K$  and hence a spurious root that will lie in the range  $[0, b_{\max}]$ . The only way to convert Equation 4.10 to a polynomial form is by dropping this middle term altogether. Doing so will generate an 8th degree polynomial that needs to be solved for  $b_{\text{seg}}^*$  since  $b_{\text{seg}}^* = b_{\max} / M_{\text{seg}}^*$ . The problem with performing such an operation is that now the expression of interest is going to have a spurious positive real root with no way for us to differentiate it from the true solution. Hence, as promising as it seemed, it is not possible to put Equation 4.1 into a form of a polynomial in order to get a quick and easy solution. Of course, since this equation is not derived from the first principles, it may be possible to find a simpler, lower-order nonlinear expression, which will approximate well the equation we are interested in solving and which will be easy to solve. We tried to find such an expression by doing curve-fits. The problem lay in the fact that although it

was possible to approximate Equation 4.1 by a third-degree polynomial, the curve fit depended highly on the value of  $b_{\max}$ , which means that every time the value of  $b_{\max}$  is changed, the curve fitting has to be redone. Since our goal was to have a robust implementation of the ALS model that will be applicable for all kinds of flows and any values of model parameters, the approach of replacing Equation 3.6 by a polynomial was not pursued further.

#### 4.1.5 Approximated Newton's method

From the discussion in the preceding subsections, it is clear that Newton's method is the best approach for solving the nonlinear algebraic equation for  $b_{\text{seg}}^*$ . It was further noticed that the expression for  $K$  (Eq. 3.6) can be approximated very well by a third degree polynomial of the form  $K^* = c_1 M_{\text{seg}}^{*3} + c_2 M_{\text{seg}}^{*2} + c_3 M_{\text{seg}}^* + c_4$ . This expression works well because Equation 3.6 is not very sensitive to the value of  $b_{\max}$ . To obtain as accurate results as possible, the data fit to get the values  $c_1, \dots, c_4$  was performed for a few ranges of  $b_{\max}$ . For this implementation of the approximate version of the Newton's method, the simulation time was decreased by another 41% as compared to the original implementation of the Newton's method. It should be noted that some time saving is obtained if one solves for  $M_{\text{seg}}^*$  instead of  $b_{\text{seg}}^*$  even though these two quantities are related by a simple expression given by Equation 3.8.

Table 4.1 presents the percentage of time spent on solving for  $b_{\text{seg}}^*$ ,  $b_{\text{seg}}$ ,  $\mathbf{Q}$ , and  $\tau_p$  from Equations 3.10, 3.14, 3.15, and 3.17 (rows 1-4). These results were obtained for the start-up of uniaxial elongation flow at  $We = 11.4$  and  $b_{\max} = 120$ . Timing estimates for the start-up of shear flow are almost identical to the ones listed in Table 4.1. The first three columns of the table summarize results for the ALS model using the bisection method, the original Newton's method, and the approximate Newton's method. Results for the FENE dumbbell model are included in the last column for comparison. Lookup table results are not included because we have not found a way to avoid high inaccuracies in the results at low values of  $\text{tr}\mathbf{Q}\mathbf{Q}$ . One obvious way is, of course, to make the table finer, but that would negate all the time savings, and Newton's method would be more efficient.

In Figure 4-3, CPU requirements for various rheological models are compared. The models considered are the FENE dumbbell, the ALS model (using exact and approximate Newton's methods described above), a 5-mode FENE dumbbell model (see Chapter 6), and FENE chains

	Bisection	Orig. Newton	Approx. Newton	FENE dumbbell
$b_{\text{seg}}^*$	75%	46%	21%	N/A
$b_{\text{seg}}$	75%	15%	17%	N/A
$\mathbf{Q}$	11%	24%	38%	37%
$\tau_p$	2%	4%	3%	21%

Table 4.1: Breakdown on timing for the ALS and the FENE dumbbell models

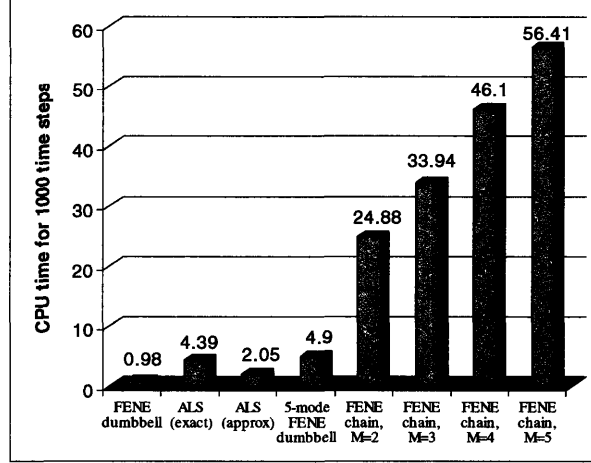


Figure 4-3: Timing comparison of various rheological models.

with 2, 3, 4, and 5 springs.

## 4.2 Time integration methods

Some effort was devoted to implementing a higher order time integration method into the homogeneous flow stress solver. A stochastic differential equation of the form  $d\mathbf{Q} = \mathbf{A}(t, \mathbf{Q})dt + B d\mathbf{W}$  can be integrated using an explicit, or Forward Euler method, using the following expression

$$\mathbf{Q}_{j+1} = \mathbf{Q}_j + \mathbf{A}(t_j, \mathbf{Q}_j)\Delta t + B\Delta \mathbf{W}_j \quad (4.11)$$

It is explicit because the end-to-end vector at the current time step  $\mathbf{Q}_{j+1}$  is a function of already known values that have been calculated in the step before. The problem with using an explicit, first order in  $\Delta t$  method for simulating nonlinear micromechanical models is that at any given time step, the length of a dumbbell (or a particular spring of a chain) may exceed

its maximum allowable extension, thus rendering the ‘move’ aphysical. One way to tackle this potential problem is by choosing the time step small enough that these occurrences become rare. In the case that it does take place, the ‘move’ must be rejected and the integration step repeated. A better way to solve the problem is by using a more stable time-stepping technique, such as a second order, semi-implicit predictor-corrector method proposed by Öttinger [45]. The predictor step is identical to the forward Euler, which for the ALS model is given by

$$\bar{\mathbf{Q}}_{j+1} = \mathbf{Q}_j + \left[ \text{We} [\boldsymbol{\kappa}_j \cdot \mathbf{Q}_j] - \frac{1}{2} K \frac{\mathbf{Q}_j}{\left(1 - \frac{\mathbf{Q}_j^2 b_{\max}}{b_{\text{seg}} b_{\text{seg}}}\right)} \right] dt + \left( K \frac{b_{\text{seg}}}{b_{\max}} \right)^{1/2} d\mathbf{W}_j \quad (4.12)$$

where  $\bar{\mathbf{Q}}_{j+1}$  is the prediction for  $\mathbf{Q}_{j+1}$ . The corrector step uses the Crank-Nicholson  $\theta$  family of approximations which approximates a weighted average of a time derivative of a dependent variable  $\mathbf{Q}$  at two consecutive time steps by linear interpolation of the values of the variable at the two time steps, i.e.

$$\frac{1}{2} \dot{\mathbf{Q}}_{j+1} + \frac{1}{2} \dot{\mathbf{Q}}_j = \frac{\mathbf{Q}_{j+1} - \mathbf{Q}_j}{\Delta t} \quad (4.13)$$

The corrector step for the ALS model is written as

$$\left( 1 + \frac{K}{4} \frac{\Delta t}{\left(1 - \frac{\mathbf{Q}_{j+1}^2 b_{\max}}{b_{\text{seg}} b_{\text{seg}}}\right)} \right) \mathbf{Q}_{j+1} = \mathbf{Q}_j + \frac{1}{2} \Delta t \times \quad (4.14)$$

$$\left( \text{We} [\boldsymbol{\kappa}_{j+1} \cdot \bar{\mathbf{Q}}_{j+1}] + \text{We} [\boldsymbol{\kappa}_j \cdot \mathbf{Q}_j] - \frac{K}{2} \frac{\mathbf{Q}_j}{\left(1 - \frac{\mathbf{Q}_j^2 b_{\max}}{b_{\text{seg}} b_{\text{seg}}}\right)} \right) \quad (4.15)$$

$$+ \left( K \frac{b_{\text{seg}}}{b_{\max}} \right)^{1/2} \Delta \mathbf{W}_j \quad (4.16)$$

In the above first-order predictor-corrector scheme, the Euler scheme is used as a predictor, and the corrector is obtained from the implicit Euler scheme by replacing  $\mathbf{Q}_{j+1}$  with the predicted value  $\bar{\mathbf{Q}}_{j+1}$  on the right-hand side of the implicit scheme. The predictor-corrector method requires a solution of a cubic equation at each time step for each trajectory. This method is about 3.5 times slower for a FENE dumbbell and about 1.5 times slower for the ALS model as

compared to the case when an explicit time-stepping method is used. If the FENE dumbbell model is used, the time-step can be increased by an order of magnitude, and therefore it is definitely advantageous to use the semi-implicit method. In the ALS model, however, time shows up in two governing equations, in the stochastic differential equation and in the evolution equation for the maximum extensibility  $b_{\text{seg}}$ . Even though the stochastic equation would support a larger time step size increase,  $\Delta t$  can only be increased by roughly a factor of two as compared to the explicit Euler method. A further increase in  $\Delta t$  renders the evolution equation for  $b_{\text{seg}}$  unstable, which causes the simulation to fail. Therefore, unless the  $b_{\text{seg}}$  equation is made more stable, there is no enormous benefit of using the predictor-corrector method in the ALS model.

### 4.3 Summary

In this chapter two approaches for optimizing the ALS algorithm have been described. In the first approach, different methods for solving the sixth-order nonlinear algebraic equation for  $b_{\text{seg}}^*$ , such as the bisection method, Newton's method, solution lookup table, conversion of the equation into a polynomial form and subsequent solution, and an approximated Newton's method were considered. Having investigated solution accuracy and CPU requirements of each method, it is suggested that the approximated Newton's method be used in simulating the ALS model in flow situations as it is only slightly over a factor of two slower than the corresponding FENE dumbbell simulation. One word of caution is that the coefficients  $c_1$  through  $c_4$  in the cubic fit to  $K^*$  (see Section 4.1.5) become more sensitive to values of  $b_{\text{max}}$  for smaller values ( $< 300$ ) of this parameter. Therefore, it is suggested that curve-fitting be performed for values of  $b_{\text{max}}$  in increments of 50 or 100 for  $b_{\text{max}} < 300$  to ensure final result accuracy.

The second approach aimed to decrease simulation time of the ALS model involved implementation of the predictor-corrector time-stepping algorithm into the homogeneous stress solver. The conclusion drawn from this implementation is that the predictor-corrector method results in tremendous CPU savings for the FENE dumbbell model and modest savings for the ALS model. As discussed in Section 4.2, whereas the stochastic differential equation allows an time-step increase by more than a factor of two as compared to the explicit Euler method, such an increase may render the evolution equation for  $b_{\text{seg}}$  unstable, thus causing the simulation to

fail. Suggestions for making this equation more stable are discussed briefly in Section 8.2.

## Chapter 5

# Behavior of the ALS model in simple flows

This chapter presents results of the ALS model in simple flow calculations. These results were obtained with the code-optimization techniques described in the previous chapter. Since the FENE force law is applicable if a polymer is slowly stretched, it is important to show that the ALS model reduces to the FENE dumbbell in the limit of low deformation rates. Transient shear and elongational viscosities are plotted in Figures 5-1 and 5-2, respectively, for the FENE dumbbell and the ALS models for  $b_{\max} = 150$ , and  $We = 0.5, 1, 5, 10.65$ , and  $50$ . As expected, the two models yield identical predictions for weak flows ( $We \leq 1$ ), and differences in predictions become more pronounced as the flow strength is increased.

An easy way to visualize why the ALS model reduced to the FENE dumbbell is by plotting the instantaneous number of segments  $M_{\text{seg}}^*$  vs the square of the dimensionless end-to-end vector  $Q$  at various values of the Weissenberg number. This relationship is depicted in Figure 5-3. The values of  $M_{\text{seg}}^*$  are obtained by solving the nonlinear algebraic equation for  $b_{\text{seg}}^*$  (Eqn. 3.10), where  $M_{\text{seg}}^* = b_{\max}/b_{\text{seg}}^*$ . The figure makes it clear that when  $We < 1$ ,  $M_{\text{seg}}^* = 1$  for all values of  $Q^2$ , which means that  $b_{\text{seg}}^* = b_{\max}$ , and the ALS model is identical to the FENE dumbbell model. Additionally, even for strong flows, as the value of  $Q^2$  gets close to its maximum extensibility, which happens in uniaxial elongational flows, the value of  $M_{\text{seg}}^*$  again approaches unity.

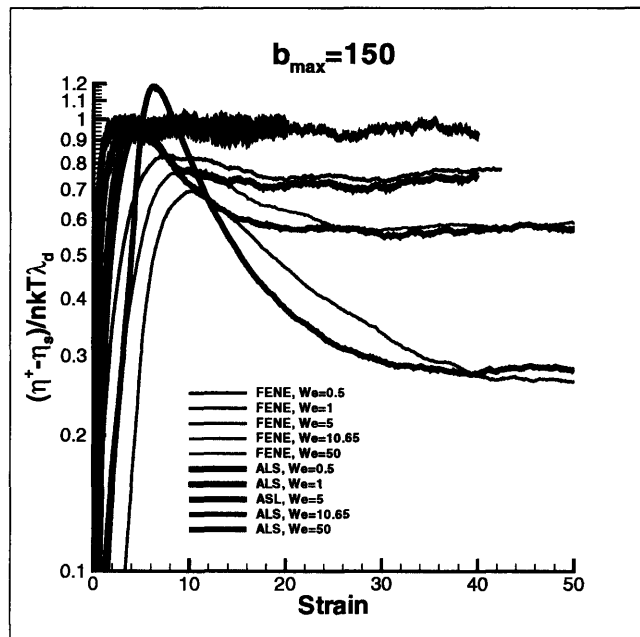


Figure 5-1: Transient polymer shear viscosity  $(\eta^+ - \eta_s) / nkT\lambda_d$  for the FENE dumbbell and the ALS models for  $b_{\max} = 150$ ,  $Z = 1$  and  $We = 0.5, 1, 5, 10.65, \text{ and } 50$ . FENE dumbbell results for  $We = 0.5$  and  $1$  coincide with the ALS results for corresponding values of  $We$ .

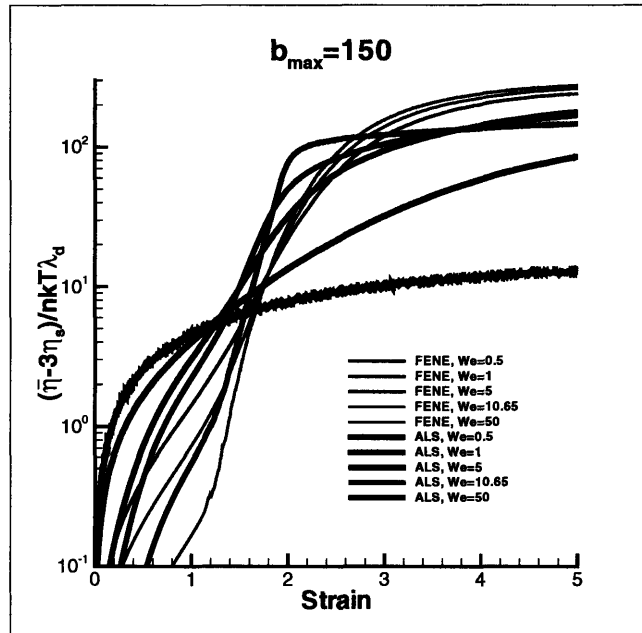


Figure 5-2: Transient polymer elongational viscosity  $(\bar{\eta}^+ - 3\eta_s)/nkT\lambda_d$  for the FENE dumbbell and the ALS models for  $b_{\max} = 150$ ,  $Z = 1$  and  $We = 0.5, 1, 5, 10.65$ , and  $50$ .

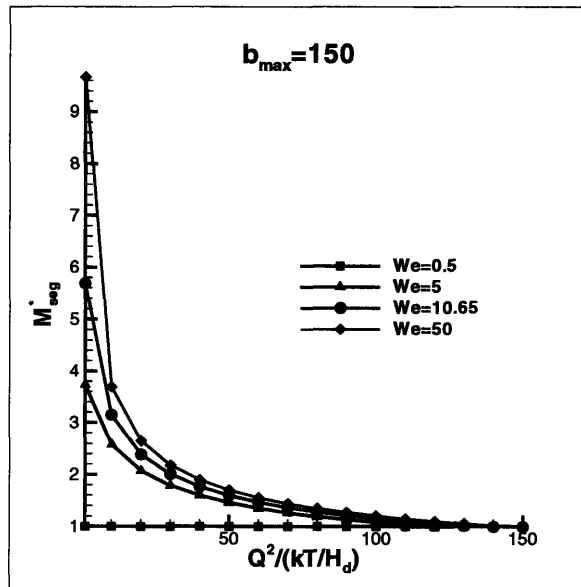


Figure 5-3: The dependence of  $M_{\text{seg}}^*$  on  $Q^2$  (made dimensionless by one-third of the equilibrium length of a FENE dumbbell) for various  $We$ .  $b_{\max} = 150$ ,  $Z = 1$ .

## 5.1 Rheological predictions of the ALS model

The optimized version of the ALS model is now used to predict its rheological properties in simple shear and extensional flows. The main goal of the ALS model was to predict the rapid extensional stress growth in the start-up of uniaxial elongational flow, which was greatly underpredicted by the FENE dumbbell model. As discussed in Chapter 3, the ALS model is able to capture the short length scale dynamics of the Kramers chain because it allows a polymer molecule to break down into a number of shorter segments when the flow gets strong enough such that the FENE force law no longer applies. The FENE dumbbell model, on the other hand, does not have enough degrees of freedom to capture these short length scale dynamics. As Figure 5-4 shows, the ALS model does, indeed, predict a stress growth that is in much better agreement with the Kramers chain. The FENE dumbbell model underpredicts stress growth at strains up to about 3. The ALS model, however, predicts a much longer time for the elongational viscosity to achieve steady-state than does the FENE dumbbell model. For example, for values of strain greater than 3, the Kramers chain and the FENE dumbbell models predict almost identical viscosities, whereas the value predicted by the ALS model is significantly lower. This feature of the ALS model needs to be investigated further although it may not be as big a problem as it seems at first because such high strains are not usually achieved in benchmark complex flows such as contraction-expansion flow or flow around a cylinder confined between two parallel plates. Figure 5-4 also shows that the two closed models, ALS-C and FENE-P, predict dynamics that are very different from the Kramers chain. The ALS-C model overpredicts elongational viscosity at low strains ( $\varepsilon < 1.5$ ), but then the curve flattens out and steady state is reached too slowly. The behavior of the FENE-P model is different from those predicted by all other models in that it greatly underpredicts stress growth for strains up to 3, and then it almost immediately achieves steady state. The last two observations prove that the physics predicted by closed models may be very different from the true physics, and therefore closure approximations must always be used with great caution. Kramers chain data in this chapter and the rest of the thesis are obtained from Doyle ([16], [15], and [17]).

Figure 5-5 shows the evolution of the polymer contribution to the transient shear viscosity  $\eta^+$  in the start-up of steady shear flow for a 50-bead Kramers chain, the equivalent ALS model, FENE dumbbell, ALS-C model, and the FENE-P dumbbell. As in the case of the start-up of

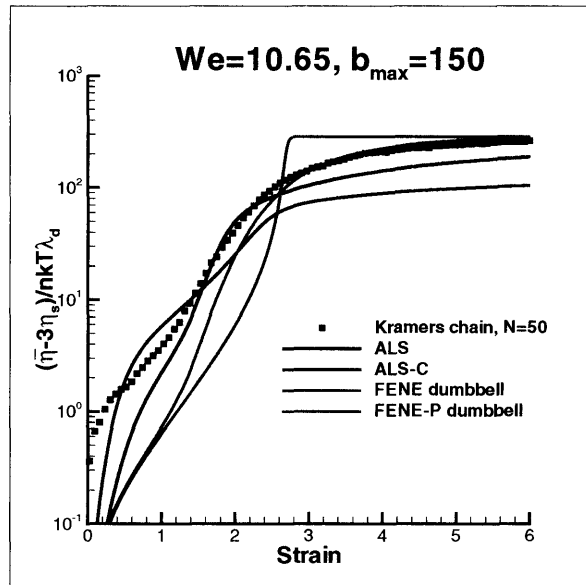


Figure 5-4: Dependence of transient polymer elongational viscosity on strain for a 50-rod Kramers chain and the corresponding forms of the ALS, ALS-C, FENE dumbbell, and FENE-P dumbbell models in start-up of uniaxial extensional flow for  $We = 10.65$ . The maximum extensibility for the elastic spring models,  $b_{\max}$  is 150. Kramers chain data are obtained from Doyle *et al.* [15].

elongational flow, the ALS model predicts shear stress growth that is in much better agreement with the Kramers chain than does the FENE dumbbell model. The maximum value of the transient viscosity for the ALS model occurs at a strain of 5, whereas the overshoot occurs later for the FENE dumbbell at a strain of 9. Viscosities predicted by the two models achieve steady state at roughly the same strain of 25. The steady-state value of the Kramers chain viscosity is about twice of that of the ALS model and the FENE dumbbell, the reason for this is explained in [25]. In short, this happens because Ghosh *et al.* chose to match the drag coefficient of the Kramers chain to that of the other two models by assuming that the characteristic relaxation time of the ALS and FENE dumbbell models is the same as the longest relaxation time of the Kramers chain. While this assumption allows us to match the infinite elongation-rate viscosities of all models, it causes a mismatch in other rheological property predictions such as the zero-elongation-rate viscosity (Figure 5-7), zero- and infinite-shear-rate viscosities (Figure 5-8), and zero- and infinite-shear-rate first normal stress coefficients (Figure 5-9).

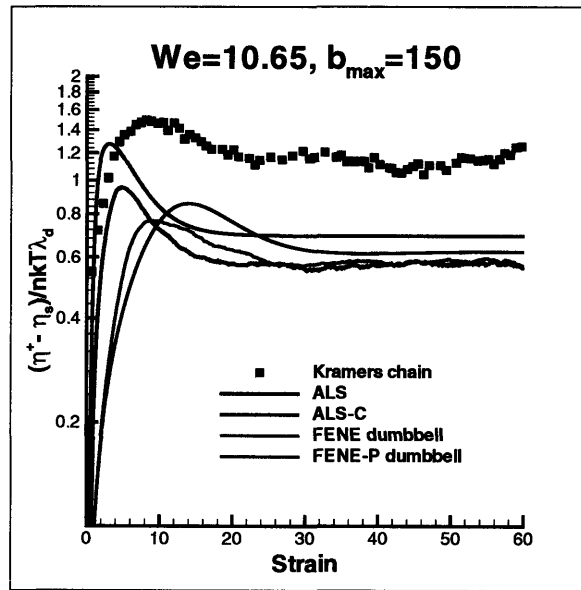


Figure 5-5: Dependence of polymer contribution to shear viscosity on strain for a 50-rod Kramers chain and the corresponding forms of the ALS, ALS-C, FENE dumbbell, and FENE-P dumbbell models in start-up of steady shear flow for  $We = 10.65$ . The maximum extensibility for the elastic spring models,  $b_{max}$  is 150.  $b_0 = 150$ . Kramers chain data are obtained from Doyle *et al.* [15].

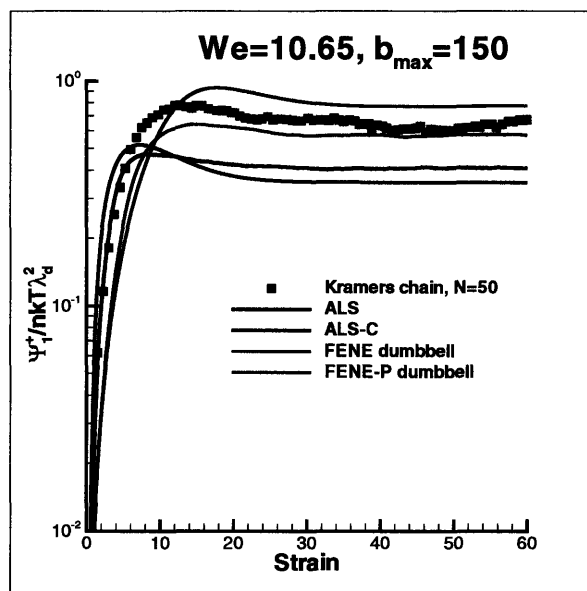


Figure 5-6: Dependence of the first normal stress coefficient  $\Psi_1^+$  on strain for a 50-rod Kramers chain and the corresponding forms of the ALS, ALS-C, FENE dumbbell, and FENE-P dumbbell models in start-up of steady shear flow for  $We = 10.65$ . The maximum extensibility for the elastic spring models,  $b_{max}$  is 150.  $b_0 = 150$ . Kramers chain data are obtained from Doyle *et al.* [15].

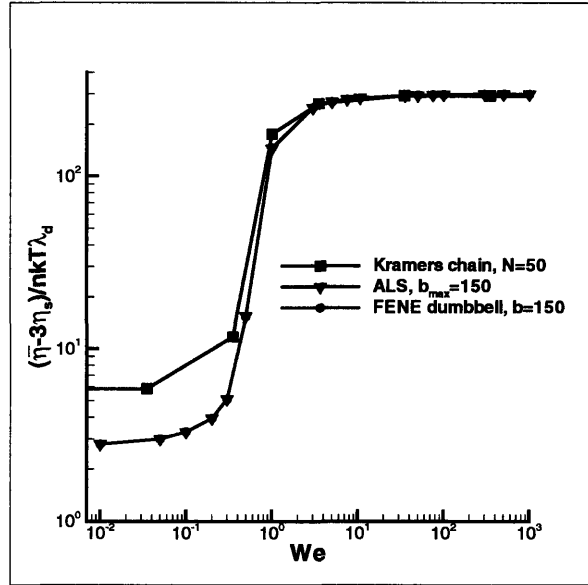


Figure 5-7: Dependence of elongational viscosity on  $We$  for a 50-rod Kramers chain and the corresponding forms of the ALS, ALS-C, FENE dumbbell, and FENE-P dumbbell models in steady elongational flow. The maximum extensibility for the elastic spring models,  $b_{\max}$  is 150. Kramers chain data are obtained from Doyle *et al.* [16].

One way to examine the evolution of stress and birefringence contributions from a polymer molecule during uniaxial elongation and subsequent relaxation is by plotting polymer contribution to the stress vs birefringence. Plotting data in this way provides an insight into the average polymer stress at a given average polymer conformation. Because a simple dumbbell only has three degrees of freedom, its birefringence is directly related to the end-to-end vector  $\mathbf{Q}$ . The simulation is run to a total strain of 6, after which the flow is stopped and stress is allowed to relax. During the start-up of the flow, the stress growth proceeds along the top branch of the curve. When the flow is stopped, the stress relaxes along the lower branch. Hence, there exists a hysteresis. As can be seen in Figure 5-10, the ALS model underpredicts the hysteresis, and the FENE dumbbell model overpredicts it when compared to the Kramers chain model. Doyle *et al.* [17] showed that the degree of hysteresis for the FENE dumbbell model increases with increasing  $We$ . The two closed models, ALS-C and FENE-P, on the other hand, do not exhibit

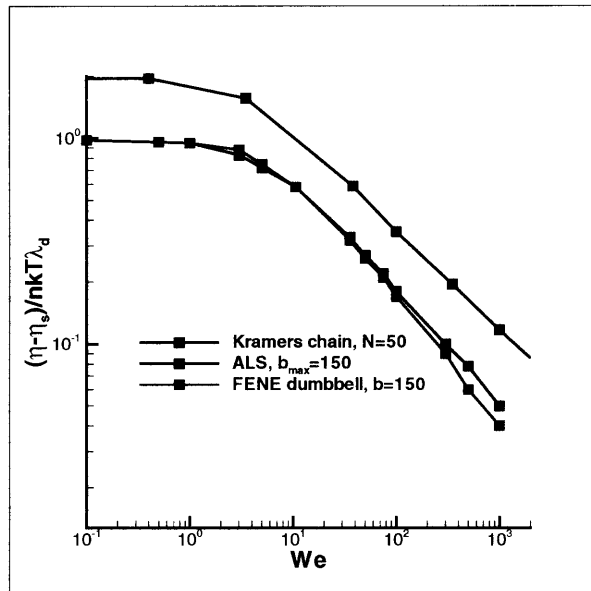


Figure 5-8: Dependence of viscosity on  $We$  for a 50-rod Kramers chain and the corresponding forms of the ALS, ALS-C, FENE dumbbell, and FENE-P dumbbell models in steady shear flow. The maximum extensibility for the elastic spring models,  $b_{max}$  is 150.  $b_0 = 150$ . Kramers chain data are obtained from Doyle *et al.* [16].  $b_0 = 150$ .

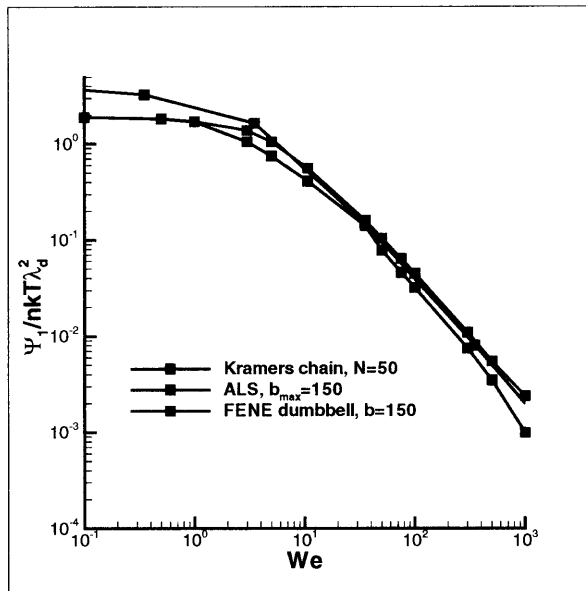


Figure 5-9: Dependence of first normal stress coefficient on  $We$  for a 50-rod Kramers chain and the corresponding forms of the ALS, ALS-C, FENE dumbbell, and FENE-P dumbbell models in steady shear flow. The maximum extensibility for the elastic spring models,  $b_{max}$  is 150. Kramers chain data are obtained from Doyle *et al.* [16].  $b_0 = 150$ .

hysteresis because of preaveraging. In fact, Doyle *et al.* state that stress-birefringence hysteresis cannot be observed for any model that expresses the polymer contribution to the stress as a function of the second moment of the distribution function,  $\langle \mathbf{Q}\mathbf{Q} \rangle$ , alone. To understand why this happens, it is helpful to know the origin of the stress-birefringence hysteresis. All three models in Figure 5-10 possess the so-called distributional hysteresis, which arises because the distribution function assumes different shapes during extension and relaxation thus leading to multiple values of stress for a given birefringence. In the FENE dumbbell model, for example, during the start-up of extensional flow, the distribution of dumbbell lengths is very broad and is not approximated well as a Gaussian. At steady-state and during relaxation, on the other hand, the distribution is nearly Gaussian, thus resulting in hysteresis. By preaveraging a model using a Peterlin-type approximation, it is assumed that the distribution is Gaussian, and hence no distributional hysteresis can be observed.

The same explanation for the distributional hysteresis is true for the Kramers chain and the ALS model, but there exists an additional, configurational hysteresis for the Kramers chain ([17]), which arises because molecules tend to assume different configurations during extension and relaxation. Sample chain configurations for the start-up of extensional flow at  $We = 10.65$  and subsequent relaxation are shown in Figure 5-11.

## 5.2 Parameter dependence

As explained in Chapter 3, the ALS model has two adjustable parameters, namely  $Z$  and  $b_0$ . In order to keep the total length of the molecule represented by the ALS model constant, the value of  $b_{\max}$  is fixed once the number of beads in the Kramers chain is chosen, and hence we do not consider  $b_{\max}$  an adjustable parameter. In this section, the effects of varying  $Z$  and  $b_0$  are examined.

The effect of varying  $Z$  on the transient extensional viscosity in the start-up of steady uniaxial elongation is depicted in Figure 5-12. As the figure shows, the viscosity for the values of  $Z \neq 1$  is smaller than that for  $Z = 1$  for strains less than 2.2, and the relationship is reversed for larger strains. In order to confirm that the ALS model reduces to the FENE dumbbell model for large values of  $Z$ , the results for the latter are included in Figure 5-12 as well. As

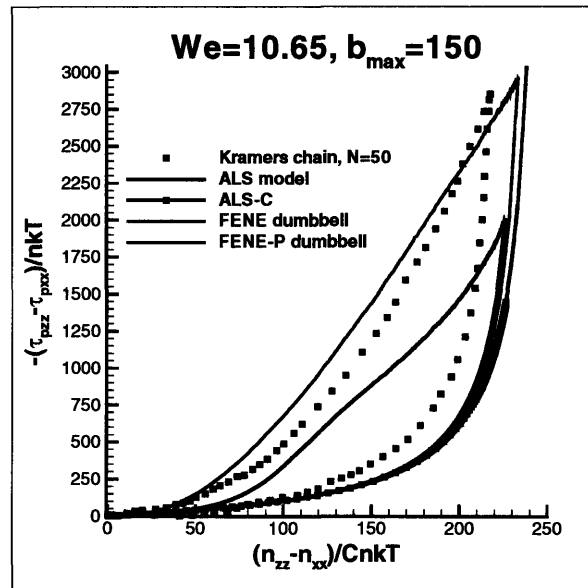


Figure 5-10: Polymer stress vs. birefringence for start-up of elongational flow up to  $\varepsilon = 6$  and subsequent relaxation. The results are shown for the Kramer's chain with  $N = 50$ , the ALS, ALS-C, FENE dumbbell, and FENE-P dumbbell models with  $b_{\max} = 150$ . Kramer's chain data are obtained from Doyle *et al.* [17].

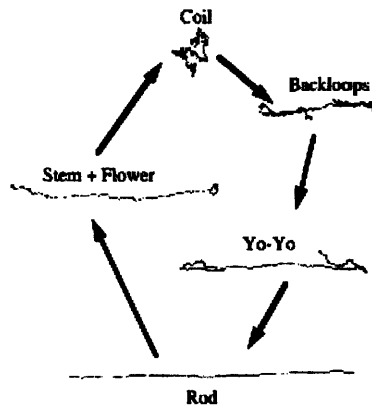


Figure 5-11: Sample chain configurations during start-up of extensional flow at  $We = 10.65$  and subsequent relaxation. During start-up the chain follows the right hand side path, and the left hand side path is followed during relaxation. Reproduced from [17]

expected, the curves corresponding to the ALS model with  $Z = 10$  and the FENE dumbbell model coincide for the whole range of strain values.

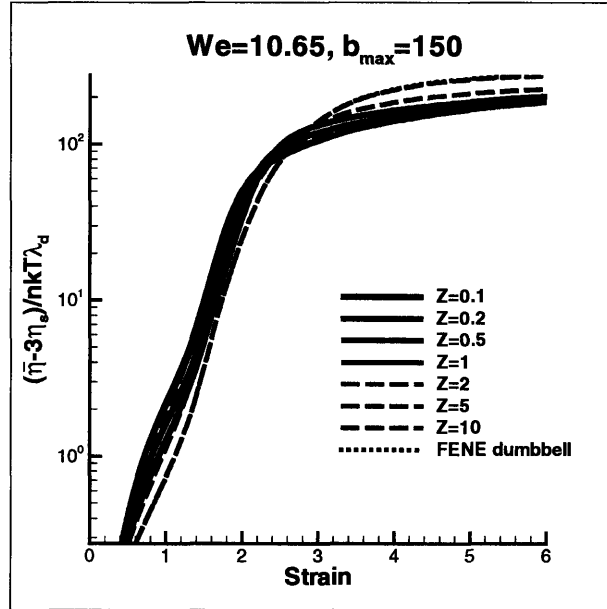


Figure 5-12: Dependence of polymer contribution to the elongational viscosity on strain in the ALS model for values of  $Z = 0.1, 0.2, 0.5, 1, 2, 5, 10$ .  $We = 10.65$  and  $b_{\max} = 150$  are held constant.

The polymer contribution to the transient viscosity  $((\eta^+ - \eta_s)/nkT)$  is displayed in Figure 5-13 as a function of strain for different values of  $Z$ . As  $Z$  is decreased from the value of unity, the viscous stress growth becomes slower and the overshoot becomes smaller as well and occurs at higher values of strain. The same behavior of the transient viscosity is exhibited as  $Z$  is increased from 1 to 10. From theory of the ALS model, one would expect the extensional and viscous stress growth to become slower with increasing  $Z$ , eventually reaching the FENE dumbbell limit as  $Z \rightarrow \infty$ , which is confirmed by this figure where the viscous stress growth predicted by the ALS model with  $Z = 10$  is very close to that predicted by the FENE dumbbell model. However, one would expect to observe the opposite effect as  $Z$  is decreased, i.e. the stress growth should become faster, because it would mean that the molecule breaks down into a larger number of segments for a given flow strength than it would for  $Z = 1$ . Results presented in Figure 5-13, however, indicate that stress growth slows down with decreasing values of  $Z$ .

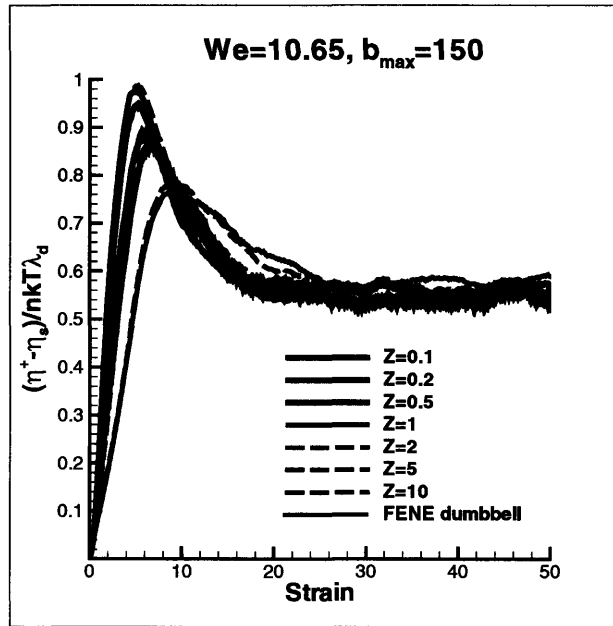


Figure 5-13: Dependence of polymer contribution to shear viscosity on strain in the ALS model for values of  $Z = 0.1, 0.2, 0.5, 1, 2, 5, 10$ .  $We = 10.65$  and  $b_{max} = 150$  are held constant.  $b_0 = 150$ .

This behavior needs to be investigated further in future work.

Figures 5-14 and 5-15 show the maximum number of segments that the ALS molecule breaks down into as a function of  $Z$  for steady elongational and shear flows, respectively. As expected, the maximum number of segments is higher for the elongational flow, and for values of  $Z > 10$ , the maximum number of segments is 1, which means that the value of  $Z$  is large enough and the FENE dumbbell model is recovered.

Finally, the effect of varying the  $b_0$  parameter on the polymer contribution to the shear viscosity is examined. The value of  $b_0$  does not have any effect on the uniaxial elongational flow because the ALS model was designed for this kind of flow. Therefore, this parameter only arises in arbitrary flows (see Eqns. 3.12 and 3.13). As Figure 5-16 shows, the effect of  $b_0$  is not very large and is non-monotonic. For example, the initial viscous stress growth is faster the higher the value of  $b_0$  is, but the behavior is reversed after the overshoot. Also, the steady state values of shear viscosity for  $b_0 = 30, 60, 90$ , and  $120$  are identical and lower than the value at  $b_0 = 150$ .

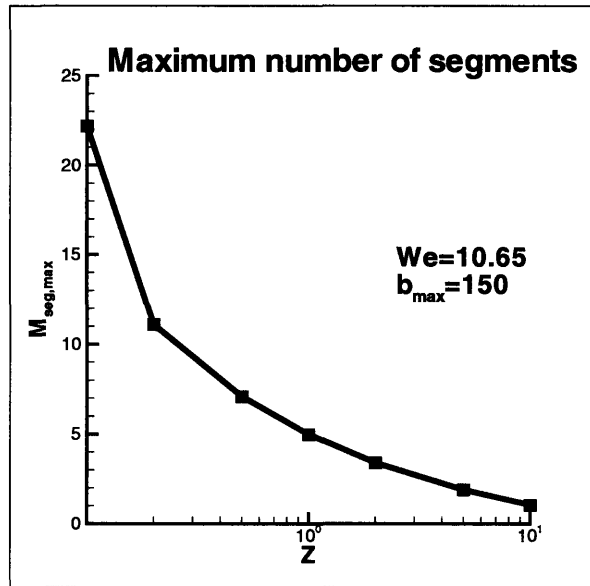


Figure 5-14: Dependence of the maximum number of segments  $M_{seg,max}$  on  $Z$  for uniaxial elongational flow at  $We = 10.65$  and  $b_{max} = 150$ .

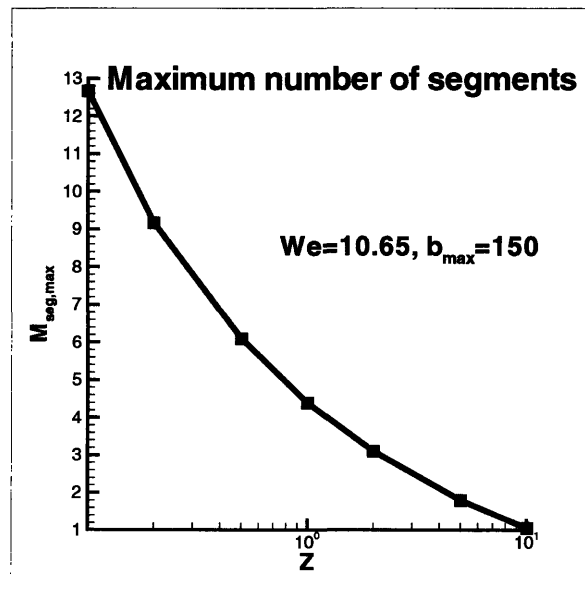


Figure 5-15: Dependence of the maximum number of segments  $M_{seg,max}$  on  $Z$  for simple shear flow at  $We = 10.65$  and  $b_{max} = 150$ .

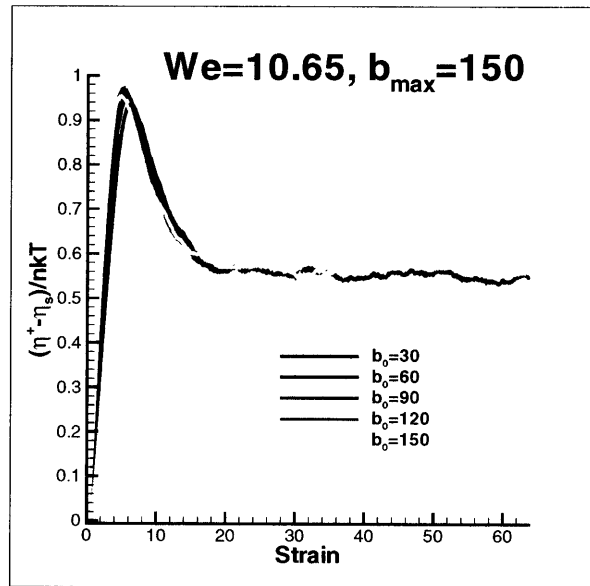


Figure 5-16: Dependence of transient polymer viscous stress growth coefficient  $\eta^+$  on strain for a 50-rod Kramers chain and the corresponding forms of the ALS, ALS-C, FENE dumbbell, and FENE-P dumbbell models in start-up of steady shear flow for  $We = 10.65$ . The maximum extensibility for the elastic spring models,  $b_{\max}$ , is 150.

## Chapter 6

# Multi-mode models

It has been explained in previous chapters that real polymer molecules possess a spectrum of relaxation times, which can be captured by a detailed molecular model such as a Kramers chain. The commonly used FENE dumbbell model does not have enough degrees of freedom to be able to capture this spectrum, whereas the ALS model allows a molecule to break down into a number of segments, each having a relaxation time that is smaller than that of the original dumbbell. However, most polymeric solutions are not monodisperse, i.e. they do not consist of polymer molecules of identical lengths and hence molecular weights, but rather a solution may contain molecules of the same chemical structure but with many different molecular weights and therefore relaxation times and contour lengths. This spectrum of relaxation times and contour lengths may be captured by a multi-mode model, in which the modes are typically assumed to be independent, and stress is calculated as a linear superposition of stresses given by individual modes.

When working with a multi-mode model, one must first perform a linear viscoelastic fit in order to obtain the relaxation time  $\lambda_i$  and contribution to viscosity  $\eta_{p,i}$  for each mode  $i$ . The experimental data used in this chapter are obtained for the 0.025 wt% PS solution which was used in the axisymmetric 4:1:4 contraction-expansion geometry by Rothstein *et al.* [49]. By performing a curve fit to the dynamic data, the authors found the solution's zero shear-rate viscosity to be 22.75 Pa sec, 21 Pa sec of which was due to the solvent and the rest to the polymer. Figure 6-1 shows the linear viscoelastic fit of the dynamic viscosity to this experimental data. The plot on the left is the fit with a single-mode dumbbell model having a

relaxation time of 1.866. The solvent used in [49] is a low molecular weight polystyrene with a relaxation time of 0.00245 seconds, which is the reason that the single-mode model is able to capture the dropoff in the dynamic viscosity at high frequencies. Therefore, technically the solvent would also be considered a mode, but in this chapter, when a model is said to contain  $n$  modes, it means that there are  $n$  modes plus the solvent mode. The plot on the right shows the same fit, but with a 4-mode model. The relaxation times for each mode were chosen such that they span a large enough range of frequencies in order to obtain the best fit possible. It is clear from the figure that the 4-mode model provides a much better fit as compared to the single-mode model.

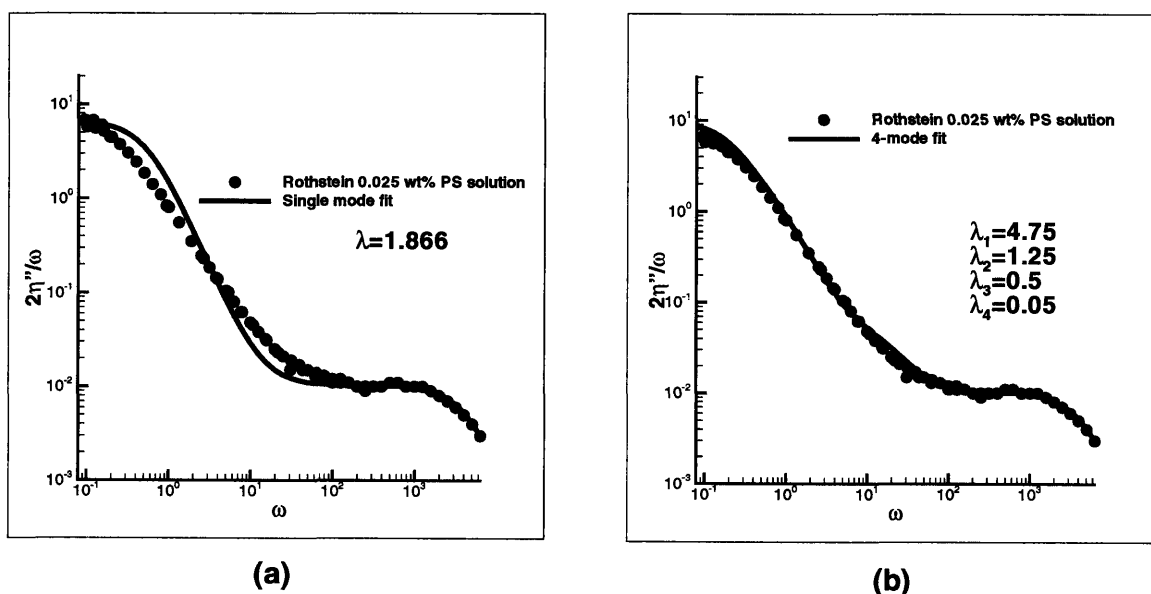


Figure 6-1: Linear viscoelastic fit to the experimental data by Rothstein [49]: (a) single-mode fit, (b) 4-mode fit.

Having chosen the set of relaxation times and individual modes' contributions to the viscosity, it is now necessary to determine the maximum extensibility  $b_{\max}$  for the models. Figure 6-2 shows data-fitting to the dimensionless extensional viscosity, defined by the Trouton ratio as  $\bar{\eta}^+/\eta_0$ , as a function of strain,  $\dot{\epsilon}t$ , for four different values of  $b_{\max}$ . The simulation results are presented for the single-mode ALS model with different values of the parameter  $Z$  and the single-mode FENE dumbbell model. The best value of  $b_{\max}$  for both models is 7,744. Given

the fact that strains larger than 2.75 are not achieved in the experimental set-up in [49], it makes sense to get as good a fit as possible for strains below that value, which is achieved for the ALS model with  $Z = 0.5$ . The same fit but for a 4-mode ALS model and a 4-mode FENE dumbbell model is depicted in Figure 6-3. Comparison of Figures 6-2 and 6-3 makes it clear, that not much benefit is obtained by extending the single-mode FENE dumbbell model to a 4-mode model. The use of a multi-mode ALS model, on the other hand, results in a better fit as compared to the single-mode fit, with the set of parameters summarized in Table 6.1. This set of parameters, however, results in a poor fit to the steady shear rheology. It must be kept in mind, though, that the zero-shear viscosity in [49] was obtained via a fit to the dynamic data, which the authors claim tends to be somewhat lower than the steady-state shear viscosity at very low shear rates.

Mode	$b_{\max}$	$Z$
1	12,000	0.5
2	7,000	0.5
3	5,000	0.5
4	1,000	0.5

Table 6.1: Set of parameters for a 4-mode ALS model resulting in the best fit to the transient uniaxial elongation experimental data of Rothstein et al.

It was shown in Chapter 5 that the ALS model is able predict the initial extensional stress growth in the startup of uniaxial elongation, which is in much better agreement with the Kramers chain results than the FENE dumbbell. Figure 6-4 shows a plot of elongational viscosity as a function of strain for these three models as well as a 5-mode FENE dumbbell model and a 5-spring FENE chain for comparison. When the ALS model with  $b_{\max} = 150$  is used to simulate a uniaxial elongational flow with  $We = 10.65$ , which is what was done to obtain Figure 6-4, it predicts that a polymer molecule will at most break down into five segments. To match this, a five-mode FENE dumbbell model was used, in which the time constant for mode  $i$  is identical to the time constant of an individual segment of the ALS model at a time when the molecule in the latter model is broken down into  $i$  segments ( $\lambda_i = \lambda_d/K$ ,  $\lambda_d$  is the time constant of a dumbbell and  $K$  is given by Equation 3.6 with asterisks removed). The maximum extensibility of mode  $i$ ,  $b_i$ , is given by  $b_{\max}/i$ . The figure indicates that the five-spring FENE chain agrees remarkably well with the Kramers chain, which we take as a benchmark model.

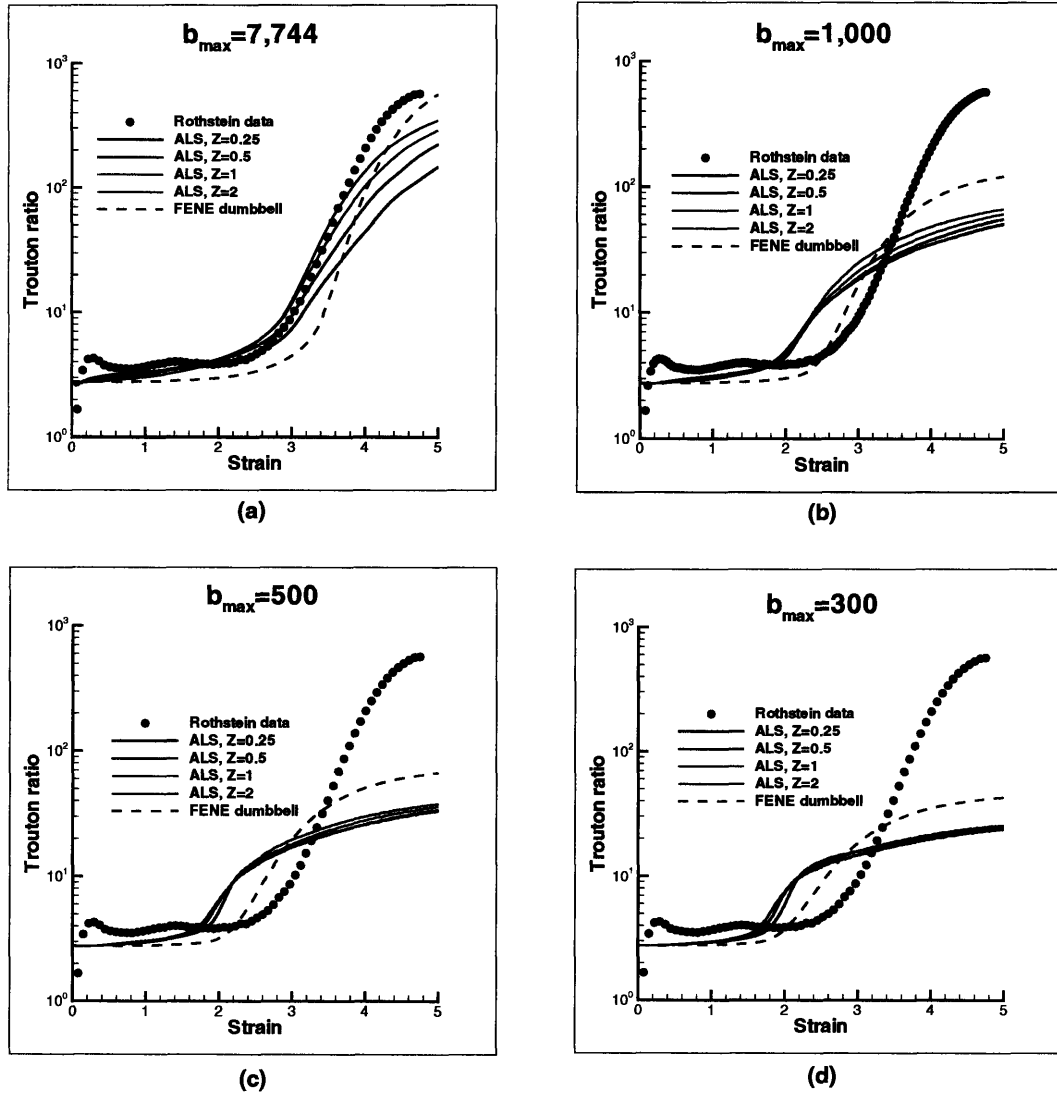


Figure 6-2: Single-mode data-fitting to experimental data in order to find the best value of  $b_{\max}$ . The included results are: i) experimental data with 0.025 wt% PS solution ([49]), simulation results with a single-mode ALS model with  $Z = 0.25, 0.5, 1$  and  $2$ , and simulation results with a single-mode FENE dumbbell model. (a)  $b_{\max} = 7744$ , (b)  $b_{\max} = 1000$ , (c)  $b_{\max} = 500$ , (d)  $b_{\max} = 1000$ . Trouton ratio is defined as  $\bar{\eta}^+/\eta_0$ , where  $\bar{\eta}^+$  is the transient extensional viscosity and  $\eta_0$  is the zero-shear-rate viscosity;  $\dot{\epsilon} = 9.1$  sec.

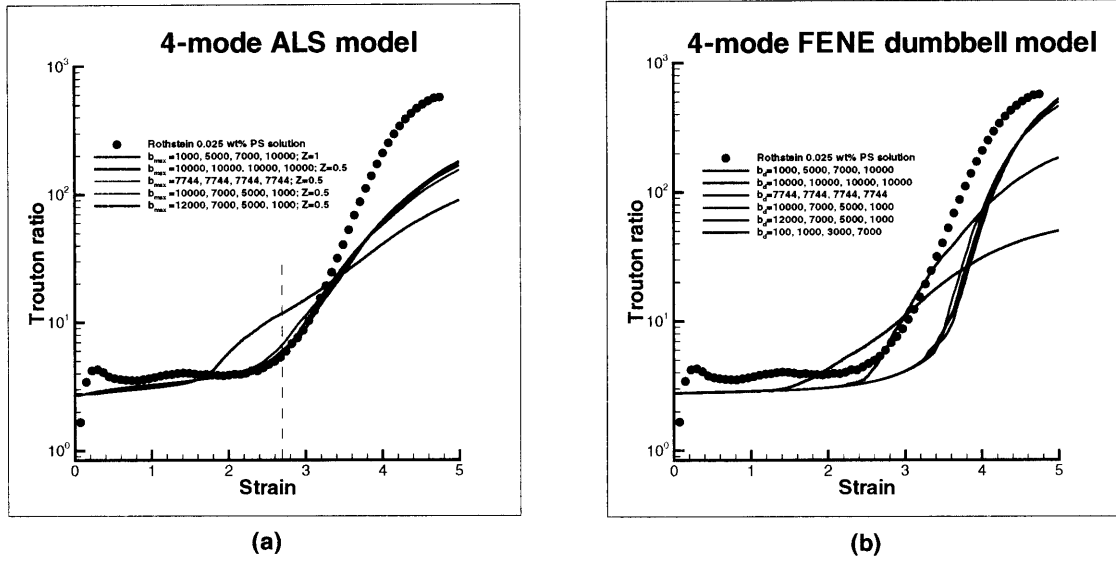


Figure 6-3: Data fitting to extensional rheology with (a) 4-mode ALS model and (b) 4-mode FENE dumbbell model to determine the best values of  $b_{max}$  for each mode. Trouton ratio is defined as  $\bar{\eta}^+/\eta_0$ , where  $\bar{\eta}^+$  is the transient extensional viscosity and  $\eta_0$  is the zero-shear rate viscosity. The vertical dashed line at Strain of 2.75 indicates the maximum value of strain achieved in the experimental setup;  $\dot{\epsilon} = 9.1$  sec.

However, as explained in Chapter 4, the FENE chain is too expensive to simulate, which would make it impossible to use this model in complex flow simulations, where having an efficient Brownian dynamics simulation is of utmost importance. The five-mode FENE dumbbell model does better than the ALS model for strains up to 1.2, which can possibly be explained by the fact that while the ALS model only has a single time constant at a given time, the five-mode FENE dumbbell model possess all five and is thus able to capture the short time-scale dynamics better. For larger strains, the faster modes in the multi-mode FENE model begin to dominate, thus causing a slower rise to steady state as compared to the other models. With the approximate Newton's method used to solve for  $b_{seg}^*$ , the ALS simulation is about a factor of two slower than the corresponding FENE dumbbell simulation, which means that a two-mode FENE dumbbell model can be simulated for the price of a single-mode ALS model. Given this and the fact that data-fitting to obtain  $\eta_{p,i}$  is required for a multi-mode model, it is suggested that the ALS model be used. If the polymer solution possesses significant polydispersity, it is recommended that the multi-mode ALS model be used because as Figure 6-3 suggests, the

fit to transient elongational data with a 4-mode FENE dumbbell model is not very good. It must be kept in mind that this recommendation is made based on data-fitting to Rothstein and McKinley's experimental data. In order to draw definite conclusions, more experimental data sets need to be examined.

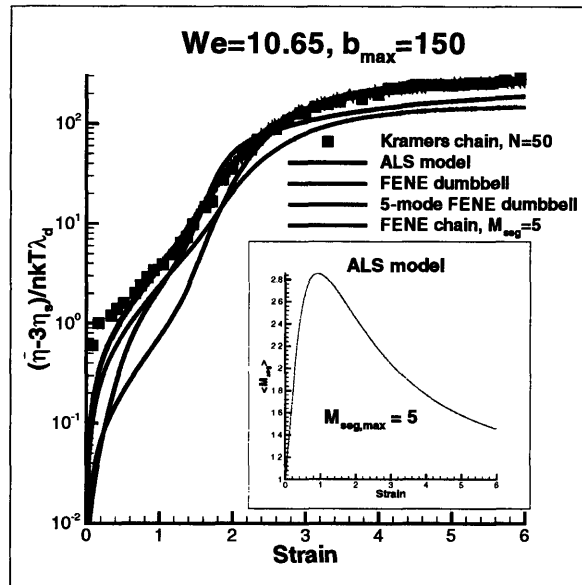


Figure 6-4: Dependence of polymer elongational viscosity on strain for a 50-rod Kramers chain and the corresponding forms of the ALS, FENE dumbbell, 5-mode FENE dumbbell and the 5-spring FENE chain models in start-up of uniaxial extensional flow at  $We = 10.65$ . The maximum extensibility for the single-mode ALS and the single-mode FENE dumbbell models,  $b_{max}$ , is 150. The maximum extensibility for each mode of the 5-mode FENE dumbbell model, starting from the slowest one, are: 150, 75, 50, 37.5, and 30. Maximum extensibility of each spring in the chain is 30. Kramers chain data are obtained from Doyle *et al.* [15]. Insert: Dependence of the ensemble-averaged number of segments in the ALS model on strain.

## Chapter 7

# Complex Flow Calculations Using Stochastic Methods

Although simulating polymer molecules in simple homogeneous flows is important, most flows of industrial importance have a velocity gradient that varies spatially because of complex geometries encountered during processing. In a traditional finite element calculation of a complex flow at steady state, the equations of continuity, motion and the constitutive equation are solved simultaneously. In order to avoid closure approximations, Laso & Öttinger [31] introduced a hybrid method for numerical calculations of viscoelastic flows that is based on coupling standard finite element methods with stochastic simulations of polymer molecule dynamics. They named their algorithm CONNFFESSIT (Calculation of Non-Newtonian Flow: Finite Element and Stochastic Simulation Technique). One of the advantages of CONNFFESSIT is that it allows for models more complicated than Hookean dumbbells to be used without closure approximations. The use of CONNFFESSIT also offers the advantage that, in principle, it is relatively easy to change models; and a wide range of molecular effects, such as polydispersity, hydrodynamic interaction, excluded volume, and polymer migration can be incorporated into the calculations. Depending on the way the convection term in the Fokker-Planck equation is treated, CONNFFESSIT approaches can be classified as Lagrangian or Eulerian, which is also known as the Brownian Configuration Fields (BCF) method. The two approaches as well as the operation count to assess feasibility of using the ALS model in complex flow calculations

are discussed in Sections 7.1, 7.2, and 7.3, respectively. Simulation results of the ALS-C model in complex flows obtained from the literature are presented in Section 7.4.

## 7.1 Lagrangian CONNFFESSIT method

The convective term in the Fokker-Planck equation (second term on the left hand side of Eqn. ??) determines the location of a polymer molecule in space. In the original CONNFFESSIT method, this contribution is converted into an ordinary differential equation that describes the center of mass position. The algorithm begins with an initial guess of the velocity field and a large number of molecules randomly dispersed throughout the flow domain. Stochastic simulations of polymer molecules moving along streamlines are performed next. The molecules are then sorted into cells, and the local value of stress is calculated from the ensemble of molecules present in each cell. After that, information about the stress is fed into the finite element solver and a new velocity field is computed from the balance equations. Stochastic simulations of molecules moving along the new set of streamlines are then performed and the entire process is repeated until the velocity field converges. In their original paper on CONNFFESSIT, Laso & Öttinger used a time-dependent plane Couette flow as a test problem for Hookean, FENE and FENE-P dumbbells. Feigl *et al.* [19] extended this algorithm to apply to a two-dimensional steady-state flow of Hookean dumbbells in an abrupt 4:1 axisymmetric contraction under isothermal conditions. They reported disagreement in stress of up to 20% when using CONNFFESSIT as compared to a closed-form integral constitutive model. This may possibly be attributed to the fact that while time-step convergence was achieved, there was a lack of convergence in mesh and ensemble. The only way to overcome this problem is to refine the mesh and increase the number of streamlines at the same time. Laso *et al.* [33] analyzed time-dependent, two-dimensional flows of FENE dumbbells in a journal-bearing geometry and showed that differences exist in the stress field predicted by FENE and FENE-P models. Cormenzana *et al.* [14] used CONNFFESSIT in calculation of free surface flows to solve the extrudate-swell problem. They reported qualitative agreement between CONNFFESSIT and the continuum calculations.

The inconvenient and often computationally difficult problem that arises in the Lagrangian

CONNFFESSIT method has to do with tracking individual molecules. To calculate a local value of stress, molecules must be sorted into cells at each time step. Because tracking occurs with finite accuracy, one has to check for particles leaving the flow domain through the boundaries. It is also possible for molecules to be concentrated in certain regions, thus leaving fewer trajectories in other regions and decreasing the accuracy of calculated ensemble average quantities. To deal with this problem, Jendrejack *et al.* [27] used a method called OSSM (Operator-Splitting Moment Matching). In this method, instead of tracking individual molecules, one follows the convection of a fixed set of moments and then determines the configuration of each molecule by matching the moments computed from a convection equation with those obtained from a conventional stochastic simulation. An improved algorithm based on various particle-tracking techniques was proposed by Keunings and coworkers ([61]). The main idea of their algorithm was to divide molecules into subensembles and to assume that the centers of mass of all molecules in a given subensemble evolve in the same manner.

The original CONNFFESSIT method requires at least  $N_{node} * N_{traj}$  random numbers to be generated, where  $N_{node}$  is the number of nodes in the spatial discretization and  $N_{traj}$  is the number of stochastic trajectories being simulated. To put this into perspective, a sample simulation with 10,000 trajectories and 16,000 DG nodes, will require generation of  $1.6 \times 10^8$  random numbers per time step, which ends up being by far the most expensive step in the whole simulation. The two methods, CONNFFESSIT and the Brownian configuration fields method, which is discussed in the next section, are explained pictorially in Figure 7-1. Whereas ensembles are uncorrelated in the Lagrangian implementation of CONNFFESSIT, the same ensemble of random numbers is generated at each node in the physical domain in the Brownian configuration fields approach, thus causing tremendous computational time savings and reducing the error of the simulation.

Another limitation of the CONNFFESSIT method as well as any other trajectory-based Brownian dynamics simulation has to do with fluctuations of the stochastic trajectories with time even after macroscopic steady state has been reached. The macroscopic stress that is used to calculate the velocity and pressure fields is hence erratic as well, which often causes problems with convergence. To reduce the magnitude of fluctuations in quantities obtained using CONNFFESSIT, Öttinger *et al.* [46] proposed using the same initial ensemble of dumbbells in each

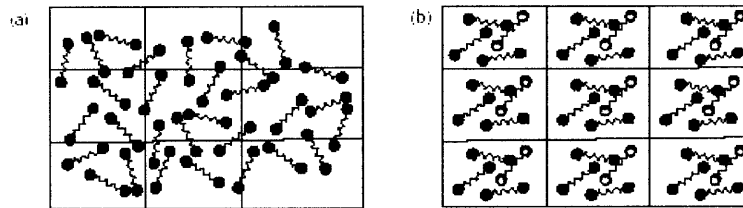


Figure 7-1: Comparison between Lagrangian (CONNFFESSIT) and Eulerian (Brownian configuration fields) implementations. (a) Lagrangian implementation, in which ensembles at adjacent nodes are uncorrelated; (b) Eulerian implementation, where the same ensemble of random numbers is generated at each node in the physical domain.

element instead of using independent ensembles. This scheme would create strong correlations in the stress fluctuations of neighboring elements. When forming the natural differences implied by the divergence of the stress tensor in the equation of motion, significant variance reduction should result from the cancellations of these fluctuations. While significant reduction in computer time is obtained by not using independent ensembles, one has to keep in mind that the attempt to mimic real polymer molecules has been partly undermined by the introduction of these unphysical correlations in random forces. This variance-reduced CONNFFESSIT method should not be used for problems involving small length scales where spatial fluctuations may become relevant. Another issue with using a Brownian dynamics based approach is that these simulations lose accuracy as  $De$  gets small, which can be problematic considering that most complex flow simulations are either performed at low  $De$  or the geometries of interest contain regions of low  $De$ .

## 7.2 Eulerian CONNFFESSIT method (Brownian Configuration Fields)

To avoid completely the problem of having to track individual particles, Hulsen *et al.* [26] and van den Brule *et al.* [58] proposed a CONNFFESSIT method with a Eulerian frame of reference called Brownian configuration fields. This is essentially the generalization to two and three dimensions of the variance-reduced CONNFFESSIT approach discussed in the previous section. The basic idea of the Brownian configuration fields method is to replace a collection of

discrete particles each specified by its configuration vector  $\mathbf{Q}_i$  by an ensemble of  $N_f$  continuous configuration fields  $\mathbf{Q}_i(\mathbf{x}, t)$ . Because of this field concept, the spatial variation of the molecular field can be discretized. Instead of having an independent equation for the motion of a molecule's center of mass, the authors included the convection term in the stochastic differential equation by rewriting it as a partial, stochastic differential equation of the following form

$$d\mathbf{Q}(\mathbf{x}, t) = \left( -\mathbf{v}(\mathbf{x}, t) \cdot \nabla \mathbf{Q}(\mathbf{x}, t) + \boldsymbol{\kappa}(t) \cdot \mathbf{Q}(\mathbf{x}, t) - \frac{2}{\zeta} \mathbf{F}^{(c)}(\mathbf{x}, t) \right) dt + \sqrt{\frac{4kT}{\zeta}} d\mathbf{W}(t) \quad (7.1)$$

SU, SUPG, and DG can all be used to discretize Equation 7.1. The DG formulation is desirable for solving large problems because the total operation count for solving the problem with this method is orders of magnitude smaller than if either SU or SUPG were used (see [55] for explanations of each formulation).

To test the algorithm, van den Brule *et al.* [58] simulated the start-up of flow of Hookean dumbbells past a cylinder confined between two parallel plates and demonstrated that their results were in good agreement with those obtained by using a macroscopic Oldroyd-B model. An additional advantage of the Brownian configuration fields is that the same random numbers can be used at each node in the physical domain, thus requiring a total of only  $N_{traj}$  random numbers to be generated, where  $N_{traj}$  is now the number of convected configuration fields. This results in a high spatial correlation, which serves to reduce the variance of stochastic simulations. The Brownian configuration fields method was used in combination with the adaptive viscosity split stress (AVSS) finite element formulation by Fan *et al.* [18] to simulate dynamics of fiber suspensions. Somasi & Khomami [51], on the other hand, applied Brownian configuration fields to investigate stability of viscoelastic flows in complex geometries. The problem with their approach is that there does not exist a steady state for a Brownian trajectory, and therefore there is no definite base state. Because of this, simulations of the base state and the perturbed state must be performed simultaneously. The authors demonstrated good agreement between their results and those obtained from continuum simulations for a number of simple geometries. Whereas most work has been done with coupling finite elements with Brownian dynamics simulations, Bell *et al.* [3] coupled Brownian dynamics with a spectral method. Because spectral methods have very high convergence rates, their computational requirement is much smaller

than that of CONNFFESSIT. The downside, however, is the limited number of problems that can be solved successfully with the spectral method. Chauvière and Lozinski [13] proposed a new approach for calculating polymeric extra-stress for dilute polymeric solutions, which is derived from the Brownian configuration fields method. Their method has the advantage of both the closed-form constitutive equations (efficiency and noise-free solutions) and stochastic simulations (robustness). Results were presented by solving the benchmark problem of the flow of an Oldroyd-B fluid past a cylinder in a channel using a spectral method.

### 7.3 Feasibility of using ALS in complex flow simulations

Chapter 4 discussed the approaches that were taken to make the ALS model simulation time as close as possible to that of the FENE dumbbell model in order for the former to be feasible for use in complex flow calculations. In this section, the feasibility of using the ALS model with the Brownian configuration fields approach is assessed in the context of a benchmark contraction-expansion problem. It is assumed that the operator splitting is used to decouple computation of the process environment from the polymer microstructure. In this approach, macroscopic and microscopic conservation relations are used to model various process effects such as different processing geometries, free-surface geometries, non-isothermal effects, and crystallization kinetics. Through these relations, the process environment is computed, consisting of velocity, velocity gradient, temperature, free surface shape, crystalline fraction, etc. These fields are fed as data into the model for the polymer microstructure where stress is calculated. The stress is then fed as data into the process environment solver (also known as the  $\mathbf{v} - p - \mathbf{G}$  solver, where  $\mathbf{G}$  is defined as  $\nabla \mathbf{v}$ ) to calculate again the velocity and pressure fields. This process continues for a desired period of time or until steady state is reached. The key idea of the operator splitting method is that changes to one of the solvers have no effect on the other solver. The operator splitting method is shown in Figure 7-2.

The data used for an operation count for the ALS model is presented in Table 7.1. It was chosen to use a sample grid containing 4,000 elements, which results in 4,221 linear nodes, 16,441 quadratic nodes and 16,000 DG nodes. 2,000 Brownian configuration fields were used to calculate polymer contribution to the stress tensor, which is similar to what was used in

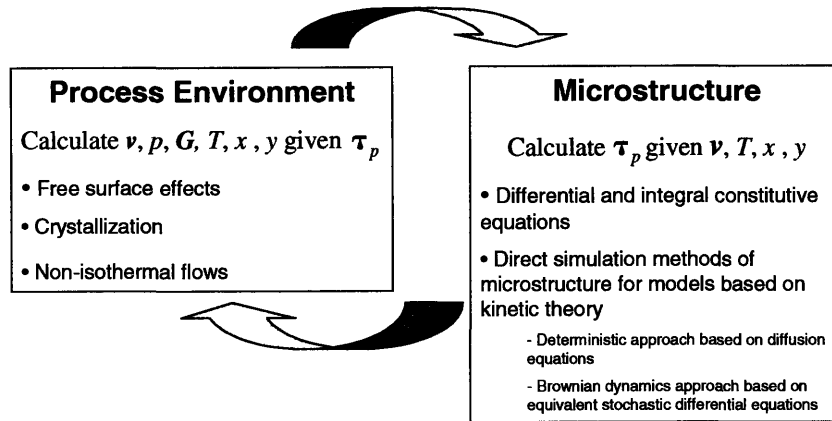


Figure 7-2: In the operator splitting method, the macroscopic process environment solver and the microstructure solvers are completely decoupled, which means that changes to one of the solvers have no effect on the other one.

the literature. In order to do the estimate, it is necessary to know how long to perform the simulation for, i.e. when steady state will be reached. We used a dimensionless time of 20 units because that is roughly how long it took to achieve steady state in the same problem, but with the closed-form of the model, ALS-C.

Number of elements	4,000
Number of linear nodes	4,221
Number of quadratic nodes	16,441
Time to steady state (dimensionless)	20
Number of DG nodes	16,000
Number of configuration fields	2,000

Table 7.1: Operation count for the ALS model in complex flow calculations

To get an idea of how much CPU time would be spent in the  $\mathbf{v} - p - \mathbf{G}$  solver and the microstructure solver, a degree-of-freedom analysis can be performed. The total number of degrees of freedom in the  $\mathbf{v} - p - \mathbf{G}$  problem that needs to be solved for is given by the following expression

$$DOF_{\mathbf{v}-p-\mathbf{G}} = DOF_{lin} \times N_{lin} + DOF_{quad} \times N_{quad} = \tag{7.2}$$

$$4 \times 4,221 + 2 \times 16,441 =$$

where  $DOF_{lin}$  is the number variables that are solved for on linear nodes ( $p, G_{11}, G_{12}, G_{21}$ ),  $DOF_{quad}$  is the number variables that are solved for on quadratic nodes ( $v_x, v_y$ ), and  $N_{lin}$  and  $N_{quad}$  are the number of linear and quadratic nodes in the mesh, respectively. The total number of degrees of freedom for the stress solver are given in Equation 7.3. Equations 7.2 and 7.3 make it clear that the amount of time spent on computing the velocity and pressure fields is negligible compared to the time it takes to simulate polymer molecules with Brownian dynamics in order to calculate stress. Equation 7.3 should also make it clear why so much effort was devoted to finding ways to speed up the ALS simulation.

$$DOF_{microstructure} = N_{DG} \times N_{field} \times DOF_{DG} = \quad (7.3)$$

$$16,000 \times 2,000 \times 4 =$$

$$1.28 \times 10^8$$

The CPU requirement for the microstructure solver will then be about 162 hours and will require about 1Gb of memory. Because stochastic trajectories are independent, an almost linear speed-up would be achieved on parallel processors. Performing this calculation on 16 processors would only take a little over an hour. To minimize communication between parallel processors, it may be beneficial to parallelize by fields and not by computational nodes, which means that the physical domain is divided into subregions and trajectories from each region are 'sent' to the same processor. Such parallelization technique is recommended because ensemble averaging will almost always be performed with regard to an element, and this approach will, therefore, provide the convenience of keeping together all members of the local ensembles. It also seems to make physically more sense to assign one or more elements and the particles residing in them to a given node because all molecules in a given element share the same macroscopic information (e.g. velocity and velocity gradient). The schematic description of this parallelization technique

is depicted in Figure 7-3.

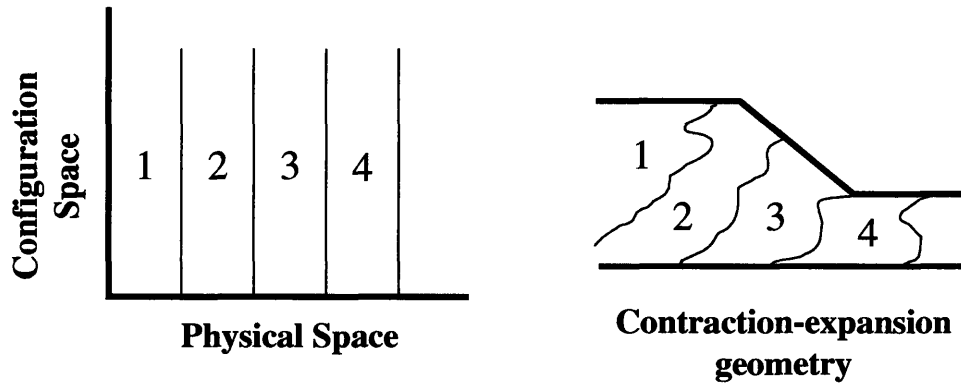


Figure 7-3: Schematic of the parallelization process for the contraction-expansion problem.

## 7.4 ALS-C in complex flows

The creeping flow of a dilute (0.025 wt%) monodisperse polystyrene/polystyrene Boger fluid through a 4:1:4 axisymmetric contraction-expansion geometry with a sharp re-entrant corner was studied experimentally for a wide range of  $De$  by Rothstein and McKinley [48]. By measuring the pressure drop across the orifice plate, they showed that there exists a large extra pressure drop, which increases monotonically with increasing  $De$ , above the value observed for a Newtonian fluid subjected to the same flow conditions.

A schematic diagram of the contraction-expansion geometry along with most important length scales is shown in Figure 7-4. The radii of the cylindrical tubes upstream and downstream of the contraction are equal and given by  $R_1$ . The radius of the contraction region is  $R_2$  and its length is  $L_c$ . The re-entrant corner is slightly rounded, and its radius is given by  $R_c$ . Also shown in the figure are sample polymer molecule conformations in the three key regions. Far upstream from the contraction, most molecules are in their coiled equilibrium configurations. As molecules get near the contraction region, they get subjected to strong elongational flow and become stretched out. Subsequent to leaving the contraction region, molecules undergo biaxial expansion and eventually coil up again as they move far away downstream.

The enhancement in the pressure drop is not associated with the onset of instability, yet

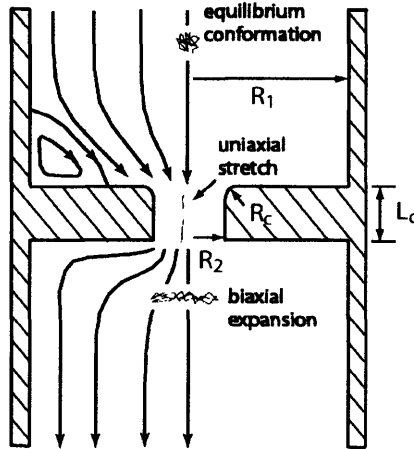


Figure 7-4: Schematic diagram of the contraction–expansion geometry with definition of important length scales.  $R_1$  is the radius of the tubes upstream and downstream of the contraction,  $R_2$  is the radius of the contraction region,  $L_c$  is the length of the contraction, and  $R_c$  is the re-entrant corner radius of curvature.

as Figure 7-5 shows, it cannot be predicted with a simple dumbbell model. In Figure [?], experimental observations by Rothstein and McKinley are presented along with simulation results of the FENE-CR model by Szabo *et al.* [56]. Contrary to experimental predictions, simulation results of Szabo *et al.* predict an initial decrease in the dimensionless pressure drop with increasing Deborah number. Figure 7-6 presents experimental observations of a Boger fluid in the 4:1:4 contraction-expansion geometry with a rounded re-entrant corner by Rothstein and McKinley [49] and simulation results of the FENE-P dumbbell and the ALS-C models by Phillips [47]. It is clear that even though the ALS-C model does not capture quantitatively the increase in the dimensionless pressure drop correctly, it does predict the trend correctly, which in itself is a significant improvement over simple dumbbell model predictions.

Another interesting benchmark problem involves the flow around an array of cylinders confined symmetrically between two parallel plates. In the geometry schematic shown in Figure 7-7,  $L$  is the inter-cylinder spacing,  $R_c$  is the cylinder radius, and  $H_c$  is the half-height of the channel. The Weissenberg number for this kind of flow is defined as

$$We = \lambda \frac{\langle v \rangle H_c}{(H_c - R_c)^2} \quad (7.4)$$

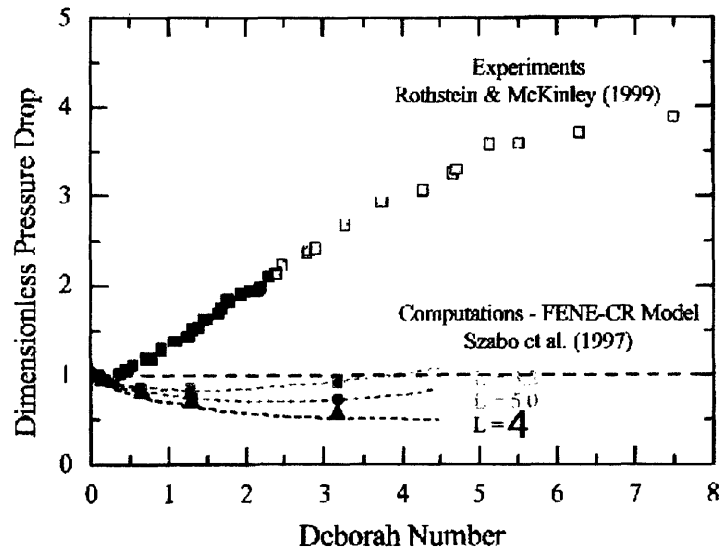


Figure 7-5: Extra pressure drop made dimensionless by the pressure drop for the Newtonian fluid as a function of  $De$  for the 4:1:4 axisymmetric contraction-expansion problem with a sharp re-entrant corner. Data presented are from experiments ([48]) and from computations with the FENE-CR model with the maximum extensibility  $L = 3.2, 4, 5$  ([56]). The horizontal dashed line corresponds to the Newtonian limit.

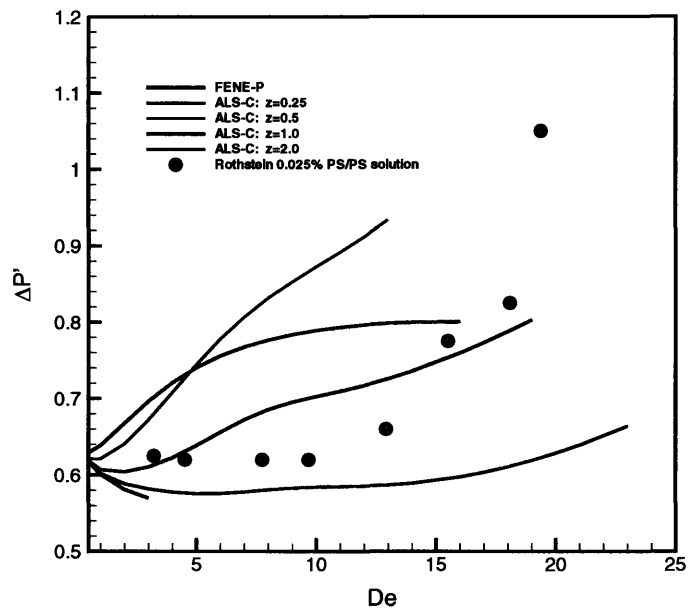


Figure 7-6: Extra pressure drop made dimensionless by the pressure drop for the Newtonian fluid as a function of  $De$  for the 4:1:4 axisymmetric contraction-expansion problem with a rounded re-entrant corner. The plot includes: experimental data for the Boger fluid by Rothstein and McKinley ([49]), FENE-P dumbbell results and single-mode ALS-C results with  $Z = 0.25, 0.5, 1,$  and  $2$  and  $b_{\max} = 7,744$  from simulations by Phillips ([47]).

where  $\langle v \rangle$  is the average velocity and  $\lambda$  is the characteristic polymer relaxation time. At small values of  $L$  the flow is shear-dominated, and the extensional component of the flow becomes stronger as  $L$  increases. In Figure 7-8, the critical value of the Weissenberg number,  $We_{cr}$ , is plotted as a function of the inter-cylinder distance  $L$  for the experimental data with the PIB/PB Boger fluid by Liu ([38]), Oldroyd-B simulations results by Smith *et al.* ([50]) and ALS-C results by Joo *et al.* ([28]). Critical value of the Weissenberg number is defined as the value of  $We$  beyond which the flow becomes unstable. The experimental data predict that as  $L$  increases,  $We_{cr}$  will decrease. The Oldroyd-B model result for  $L = 2.5$  is in a good agreement with experiments, but the model fails to predict the observed flow destabilization with increasing inter-cylinder spacing. The ALS-C model is the only model that is able to capture correctly this destabilization, although more work is required to match experimental results quantitatively as well as qualitatively. Given the promising results obtained with the ALS-C model in the benchmark problems of flow through the contraction-expansion geometry and flow around an array of cylinders, it is of great interest to see how the unapproximated version of the ALS-C model, the ALS model, will behave in the same flow situations.

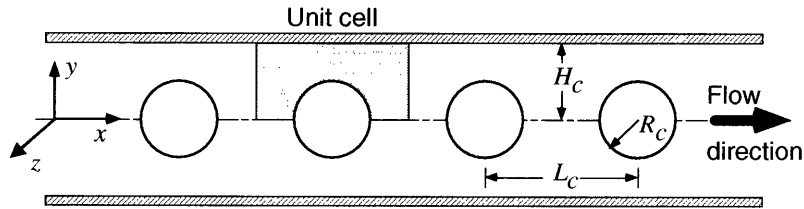


Figure 7-7: Flow past a linear, periodic array of cylinders confined between two parallel plates. The cylinders each have radius  $R_c$ , and the geometry is specified by the cylinder-to-cylinder spacing  $L$  and the channel half height  $H_c$ . The unit cell on which computations are performed is shaded.

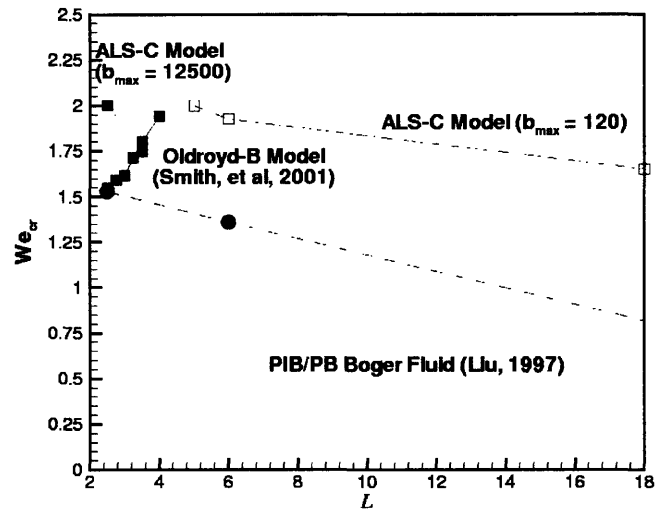


Figure 7-8: Dependence of the critical Weissenberg number,  $We_{cr}$  on the inter-cylinder spacing  $L$  for the flow around an array of cylinders confined between two parallel plates. Data presented are: PIB/PB Boger fluid experimental data by Liu ([38]), simulation results with an Oldroyd-B model by Smith *et al.* ([50]), and simulations results with the ALS-C model by Joo *et al.* for  $b_{max} = 120$  and 12,500 ([28]).

# Chapter 8

## Conclusion

### 8.1 Summary

The use of molecular models to calculate polymer conformations and hence the polymer contribution to the stress tensor, has been an active area of research in the last decade. In this thesis, we explore the use of the Adaptive Length Scale (ALS) model in simple flow calculations and compare results with those obtained using other competing rheological models. Using the formulation of Ghosh et al. [25], we first attempt to optimize the model in order to decrease its simulation time by as much as possible, ideally having it close to the time it takes to simulate a suspension of FENE dumbbells. Most of the effort is spent on looking for efficient ways to solve a 6th-order nonlinear algebraic equation for  $b_{\text{seg}}^*$ .

First, the use of the bisection method is explored. This method, although guaranteed to find a root if one lies in the bracketed region in which the search takes place, has a linear convergence rate and hence takes too long. Next, we implemented the Newton's method and achieved significant solution speed-up due to the method's quadratic convergence. How successful Newton's method is depends on the quality of the initial guess. Ideally, the solution  $b_{\text{seg}}^*$  for stochastic trajectory  $i$  would be used as the initial guess in solving for  $b_{\text{seg}}^*$  for trajectory  $i + 1$ , which makes sense because all molecules in the ensemble are subjected to the same flow conditions. Unfortunately, we are not able to implement this because of the shape of the function, and are forced to use the same initial guess throughout the simulation. The use of a lookup table is also considered, but the table has to be made extremely fine because molecules

undergoing the startup of uniaxial elongational flows experience a wide range of end-to-end extensions, which must be captured accurately. Generating fine tables is time-consuming, and since this method does not offer significant CPU savings as compared to the Newton's method, its use in simulations was rejected. Given the fact that there exist efficient ways of finding roots of polynomial expressions, we attempted to put the algebraic equation in such a form. The only way to do so, however, is to form an 8th degree polynomial with a spurious real positive root with no apparent way to differentiate it from the true root. Hence, this method is rejected as well. The most promising solution method in terms of simulation time is obtained with Newton's method, but with a part of the expression replaced by a third degree polynomial. We call this the approximate Newton's method. With this method implemented, simulation time of the ALS model is only a factor of two longer than the simulation time of a FENE dumbbell model.

In an attempt to optimize the ALS model further, an attempt is made to replace the explicit time integrator in the stochastic differential equation for  $\mathbf{Q}$  and the ordinary differential equation for  $b_{\text{seg}}$  by a semi-implicit predictor-corrector method proposed to Öttinger [45]. The predictor-corrector method requires a solution of a cubic equation at each time step for each trajectory. This method is about 3.5 times slower for a FENE dumbbell and about 1.5 times slower for the ALS model as compared to the case when an explicit time-stepping method is used. If the FENE dumbbell model is used, the time-step can be increased by an order of magnitude, and therefore there is definitely the advantage of using the semi-implicit method. In the case of the ALS model, even though the stochastic equation would support a larger time step size increase,  $\Delta t$  can only be increased by roughly a factor of two as compared to the explicit Euler method. A further increase in  $\Delta t$  renders the evolution equation for  $b_{\text{seg}}$  unstable, which causes the simulation to fail. Therefore, unless the  $b_{\text{seg}}$  equation is made more stable, there is no enormous benefit to using the predictor-corrector method in the ALS model.

We subsequently use the optimized version of the ALS model in simple flow calculations to assess and compare its rheological predictions with other rheological models such as the Kramers chain, the FENE chain and the FENE dumbbell. Our results agreed well with those of Ghosh *et al.* [25]. The ALS model predicts the rapid extension stress growth in the startup of uniaxial elongational flow, which is in very good agreement with the Kramers chain results. The stress

growth predicted by the FENE dumbbell model, on the other hand, is slower at intermediate values of strain. If one is interested in finding a micromechanical molecular model, which will mimic the behavior of real polymer solutions in homogeneous flows, then it makes sense to use a detailed model such as the Kramers chain or a five-spring FENE chain. However, our goal is to find a model, which will predict simple flow rheological properties accurately AND is feasible for use in complex flow simulations. The Kramers chain and the FENE chain are too detailed for this purpose, and hence are only considered as benchmark results. The shear stress growth predicted by the ALS model in the startup of steady shear flow is also in much better agreement with the Kramers chain results as compared to those predicted by the FENE dumbbell model. Steady state elongational viscosities predicted by the ALS model and the FENE dumbbell are essentially identical, which is expected because at high strains, a majority of molecules undergoing uniaxial elongational flow will be fully stretched, and the adaptive length scale in the ALS model will equal the maximum extensibility  $b_{\max}$  of the FENE dumbbell.

We also explored the use of multi-mode models in simple flow calculations in an attempt to capture the spectrum of relaxation times possessed by real polymer solutions. The modes are assumed to be independent, which means that total simulation time scales linearly with the number of modes. As expected, the fit to the linear viscoelastic data with a four-mode model is much better than the fit with a single-mode model. However, we were not able to achieve a good enough fit to the transient extensional data by Rothstein and McKinley [49] to justify quadrupling the CPU time to simulate a four-mode model.

Lastly, we assessed the feasibility of incorporating the ALS model into the complex flow solver using the Brownian configuration fields approach in the context of a benchmark contraction-expansion problem. It was assumed that the operator splitting will be used to decouple computation of the process environment from the polymer microstructure. The number of elements in the finite element mesh as well as the length of time to achieve steady state was chosen to match those used by Phillips [47] in the analogous calculation, but with the closed-form version of the model, ALS-C. In the Brownian configuration fields approach, the solution of the stochastic differential equation takes up the majority of CPU time. Since the solution of the  $\mathbf{v} - p - \mathbf{G}$  problem does not depend on which rheological model is used, whether or not the configuration fields approach using the ALS model is feasible will depend on how long it takes

to solve the microstructure equation. From the operation count, we found that solution on a single processor will take about 162 hours and will require 1Gb of memory. Given the fact that stochastic trajectories are independent from one another, the microstructure solver should lend itself to efficient parallelization, which means that the ALS model can be used in complex flow calculations.

## 8.2 Suggested future work

Although this thesis concentrates on simple flow situations, one of its main goals has been to show that the ALS model is robust and can be used in complex flow simulations. The operation count in the previous chapter shows that the model is indeed feasible for use in complex geometries. However, before the ALS model is used, a couple of features of the model must be looked at. First of all, it is extremely important to understand why the ALS model takes so long to achieve steady state in the startup of steady uniaxial elongational flows. The evolution equation for the dimensionless extensibility  $b_{\text{seg}}$  was not based on a rigorous derivation in a kinetic theory framework, but was rather motivated by observations of the Kramers chains behavior in extensional flows. Hence, it is possible that the relaxation term in this equation is too weak compared to the stiffness term. Understanding what drives the rate at which the ALS model approaches steady state may help explain why the stress-birefringence hysteresis predicted by this model is much smaller than that of the Kramers chain and the FENE dumbbell. Developing a more stable evolution equation for  $b_{\text{seg}}$  may have the added benefit of allowing a larger time-step size with the semi-implicit time integration algorithm, which will further decrease simulation time of the ALS model. Another approach to consider is to have different time-step sizes in the stochastic differential equation and the evolution equation for  $b_{\text{seg}}$  so that, for example, for each time-step advancement of the stochastic equation, the equation for  $b_{\text{seg}}$  will be time-integrated twice.

# Bibliography

- [1] K. Adachi. Calculation of strain histories in Protean coordinate system, *Rheol. Acta*, **22**: 326-335, 1983.
- [2] R.C. Armstrong, R. Nayak, and R.A. Brown. The use of kinetic theory and microstructural models in the analysis of complex flows of viscoelastic liquids, *Proceedings of the XIIth International Congress on Rheology*, Quebec: Laval Univ., 307-310, 1996.
- [3] T.W. Bell, G.H. Nyland, J.J. de Pablo, and M.D. Graham. Combined Brownian dynamics and spectral simulation of the recovery of polymeric fluids after shear flow, *Macromolecules*, **30**: 1806-1812, 1997.
- [4] R.B. Bird, R.C. Armstrong, and O. Hassager. *Dynamics of Polymeric Liquids, Vol. 1: Fluid Mechanics*. New York: Wiley, 1987.
- [5] R.B. Bird, C.F. Curtiss, R.C. Armstrong, and O. Hassager. *Dynamics of Polymeric Liquids, Vol. 2: Kinetic Theory*. New York: Wiley, 1987.
- [6] R.B. Bird, P.J. Dotson, and N.L. Johnson. Polymer solution rheology based on a finitely extensible bead-spring chain model, *J. Non-Newtonian Fluid Mech.*, **7**: 213-235, 1980.
- [7] R.B. Bird and H.C. Öttinger. Transport properties of polymeric liquids, *Annu. Rev. Phys. Chem.*, **43**: 371-406, 1992.
- [8] R.B. Bird and J.M. Wiest. Constitutive equations for polymeric liquids, *Annu. Rev. Fluid Mech.*, **27**: 169-193, 1995.
- [9] D.V. Boger and K. Walters, *Rheological Phenomena in Focus*, Amsterdam: Elsevier, 1993.

- [10] J. Bonvin and M. Picasso. Variance reduction methods for CONNFFESSIT-like simulations, *J. Non-Newtonian Fluid Mech.*, **84**: 191-215, 1999.
- [11] W.R. Burghardt, J.M. Li, and B. Khomami. Uniaxial Extensional Characterization of a Shear Thinning Fluid Using Asisymmetric Flow Birefringence, *J.Rheol.*, **43**: 147-165, 1999.
- [12] J.J. Cascales, F.G. Diaz, and J.G. de la Torre. Simulation of non-linear models for polymer chains in flowing solutions, *Polymer*, **36**: 345-351, 1995.
- [13] C. Chauvière and A. Lozinski. An efficient technique for simulations of viscoelastic flows, derived from the Brownian configuration field method, *Siam Journal on Scientific Computing*, **24**: 1823-1837, 2003.
- [14] J. Cormenzana, A. Ledda, and M. Laso. Calculation of free surface flows using CONNFFESSIT, *J. Rheol.*, **45**:237-257, 2001.
- [15] P.S. Doyle and E.S.G. Shaqfeh. Dynamic simulation of freely-draining, flexible bead-rod chains: Start-up of extensional and shear flow, *J. Non-Newtonian Fluid Mech.*, **76**: 43-78, 1998.
- [16] P.S. Doyle, E.S.G. Shaqfeh, and A.P. Gast. Dynamic simulation of freely draining flexible polymers in steady linear flows, *J. Fluid Mech.*, **334**: 251-291, 1997.
- [17] P.S. Doyle, E.S.G. Shaqfeh, G.H. McKinley, and S.H. Spiegelberg. Relaxation of dilute polymer solutions following extensional flow, *J. Non-Newtonian Fluid Mech.*, **76**: 79-110, 1998.
- [18] X.J. Fan, N. Phan-Thien, and R. Zheng. Simulation of fibre suspension flow with shear-induced migration, *J. Non-Newtonian Fluid Mech.*, **90**: 47-63, 2000.
- [19] K. Feigl, M. Laso, H.C. Öttinger. CONNFFESSIT approach for solving a two-dimensional viscoelastic fluid problem, *Macromolecules*, **28**: 3261-3274, 1995.
- [20] S.W. Fetsko, and P.T. Cummings. Brownian dynamics simulations of bead-spring chain models for dilute solutions in elongational flow, *J. Rheol.*, **39**: 285-299, 1995.
- [21] P.J. Flory. *Principles of polymer chemistry*, Ithaca, Cornell, 1953.

- [22] L. Geneiser. *Stress and Velocity Field Evolution in Viscoelastic Planar Contraction Flow*, Ph.D. Thesis, Massachusetts Institute of Technology, 1998.
- [23] I. Ghosh. *Molecular modeling of polymer solutions using Brownian dynamics*, Ph.D. thesis, Massachusetts Institute of Technology, 2000.
- [24] I. Ghosh, G.H. McKinley, R.A. Brown, and R.C. Armstrong. Deficiencies of FENE dumbbell models in describing the rapid stretching of dilute polymer solutions, *J. Rheol.*, **45**: 721-758, 2001.
- [25] I. Ghosh, G.H. McKinley, R.A. Brown, and R.C. Armstrong. A new model for dilute polymer solutions in flows with strong extensional components, *J. Rheol.*, **46**: 1057-1090, 2002.
- [26] M.A. Hulsen, A.P.G. van Heel, and B.H.A.A. van den Brule. Simulation of viscoelastic flows using Brownian configuration fields, *J. Non-Newtonian Fluid Mech.*, **70**: 79-101, 1997.
- [27] R.M. Jendrejack, M.D. Graham, and J.J. de Pablo. Hydrodynamic interactions in long chain polymers: Application of the Chebyshev polynomial approximation in stochastic simulations, *J. Chem. Phys.*, **113**:2894-2900, 2000.
- [28] Y.L. Joo, S.D. Phillips, J.P. Rothstein, G.H. McKinley, R.C. Armstrong, and R.A. Brown. Use of an Adaptive Length Scale Model in the Simulations of Complex Viscoelastic Flows, *XII Numerical workshop*, Monterey Bay, CA, 2001.
- [29] R. Keunings. On the Peterlin approximation of finitely extensible dumbbells, *J. Non-Newtonian Fluid Mech.*, **68**: 85-100, 1997.
- [30] P.E. Kloeden and E. Platen. *Numerical solution of stochastic differential equations*, Berlin: Springer, 1992.
- [31] M. Laso, and H.C. Öttinger. Calculation of viscoelastic flow using molecular models: the CONNFESSIT approach, *J. Non-Newtonian Fluid Mech.*, **47**: 1-20, 1993.
- [32] M. Laso, H.C. Öttinger, and U.W. Suter. Bond length and bond angle distributions in coarse-grained polymer chains, *J. Chem. Phys.*, **95**: 2178-82, 1991.

- [33] M. Laso, M. Picasso, and H.C. Öttinger. 2-D time-dependent viscoelastic flow calculations using CONNFESSIT, *AICHE*, **43**: 877-892, 1997.
- [34] A.T. Lee and A.J. McHugh. Brownian dynamics study of mixed linear-hyperbranched polymers, *Macromolecules*, **34**: 7127-7134, 2001.
- [35] A.T. Lee and A.J. McHugh. Dynamics of dendrimeric molecules undergoing simple shear flow: A nonequilibrium Brownian dynamics study, *Macromol. Theory Simul.*, **10**: 244-254, 2001.
- [36] G. Lielens, P. Halin, I. Jaumain, R. Keunings, and V. Legat. New closure approximations for the kinetic theory of finitely extensible dumbbells, *J. Non-Newtonian Fluid Mech.*, **76**: 249-279, 1998.
- [37] G. Lielens, R. Keunings, and V. Legat. The FENE-L and the FENE-LS closure approximations to the kinetic theory of finitely extensible dumbbells, *J. Non-Newtonian Fluid Mech.*, **87**: 179-196, 1999.
- [38] A.W. Liu. *Viscoelastic Flow of Polymer Solutions Around Arrays of Cylinders: comparison of Experiment and Theory*, Ph.D. Thesis, Massachusetts Institute of Technology, 1997.
- [39] T.W. Liu. Flexible polymer chain dynamics and rheological properties in steady flows, *J. Chem. Phys.*, **90**: 5826-5842, 1989.
- [40] T.C.B. McLeish and R.G. Larson. Molecular constitutive equations for a class of branched polymers: The pom-pom polymer, *J. Rheol.*, **42**: 81-110, 1998.
- [41] M. Melchior and H.C. Öttinger. Variance reduced simulations of stochastic differential equations, *J. Chem. Phys.*, **103**: 9506-9509, 1995.
- [42] M. Melchior and H.C. Öttinger. Variance reduced simulations of polymer dynamics, *J. Chem. Phys.*, **105**: 3316-3331, 1996.
- [43] R. Nayak. *Molecular simulation of liquid crystal polymer flow: a wavelet-finite element analysis*, Ph.D. thesis, Massachusetts Institute of Technology, 1998.

- [44] H.C. Öttinger. A model of dilute polymer solutions with hydrodynamic interaction and finite extensibility. I. Basic equations and series expansions, *J. Non-Newtonian Fluid Mech.*, **26**: 207-246, 1987.
- [45] H.C. Öttinger. *Stochastic processes in polymeric fluids: Tools and examples for developing simulation algorithms*. Springer, Berlin, 1996.
- [46] H.C. Öttinger, B.H.A.A. van den Brule, and M.A. Hulsen. Brownian configuration fields and variance reduced CONNFFESSIT, *J. Non-Newtonian Fluid Mech.*, **70**: 255-261, 1997.
- [47] S. Phillips. Analysis of complex viscoelastic flows using a finite element method, Ph.D. thesis, Massachusetts Institute of Technology, 2005.
- [48] J.P. Rothstein and G.H. McKinley. Extensional flow of a polystyrene Boger fluid through a 4:1:4 axisymmetric contraction/expansion, *J. Non-Newtonian Fluid Mech.*, **86**: 61-88, 1999.
- [49] J.P. Rothstein and G.H. McKinley. The axisymmetric contraction-expansion: the role of extensional rheology on vortex growth dynamics and the enhanced pressure drop, *J. Non-Newtonian Fluid Mech.*, **98**: 33-63, 2001.
- [50] M.D. Smith, Y.L. Joo, R.C. Armstrong, and R.A. Brown. Linear stability analysis of flow of an Oldroyd-B fluid through a linear array of cylinders, *J. Non-Newtonian Fluid Mech.*, **109**: 13-50, 2003.
- [51] M. Somasi and B. Khomami. Linear stability and dynamics of viscoelastic flows using time-dependent stochastic simulation techniques, *J. Non-Newtonian Fluid Mech.*, **93**: 339-362, 2000.
- [52] W.E. Stewart and J.P. Sørensen. Hydrodynamic interaction effects in rigid dumbbell suspensions. II. Computations for steady shear flow, *Trans. Soc. Rheol.*, **16**: 1-13, 1972.
- [53] S.R. Strand, S. Kim, S.J. Karrila. Computation of rheological properties of suspensions of rigid rods: stress growth after inception of steady shear flow, *J. Non-Newtonian Fluid Mech.*, **24**: 311-330, 1987.

- [54] J.K.C. Suen, Y.L. Joo, and R.C. Armstrong. Molecular orientation effects in viscoelasticity, *Annu. Rev. Fluid Mech.*, **34**: 417-444, 2002.
- [55] J.K.C. Suen, *Multiscale simulation of viscoelastic flows: Applications to Kinetic Theory Models of Polymer Melts and Liquid Crystalline Polymers*, Ph.D. thesis, Massachusetts Institute of Technology, 2002.
- [56] P. Szabo, J.M. Rallison, and E.J. Hinch. Start-up of flow of a FENE fluid through a 4:1:4 contraction in a tube, *J. Non-Newtonian Fluid Mech.*, **72**: 73-86, 1997.
- [57] V. Tirtaatmadya and T. Sridhar. Comparison of constitutive equations for polymer solutions in uniaxial extension, *J. Rheol.*, **39**: 1133-1160, 1995.
- [58] B.H.A.A. Van den Brule. Brownian dynamics simulations of finitely extensible bead-spring chains, *J. Non-Newtonian Fluid Mech.*, **47**: 357-378, 1993.
- [59] B.H.A.A. van den Brule, T. van Heel, and M. Hulsen. Brownian configuration fields: A new method for simulating viscoelastic fluid flow, *Macromol. Symp.*, **121**: 205-217, 1997.
- [60] A.P.G. Van Heel, M.A. Hulsen, and B.H.A.A. van den Brule. On the selection of parameters in the FENE-P model, *J. Non-Newtonian Fluid Mech.*, **75**: 253-271, 1998.
- [61] P. Wapperom, R. Keunings, and V. Legat. The backward-tracking Lagrangian particle method for transient viscoelastic flows, *J. Non-Newtonian Fluid Mech.*, **91**: 273-295, 2000.
- [62] H.R. Warnet. Kinetic theory and rheology of dilute suspensions of finitely extensible dumbbells, *Ind. Eng. Chem. Fundam.*, **11**: 379-387, 1972.
- [63] L.E. Wedgewood, D.N. Ostrov, and R.B. Bird. A finitely extensible bead-spring chain model for dilute polymer solutions, *J. Non-Newtonian Fluid Mech.*, **40**: 119-139, 1991.
- [64] L.E. Wedgewood and H.C. Öttinger. A model of dilute polymer solutions with hydrodynamic interaction and finite extensibility. II Shear flows, *J. Non-Newtonian Fluid Mech.*, **27**: 245-264, 1988.
- [65] J.M. Wiest. Birefringence in strong flows of dilute polymer solutions, *Polymer*, **40**: 1917-1922, 1999.

- [66] J.M Wiest, L.E. Wedgewood, and R.B. Bird. On coil-stretch transitions in dilute polymer-solutions, *J. Chem. Phys.*, **90**: 587-594, 1988.